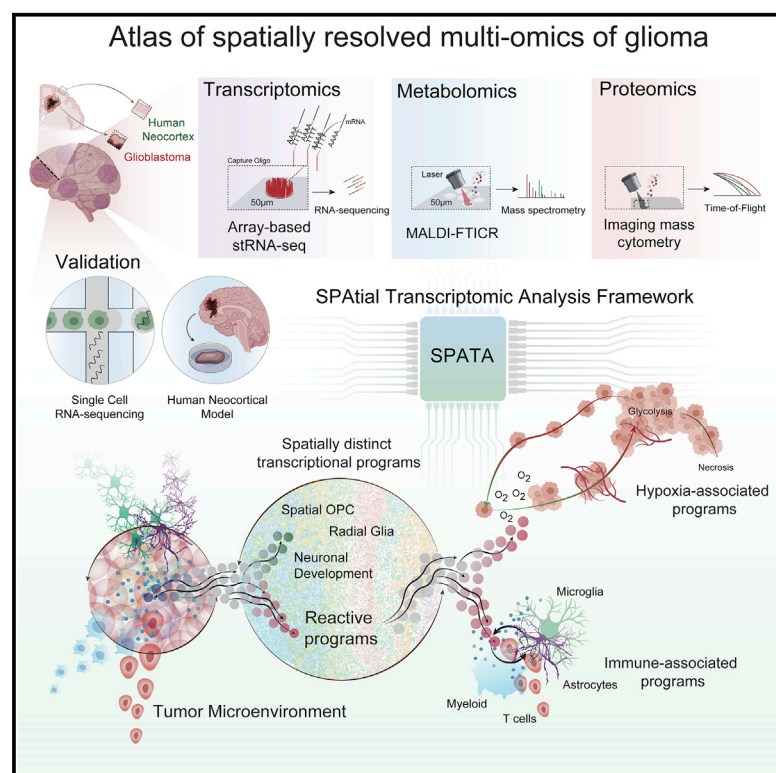


# Spatially resolved multi-omics deciphers bidirectional tumor-host interdependence in glioblastoma

## Graphical abstract



## Authors

Vidhya M. Ravi, Paulina Will, Jan Kueckelhaus, ..., Daniel Delev, Oliver Schnell, Dieter Henrik Heiland

## Correspondence

dieter.henrik.heiland@uniklinik-freiburg.de

## In brief

Ravi et al. employ spatially resolved multi-omics in glioblastoma samples and identify segregated niches hallmarked by immunological and metabolic stress factors. These spatial niches are influenced by the tumor microenvironment and reflect transcriptional adaptations to inflammatory or metabolic stimuli and recapitulate neural developmental stages.

## Highlights

- Five spatially distinct transcriptional programs are identified in glioblastomas
- Hypoxia induces defined transcriptional and genomic responses, including CNAs
- Immunosuppressive tumor-myeloid cell interactions are enhanced in segregated niches
- Non-stress environments support subtype transition towards developmental stages



Article

# Spatially resolved multi-omics deciphers bidirectional tumor-host interdependence in glioblastoma

Vidhya M. Ravi,<sup>1,2,3,4,5,19,26</sup> Paulina Will,<sup>1,2,3,4,26</sup> Jan Kueckelhaus,<sup>1,2,3,4,6,26</sup> Na Sun,<sup>7,27</sup> Kevin Joseph,<sup>1,2,3,4,19,27</sup> Henrike Salié,<sup>3,8,27</sup> Lea Vollmer,<sup>1,2,3,4</sup> Ugne Kuliesiute,<sup>1,4,9</sup> Jasmin von Ehr,<sup>1,2,3,4</sup> Jasim K. Benotmane,<sup>1,2,3,4</sup> Nicolas Neider,<sup>1,2,3,4</sup> Marie Follo,<sup>3,10</sup> Florian Scherer,<sup>3,10</sup> Jonathan M. Goeldner,<sup>1,2,3,4</sup> Simon P. Behringer,<sup>1,2,3,4</sup> Pamela Franco,<sup>3,4</sup> Mohammed Khat,<sup>1,2,3,4</sup> Junyi Zhang,<sup>1,2,3,4</sup> Ulrich G. Hofmann,<sup>2,3,11</sup> Christian Fung,<sup>2,3</sup> Franz L. Ricklefs,<sup>12,13</sup> Katrin Lamszus,<sup>12,13</sup> Melanie Boerries,<sup>3,14,15,16</sup> Manching Ku,<sup>3,17</sup> Jürgen Beck,<sup>2,3,18,19</sup> Roman Sankowski,<sup>3,20</sup> Marius Schwabenland,<sup>3,20</sup> Marco Prinz,<sup>3,18,20,21</sup> Ulrich Schüller,<sup>22,23,24</sup> Saskia Killmer,<sup>3,8</sup> Bertram Bengsch,<sup>3,8,21</sup> Axel K. Walch,<sup>7</sup> Daniel Delev,<sup>6,25,28</sup> Oliver Schnell,<sup>1,2,3,4,19,28</sup> and Dieter Henrik Heiland<sup>1,2,3,15,16,19,28,29,\*</sup>

<sup>1</sup>Microenvironment and Immunology Research Laboratory, Medical Center - University of Freiburg, Freiburg, Germany

<sup>2</sup>Department of Neurosurgery, Medical Center - University of Freiburg, Freiburg, Germany

<sup>3</sup>Faculty of Medicine, University of Freiburg, Freiburg, Germany

<sup>4</sup>Translational NeuroOncology Research Group, Medical Center - University of Freiburg, Freiburg, Germany

<sup>5</sup>Freiburg Institute for Advanced Studies (FRIAS), University of Freiburg, Freiburg, Germany

<sup>6</sup>Neurosurgical Artificial Intelligence Laboratory Aachen (NAILA), Department of Neurosurgery, RWTH University of Aachen, Aachen, Germany

<sup>7</sup>Research Unit Analytical Pathology, Helmholtz Zentrum München, Neuherberg, Germany

<sup>8</sup>Department of Medicine II: Gastroenterology, Hepatology, Endocrinology, and Infectious Disease, Medical Center - University of Freiburg, Freiburg, Germany

<sup>9</sup>The Institute of Biosciences, Life Sciences Center, Vilnius University, Vilnius, Lithuania

<sup>10</sup>Department of Medicine I, Medical Center - University of Freiburg, Freiburg, Germany

<sup>11</sup>Neuroelectronic Systems, Medical Center - University of Freiburg, Freiburg, Germany

<sup>12</sup>Department of Neurosurgery, University Hospital Eppendorf, Hamburg, Germany

<sup>13</sup>Laboratory for Brain Tumor Biology, University Hospital Eppendorf, Hamburg, Germany

<sup>14</sup>Institute of Medical Bioinformatics and Systems Medicine, Medical Center-University of Freiburg, Freiburg, Germany

<sup>15</sup>Comprehensive Cancer Center Freiburg (CCCF), Medical Center - University of Freiburg, Freiburg, Germany

<sup>16</sup>German Cancer Consortium (DKTK), partner site Freiburg, Freiburg, Germany

<sup>17</sup>Department of Pediatrics and Adolescent Medicine, Division of Pediatric Hematology and Oncology, Medical Center - University of Freiburg, Freiburg, Germany

<sup>18</sup>Center for NeuroModulation (NeuroModul), University of Freiburg, Freiburg, Germany

<sup>19</sup>Center of Advanced Surgical Tissue Analysis (CAST), University of Freiburg, Freiburg, Germany

<sup>20</sup>Institute of Neuropathology, Medical Center - University of Freiburg, Freiburg, Germany

<sup>21</sup>Signalling Research Centres BIOSS and CIBSS, University of Freiburg, Freiburg, Germany

<sup>22</sup>Institute of Neuropathology, University Medical Centre Hamburg-Eppendorf, Hamburg, Germany

<sup>23</sup>Research Institute Children's Cancer Center, Hamburg, Germany

<sup>24</sup>Department of Pediatric Hematology and Oncology, University Medical Centre Hamburg-Eppendorf, Hamburg, Germany

<sup>25</sup>Department of Neurosurgery, RWTH University of Aachen, Aachen, Germany

<sup>26</sup>These authors contributed equally

<sup>27</sup>These authors contributed equally

<sup>28</sup>Senior author

<sup>29</sup>Lead contact

\*Correspondence: [dieter.henrik.heiland@uniklinik-freiburg.de](mailto:dieter.henrik.heiland@uniklinik-freiburg.de)

<https://doi.org/10.1016/j.ccell.2022.05.009>

## SUMMARY

Glioblastomas are malignant tumors of the central nervous system hallmarked by subclonal diversity and dynamic adaptation amid developmental hierarchies. The source of dynamic reorganization within the spatial context of these tumors remains elusive. Here, we characterized glioblastomas by spatially resolved transcriptomics, metabolomics, and proteomics. By deciphering regionally shared transcriptional programs across patients, we infer that glioblastoma is organized by spatial segregation of lineage states and adapts to inflammatory and/or metabolic stimuli, reminiscent of the reactive transformation in mature astrocytes. Integration of metabolic imaging and imaging mass cytometry uncovered locoregional tumor-host interdependence, resulting in spatially exclusive adaptive transcriptional programs. Inferring copy-number



alterations emphasizes a spatially cohesive organization of subclones associated with reactive transcriptional programs, confirming that environmental stress gives rise to selection pressure. A model of glioblastoma stem cells implanted into human and rodent neocortical tissue mimicking various environments confirmed that transcriptional states originate from dynamic adaptation to various environments.

## INTRODUCTION

Single-cell technologies have provided insights into the transcriptional regulation and dynamic evolution of individual cells within the healthy human brain and malignancy (Darmanis et al., 2015; Grubman et al., 2019; Neftel et al., 2019; Patel et al., 2014; Tabula Muris Consortium, 2020; Tirosh et al., 2016a; Venteicher et al., 2017). Single-cell RNA sequencing (scRNA-seq) studies of high- and low-grade gliomas have demonstrated that intratumoral heterogeneity and dynamic plasticity across cellular states are hallmarks of malignant brain tumors (Neftel et al., 2019; Tirosh et al., 2016a; Venteicher et al., 2017). This dynamic adaptation occurs within four different states, namely the mesenchymal-like (MES-like), neural progenitor cell-like (NPC-like), astrocyte-like (AC-like), and the oligodendrocytic precursor cell-like (OPC-like) states, mirroring early development of the healthy human brain (Couturier et al., 2020; Neftel et al., 2019). Although brain tumors present similar transcriptional adaptations and evolution to the healthy brain, they have long been studied as an independent entity, overlooking the role of the local microenvironment in tumorigenesis. However, recent reports have sought to detail the local interactions of tumor cells with the neuronal environment, where neurons and glial and immune cells contribute to the intricate and dynamically heterogeneous glioma network (Neftel et al., 2019; Osswald et al., 2015; Venkataramani et al., 2019; Venkatesh et al., 2019; Venteicher et al., 2017; Wurm et al., 2019).

Single-cell analysis provides only indirect inferences of cellular interactions due to the loss of spatial-organization information. In the brain, spatial organization and function are closely related. Thus, we hypothesize that CNS malignancies are also functionally and spatially organized. Spatially resolved transcriptomics is a novel technology that allows us to characterize cellular interactions and organization *in situ* and thus decipher the ecosystem of malignant brain tumors.

Given that scRNA-seq and spatial transcriptomics are not considered competitive but rather complementary (Elosua-Bayes et al., 2021; Kleshchevnikov et al., 2020), the integration of both technologies is pivotal. In addition to the spatially resolved transcriptome, supplementary molecular analyses are required to obtain comprehensive insights into the impact of the microenvironment on tumor cells. Cellular communications and metabolism are two crucial factors that have a decisive impact on the dynamic adaptation of brain cancers, facilitating growth, infiltration, and therapy resistance (Grimes et al., 2020). These metabolic alterations could be attributed to the microenvironment or regional heterogeneity in tumor metabolism. For instance, it has been demonstrated that forced metabolic deterioration due to hypoxia significantly drives transcriptional adaptation (Heiland et al., 2018) and genomic instability (Bhandari et al., 2019). Increased focus has also been placed

on the cellular interactions between tumor cells and the immune system, with a recent study proving that epigenetic immunoediting drives an acquired immune-invasion program contributing to the spatially heterogeneous landscape seen in glioblastoma (Gangoso et al., 2021).

These studies further reinforce the need to comprehensively interrogate the various transcriptional adaptations of glioma due to the microenvironment in a spatially resolved context. Our study aims to provide an atlas of spatially resolved transcriptional programs and cellular interactions of glioblastoma with its local microenvironment.

## RESULTS

### Atlas of spatially resolved transcriptomics in glioblastoma

With the goal of characterizing the spatial architecture of glioblastoma (GBM), we curated an atlas of spatially resolved transcriptomics (stRNA-seq) of twenty-eight specimens (patients  $n = 20$ ) resulting in 88,793 individual transcriptomes across different age groups and anatomic regions. We complemented spatially resolved metabolomics (matrix-assisted laser desorption/ionization [MALDI],  $n = 6$  from patients  $n = 6$ ) and proteomics (imaging mass cytometry,  $n = 14$  regions of interest [ROIs] from patients  $n = 6$ ) from tissue sections subsequent to those used for stRNA-seq to comprehensively integrate multiple molecular layers (Figure 1A). A detailed report on the individual donors and specimens including clinical characteristics and samplewise analysis is provided in Table S1 and Figure S1. Mutual nearest neighbor (MNN)-based horizontal integration and shared nearest neighbor (SNN) clustering revealed that non-malignant specimens (access cortex) demonstrated similarities across patients. Malignant transcriptomes were marked by unique gene-expression profiles, which was further confirmed by the high Shannon entropy of the sample diversity across clusters (Figures 1B and S2A). Samples of malignant origin showed significant lower entropy (adjusted  $p$  value [ $p_{adj}$ ] =  $3.23 \times 10^{-24}$ ), indicating that the clusters were composed of spots from individual patients (Figures 1B and 1C). These findings are in line with recent single-cell studies reporting that high numbers of individual copy-number alterations and mutational profiles contribute to interpatient heterogeneity, resulting in individual transcriptional profiles (Neftel et al., 2019; Richards et al., 2021).

To explore transcriptional diversity in a spatial context, addressing and overcoming several methodological hurdles was necessary. Since the array-based stRNA-seq technology (Visium 10X) is unable to resolve single cells, it requires inference of the cellular composition of each spot. Our approach to approximately deconvolute the cellular composition encompassed two steps: (1) a machine-learning-based segmentation technique to predict the exact number of nuclei within each spot (Figures S2D and S2E), and (2) an artificial neural network

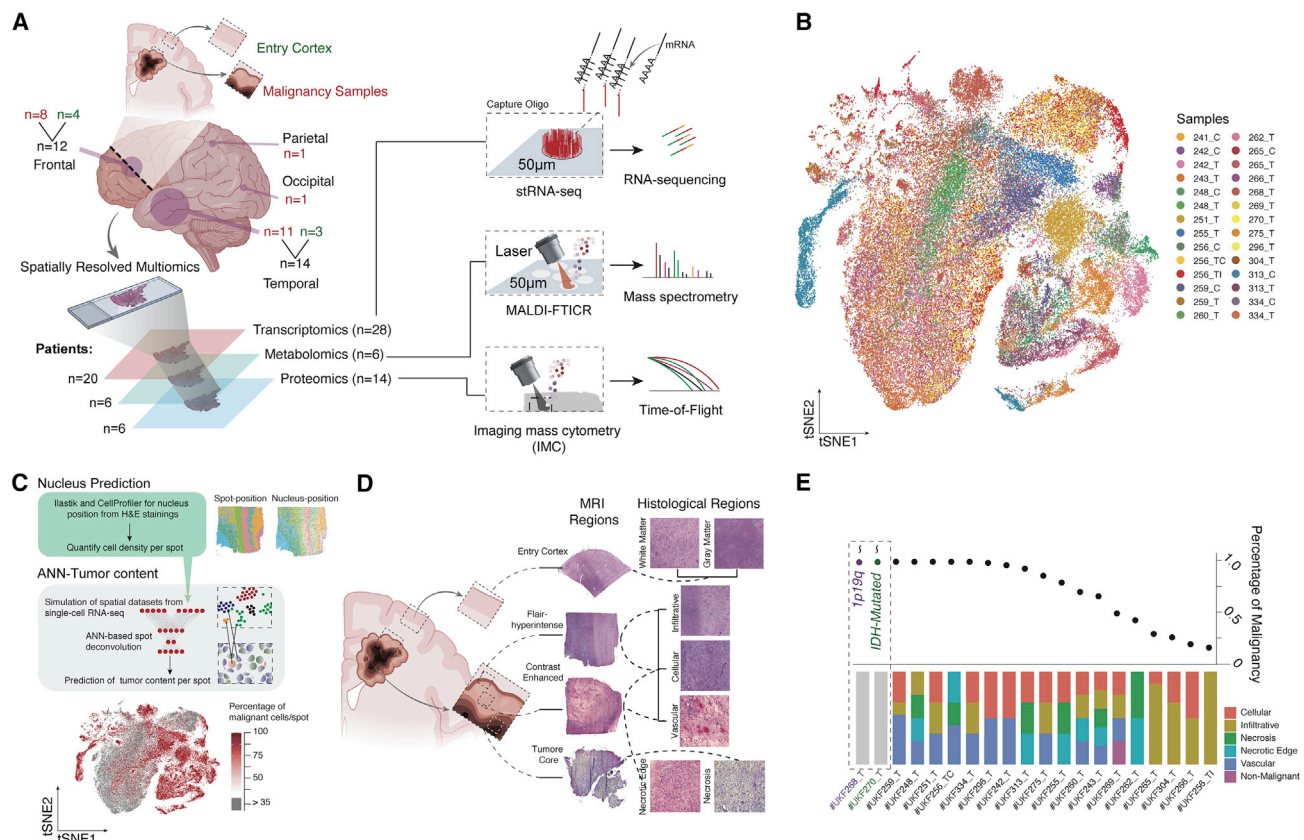


**Figure 1. Overview of the methods and cohort**

(A) Illustration of the workflow and the cohort of spatial datasets (left) and an overview of analytical approaches used (right).

(B) t-stochastic neighbor embedding (tSNE) plot of all integrated spatially resolved transcriptomic spots. Color reflects individual specimens and patients. Numbers indicate the anonymized patient sample ID. The letter indicates the anatomical origin of tissue. T, tumor; TI, tumor infiltrative; TC, tumor core; C, cortex.

(C) Overview of the workflow for prediction of tumor-cell content (top) and tSNE plot (bottom). Colors indicate the percentage of predicted tumor-cell content.

(D) Examples of the different resolutions of histologically defined regions.

(E) Dot plot of the percentage of malignant spots within the stRNA-seq data set based on ANN estimation. At the bottom, barplot illustration of the distribution of histological regions within the samples.

See also [Figures S1–S3](#) and [Table S1](#).

(ANN) model trained to predict the number of tumor cells per spot, based on a simulated dataset consisting of randomized cellular assemblies from paired st-/scRNA-seq datasets ( $n = 5$ ) ([Figures S2G and S2H](#)). From the 88,793 spots from all samples, 63,121 spots were from malignant specimens, of which 46,459 spots contained a minimum of 95% tumor cells ([Figure 1C](#)). This rigorous filtering approach leads to a bias in the downstream analysis, as regions with lower tumor content are not considered. This confounding factor contrasts with the bias resulting from different healthy cell types in spots with low tumor-cell content. Since the focus of this work is on the architecture of tumor heterogeneity, spots with low tumor content were excluded. To investigate infiltrative regions, we followed a different workflow as indicated in [Figures S3A–S3F](#). To enable integration of our results with the prevailing gold standard of the histological classification, we predicted the spotwise histological phenotype in accordance with the Ivy GAP histological classification system ([Figures 1D, S3G, and S3H; STAR Methods](#)). Compared with histopathological characteristics, samples with a low tumor-cell frequency

predominantly contained infiltrative regions where tumor cells within the healthy cortex were poorly delineated ([Figure 1E](#)).

### Deciphering spatially resolved transcriptional heterogeneity

We aimed to identify recurring transcriptional spatial patterns by contextualizing them to existing transcriptional and histological classifications. The spatial localization of GBM transcriptional subgroups, as initially described using bulk RNA-seq ([Phillips et al., 2006; Verhaak et al., 2010](#)) and further characterized in depth using scRNA-seq ([Nefel et al., 2019](#)), remains unclear. We and others ([Li et al., 2020](#)) hypothesize that transcriptional subgroups are spatially segregated and engage in distinct tasks within the tumor. To address the transcriptional diversity in a spatial context, we first elucidated spatially separated transcriptional patterns within individual patients, aggregating these results across the entire cohort ([Figure S3I](#)). To achieve this goal, we sequentially eliminated confounders including inter-patient variability, technical artifacts, and variability in sequencing



depth; an overview of filter parameters is provided in the [STAR Methods](#). Our analysis workflow was composed of three major steps: (1) identification of patientwise robust regional transcriptional programs, (2) horizontal integration across patients using shared transcriptional programs as anchors and spatially weighted correlation to explore colocalization of transcriptional programs, and (3) characterization of the spatial organization of shared programs ([Figure S3I](#)).

Unsupervised clustering was first carried out using five complementary methods ([STAR Methods](#)) to maximize robustness in cluster assignment (*IDH1/2* wild-type GBM,  $n = 16$  patients). We then conservatively retained clusters from further analysis, including partially overlapping clusters, clusters lacking significant signature gene expression, or spots with ambiguous cluster assignments across methods ([Galili, 2015](#)) ([Figures S3J–S3L](#)). This resulted in 38,872 spots across 99 clusters (of all patients), representing stable regional patterns. To further determine recurring transcriptional programs, horizontal integration of the assigned clusters was carried out within transcriptional and cartesian space. Within the transcriptional space, we uncovered five consistently expressed transcriptional programs, later referred to as “spatially distinct transcriptional programs,” distinguished by the presence of each program in 90% of the surveyed tumors ([Figure 2A](#)). In the cartesian space, we subsequently integrated patientwise spatial-weighted correlation matrices (cluster by cluster) followed by a hierarchical clustering, confirming the spatial segregation of the five recurrent spatially distinct transcriptional programs ([Figure 2A](#)). This approach allowed us to understand the biological significance of transcriptional programs among patient-specific clusters that were robustly expressed across the cohort. Exploring these distinct programs, we identified two spatially distinct transcriptional programs that were associated with high expression of glial-related genes (e.g., *GFAP*, *AQP4*, *VIM*, *CD44*). Although both programs indicated glial lineage, one was associated with increased expression of radial-glia-associated genes (*HOPX*, *PTPRZ1*), and the other revealed functional enrichment of inflammation-associated genes (e.g., *HLA-DRA*, *C3*, *CCL4*, *CCL3*) and gene sets (interferon [INF]-gamma signaling, false discovery rate [FDR] < 0.01, hypergeometric test). These programs that shared a common glial transcriptional profile will be further referred to as “radial glia” and “reactive-immune,” respectively ([Figures 2A](#), [S4A](#), and [S4B](#); [Tables S2](#) and [S3](#)). The term reactive is used since these transcription programs are reminiscent of signature genes associated with the reactive transformation of ACs ([Figures S4B–S4G](#)). The remaining transcriptional programs demonstrated substantial concordance with glial lineages and were named according to their neural (termed “neural development”) or oligodendrocytic origin (termed “spatial OPC”), coinciding with the recently described “developmental” signature ([Richards et al., 2021](#)) and the NPC- and OPC-like tumor-cell subgroups ([Nefitel et al., 2019](#)), respectively ([Figures 2C](#) and [S4F](#)). The fifth spatially distinct transcriptional program, further referred to as “reactive-hypoxia,” was identified to be associated with hypoxia-response (e.g., *VEGFR*, *HMOX1*, *GAPDH*) and glycolytic (e.g., *LDHA*, *PGK1*) genes, suggesting that metabolic alterations coupled with low concentrations of oxygen drive a

transcriptionally distinct state in some regions ([Figures 2A](#), [2B](#), and [S4A](#)). We hypothesize that this phenotype is characterized by a dynamic adaptive response, consequently linked to distinct alterations in the microenvironment.

### **Spatially distinct transcriptional states are independent of cell-cycle states and are congruent with existing classification systems**

To determine if the detected spatially distinct transcriptional programs exist across all cell-cycle phases, we classified all spots based on their transcriptional and cell-cycle programs. Akin to the findings from scRNA-seq studies, a lower abundance of spots classified as neuronal development and reactive-hypoxia (ANOVA,  $p < 0.001$ ) was detected in cycling cells (further analysis in a later section). Other programs were equally distributed across all cell-cycle states, highlighting the independence and stability of the detected spatially distinct transcriptional programs ([Figure 2A](#)).

In order to further integrate our findings with existent classification systems, we performed spatial-weighted regression of the established bulk- ([Verhaak et al., 2010](#)), single-cell ([Nefitel et al., 2019](#); [Richards et al., 2021](#)), and our spatially distinct transcriptional program classification to map spatial relationships ([Figures 2C](#) and [S4D–S4F](#)). Bilateral integration of the top-scoring gene signatures of the spatially distinct transcriptional programs was carried out with the scRNAseq dataset from Nefitel et al., confirming that glial-related programs radial glia, spatial OPC, and neuronal development demonstrated strongest overlap with AC-, OPC-, and NPC-like, respectively ([Figure S4A](#)). When compared with the data from Richards et al., all the above programs demonstrated a strong overlap with the neurodevelopmental phenotype ([Figure 2C](#)). The reactive-hypoxia program demonstrated the strongest overlap with the MES-like subtype, specifically the hypoxia-dependent “MES2” state ([Nefitel et al., 2019](#)) ([Figures 2C](#), [S5A](#), and [S5B](#)).

So far, all states demonstrated overlap with exclusive transcriptional programs from scRNA-seq data. However, Nefitel et al. pointed out the presence of a subset of cells that expressed two distinct meta-modules or “hybrid” states. The spatially unique reactive-immune program was found to be associated with a distinct hybrid cell population, spanning between AC- and MES-like states or containing cells from the AC- and MES-like states in close proximity, suggesting that these hybrid states (or interactions between AC- and MES-like states) may reflect spatially segregated functions ([Figures S5A](#) and [S5B](#)). To evaluate the spatial distribution of states and spatially distinct transcriptional programs, we determined Moran’s  $I$  autocorrelation ([STAR Methods](#)). We found that the spatially distinct transcriptional programs were arranged in robust patterns within the cartesian space (quantified by the Monte Carlo simulation of Moran’s  $I$  across all samples, mean spatial classification: 0.62, mean cellular states: 0.38) ([Figure S5C](#)). Additionally, we analyzed the spatial congruence between histological patterns and spatial transcriptional clusters, and a significant enrichment of the reactive hypoxia program was found around histologically necrotic regions (ANOVA and Tukey’s honestly significant difference [TukeyHSD],  $FDR = 3.34 \times 10^{-9}$ ) ([Figures 2A](#) and [S5D–S5F](#)).

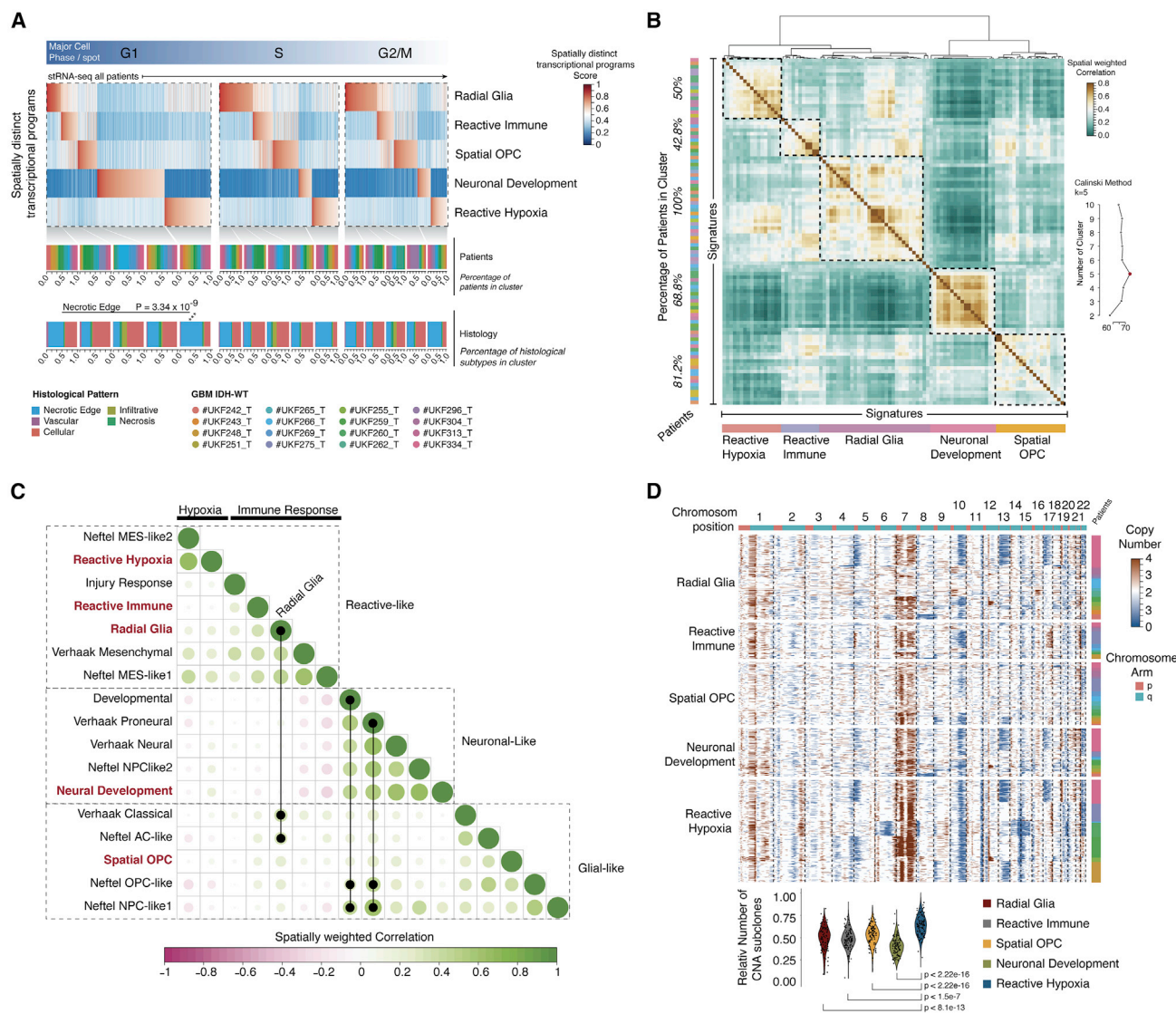


**Figure 2. Exploration of spatially distinct transcriptional programs**

(A) Heatmap of spatially resolved transcriptomics of glioblastoma. Colors indicate the normalized regional program score. Heatmaps are arranged by major cell phase (G1, S, or G2/M). Below the heatmap, patient samples and the histological origin of each spot are illustrated.

(B) Heatmap of the spatial-weighted correlation analysis of the 99 individual transcriptional programs. Hierarchical clustering (Ward.D2) confirmed 5 programs (Calinski method, right) with large spatial congruence. The percentage of programs per patient contributing to each cluster is shown to the left.

(C) Spatially weighted correlation analysis of the enrichment scores and spatial overlap of current transcriptional signatures. By clustering all signatures, three major branches appear: glia-like, neuronal-like, and stress-response reactive signatures. Signatures with high cross correlation are marked by lines.

(D) Heatmap of different CNAs across spatially distinct transcriptional subtypes. In the bar plot at the bottom, we quantified the relative numbers of exclusive subclones that occur only in the defined spatially distinct subgroups. Violin plots represent the relative numbers of unique CNA events (subclones) across spatially distinct transcriptional programs. Significance was determined using Mann-Whitney U test, and p values were corrected for multiple testing using the Bonferroni method.

See also [Figures S4–S6](#) and [Tables S2](#) and [S3](#).

## Spatially distinct transcriptional programs and subclonal architecture

Copy-number alterations (CNAs), including focal amplification of oncogenes or losses of tumor suppressors, are hallmarks of malignant cells that have been reported to drive therapy resistance and tumor relapse (Smith and Sheltzer, 2018). In the known classifications of cellular states (Netel et al., 2019; Richards et al., 2021), unique CNAs have been linked to particular states, het-

erogeneously distributed across individual tumor cells. We investigated the relationship between genomic alterations and spatially distinct transcriptional programs, leveraging inferred CNAs (Figures S6A–S6C). Since the inference of CNAs at the transcriptional level provides only an approximation, we assessed the accuracy of inference by a comparison between spatially resolved DNA/RNA-seq from a recent published dataset, demonstrating reasonable agreement amid the inferred

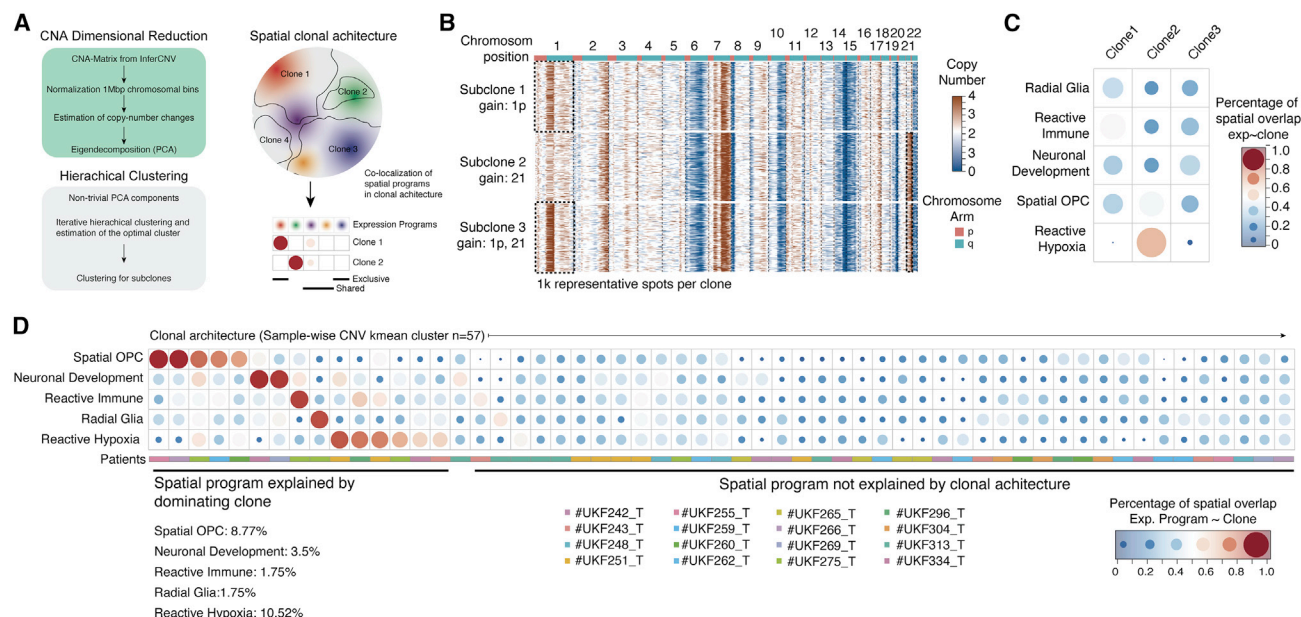


**Figure 3. Transcriptional subgroups are independent of the subclonal architecture**

(A) Overview and illustration of the workflow (left) and an illustration of the concept of spatially shared and exclusive transcriptional programs within subclones.

(B) CNA heatmap of the sample #UKF 260\_T showing 3 dominant subclones.

(C) Dot plot indicating the spatial overlap between transcriptional subgroups (as rows) and subclones (as columns [cols]) from the example #UKF 260\_T as illustrated in (B). Size and color show the percentage of overlap.

(D) Dot plot indicating the spatial overlap between transcriptional subgroups (as rows) and subclones (as cols) from all subclones. Colors at the bottom demonstrate the patients. Size and color showed the percentage of overlap as demonstrated in (C).

and real CNAs, and revealed important thresholds to increase robustness of our inferred method (Figures S6E–S6M; STAR Methods). In reactive-hypoxia-associated spots, we identified a significant accumulation of CNAs that occurred as independent subclonal events ( $p < 2.2 \times 10^{-26}$ ) (Figure 2D).

Next, we aimed to investigate whether the spatially distinct transcriptional diversity could directly reflect genetic subclones within the tumor. We reconstructed clonal architecture by patient-specific hierarchical clustering of CNAs. Fifty-seven genetic subclones were identified, spanning between 2 to 6 subclones per sample (Figure 3A). We then determined the distribution of individual, spatially distinct transcriptional programs within each subclone (Figures 3B and 3C). Our analysis showed that in 26.32% of all subclones, a single transcriptional program dominated (more than 75% of spots per subclone). These findings helped us conclude that clonal architecture has a limited impact on the occurrence of spatially distinct transcriptional programs, although subclones are occasionally biased toward the spatial OPC (8.77%) or reactive-hypoxia program (10.52%) (Figure 3D).

### Metabolic alterations associated with reactive-hypoxia programs in GBM

To further explore the spatially distinct reactive-hypoxia program, we carried out spatially resolved metabolomics using MALDI Fourier-transform ion cyclotron resonance imaging mass spectrometry (MALDI-FTICR-MSI) from tissue sections consecutive to those used for stRNA-seq (patients,  $n = 6$ ) (Figure 4A; Table S1). A workflow similar to that described for the

stRNA-seq to decipher metabolic profiles was implemented, encompassing three major steps: (1) alignment of metabolic and transcriptomic data, (2) patientwise exploration, and (3) reciprocal principal-component analysis (RPCA) integration. Dimensional reduction revealed major variance within the first two principal components, resulting in the identification of three prominent metabolic subgroups post correction for cluster stability (Figures 4A, 4B, and S7). Functional metabolic analysis revealed a significant enrichment of the pentose phosphate pathway ( $FDR = 1.4 \times 10^{-8}$ , hypergeometric test) in the first metabolic module (M-G1). The second metabolic subgroup (M-G2) was characterized by an enrichment of phosphoadenylate metabolism ( $FDR = 3.3 \times 10^{-7}$ , hypergeometric test), described as a hallmark of glioma metabolism (Li et al., 2018). The final metabolic subgroup (M-G3) was strongly enriched for glycolysis ( $FDR = 2.2 \times 10^{-7}$ , hypergeometric test) and amino sugar metabolism ( $FDR = 4.2 \times 10^{-8}$ , hypergeometric test) (Figure 4C).

### Regions of reactive-hypoxia accumulate chromosomal alterations

The spatially distinct transcriptional program reactive-hypoxia, highlighted in this section, appeared as a unique cluster in our integrated analyses (WNN clustering) (Figure 4B). Histologically, most spots assigned to the reactive-hypoxia program represent the necrotic edge (Figure 4C). Although these results are largely expected, and cell-state-specific CNAs have been described in the literature (Neftel et al., 2019), the spatial co-occurrence of metabolic alterations and distinct CNAs is unclear. We



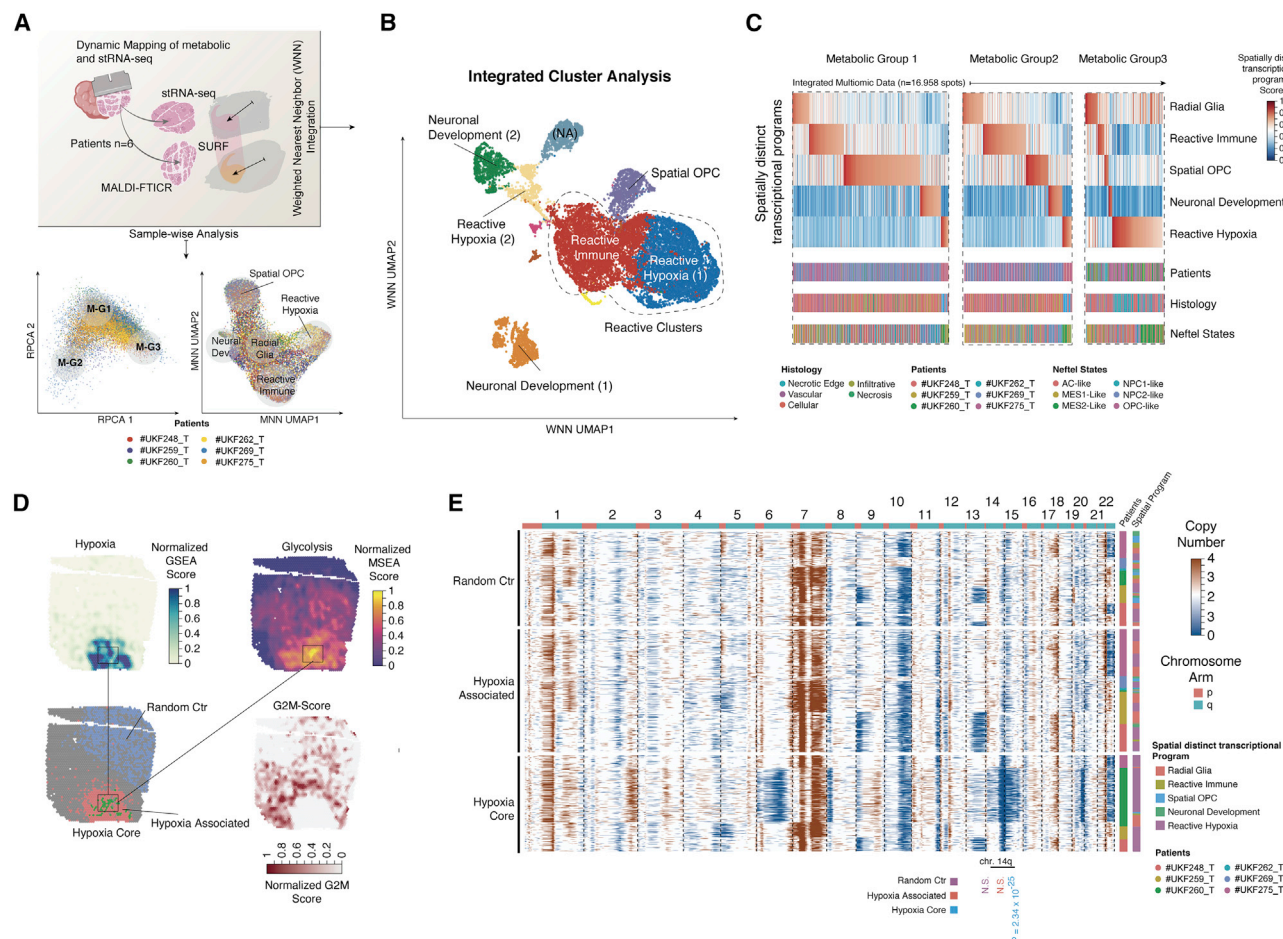


**Figure 4. Integration of spatially resolved metabolomic and transcriptional data**

(A) Illustration of the workflow to integrate transcriptional and metabolomic data from 6 patients. Data analysis was performed by both samplewise comparison and combined vertical and horizontal integration.

(B) Scatter plots of the horizontal integration of metabolomic data across patients using reciprocal PCA (RPCCA 1–2), and the horizontal integration of transcriptomic data using mutual nearest neighbor (MNN) integration (MNN uniform manifold approximation and projection [UMAP] 1–2). Both data are integrated by the weighted nearest neighbor (WNN) followed by dimensional reduction (WNN UMAP 1–2) indicated in the scatter plot. NA clusters are not further specified.

(C) Heatmap of spatially resolved transcriptomics of all integrated spots. Colors indicate the normalized regional program score. Below the heatmap, bar plots show the individual distribution of characteristics within the spatial distinct subgroup.

(D) Surface plots of the integrated analysis in sample #UKF 275\_T. At the top, hypoxia transcriptional activation is shown (left), and the metabolic activation (from MALDI) is indicated at the right. At the bottom, hypoxia-associated spots are indicated in red and hypoxia core in green. Random spots are shown in blue. The boxes connect the same spatial positions. At the bottom right, the enrichment score for cell cycle (G2M) is demonstrated.

(E) Copy-number heatmap across hypoxia phenotypes. A significant alteration was tested by Wilcoxon and corrected by FDR.

See also Figure S7.

hypothesized that hypoxic metabolism leads to accumulation of genomic instabilities in spatially segregated niches. These “reactive islands” represent potential sources of *de novo* genomic alterations aiding in the evolution of therapy resistance by the tumor cells. This is in line with reports on hypoxia-driven genomic instabilities and epigenetic remodeling supporting tumor evolution and therapy resistance in glioma (Garofano et al., 2021; Johnson et al., 2021) and other cancer types (Bhandari et al., 2020; Luoto et al., 2013; Sharma et al., 2010). Hypoxia has been shown to result in altered expression of DNA-damage-response and -repair genes, resulting in inhibition of recombination-mediated repair of DNA double-strand breaks, increasing mutation rates and CNAs (Luoto et al., 2013).

To investigate our hypothesis, we explored areas enriched for reactive-hypoxia signatures. Regions were defined as either hypoxia-core (defined by bilateral hypoxia: MALDI and stRNA-seq) or hypoxia-associated regions (unilateral-hypoxia MALDI or stRNA-seq) with enrichment for glycolysis pathway (Figure 4D). CNA mapping across both hypoxia-core and hypoxia-associated regions versus randomly chosen control spots revealed a significant loss of chromosome 15p (ANOVA, FDR =  $4.15 \times 10^{-17}$ ) and 14q (ANOVA, FDR =  $2.34 \times 10^{-25}$ ) and gain in chromosome 7 (ANOVA, FDR =  $1.74 \times 10^{-6}$ ) in hypoxia core regions. Some samples also displayed singular losses and gains across multiple chromosomes (8p, 9p, 13q, 19q, and 21q), the variability most likely explained by single subclones within hypoxic core areas, lending



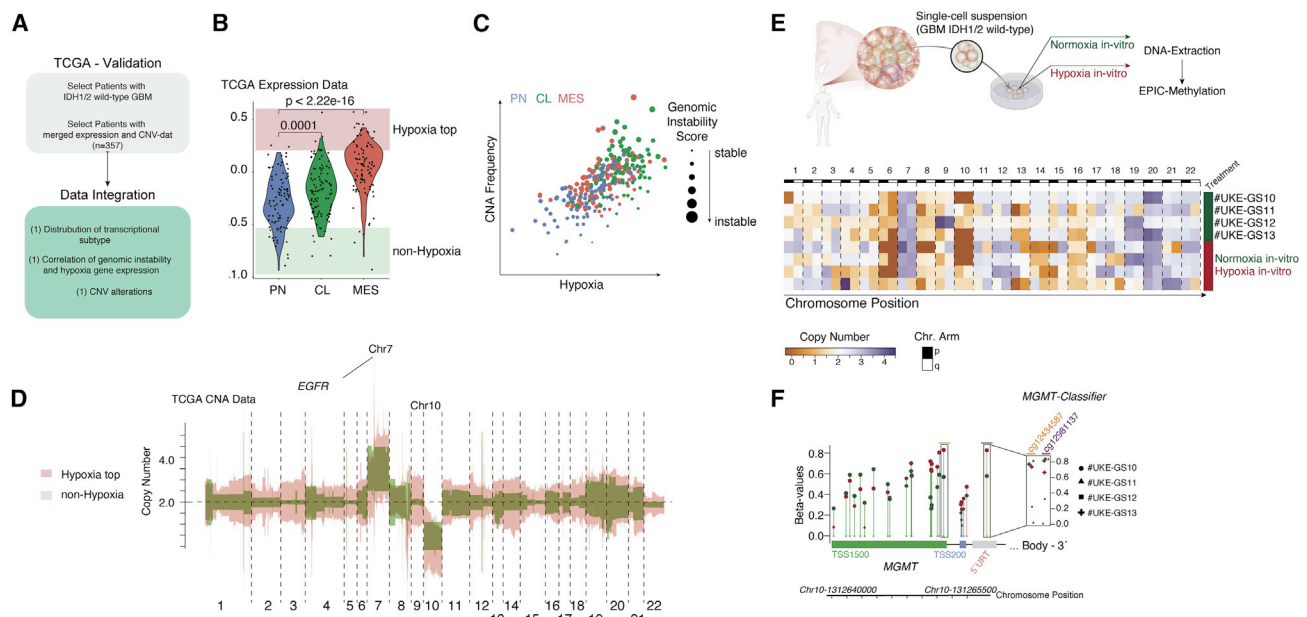


**Figure 5. TCGA and cell-culture validation of hypoxia-associated CNA alterations**

(A) Overview and workflow of the TCGA data analysis.

(B) TCGA data validation. Patients were grouped by hypoxia score (from gene expression) and transcriptional subgroups (top left). Violin plots show the reactive hypoxia score within the transcriptional subgroups: MES, mesenchymal; PN, proneural; CL, classical. Significance was tested by one-way ANOVA.

(C) Scatterplot of CNA frequency and hypoxia score. Point size indicates genomic instability, based on mutational load and CNAs.

(D) CNA mapping from TCGA data across the whole genome with overlapping hypoxia (indicated in red) and non-hypoxia (indicated in green) scores.

(E) Experimental validation of primary cell cultures of 4 patients cultured either in hypoxic or normoxic conditions. Illustration of the experimental workflow (top). CNA mapping from 850,000 methylation data showed a stochastic accumulation of *de novo* CNAs under hypoxia.

(F) CpG islands at the MGMT TSS1500 – 1<sup>st</sup> exon. y axis shows the methylation beta values. The lollipop plot shows the differential methylation between hypoxia-stress response at the MGMT promoter. Colors of the dots indicate the sample origin, hypoxia treatment (red) or normoxia (green). Colors of the boxes (bottom) indicate the chromosomal region. The MGMT CpG islands (cg12434587 and cg12981137) were statistically tested using a one-way ANOVA.

credence to the hypothesis that hypoxia-associated metabolism is a potential driver of genomic instability (Figure 4E). In particular, a chromosome 14q loss has been reported in other hypoxia-driven cancers such as renal (Monzon et al., 2011) and pancreatic cancers (Tiwari et al., 2020). Both hypoxia-inducible factor (*HIF1A*) and L-2-hydroxyglutarate dehydrogenase (*L2HGDH*) are located on chromosome 14q, and its loss was linked to poorer survival in patients suffering from renal cancer (Monzon et al., 2011). Also, the loss of *L2HGDH* has been demonstrated to be a potential driver of epigenetic remodeling in renal cancers (Shim et al., 2014). To further validate our findings, we analyzed samples sourced from the TCGA database (patients GBM IDH1/2 wild-type n = 357), classifying patients based on their hypoxia-gene expression score (Figures 5A and 5B). Hypoxia-driven tumors showed a significant increase in chromosomal alterations, confirming our initial observation and further strengthening the relationship between metabolism and genomic instability (Figures 5C and 5D). The defined loss of chromosome 15q/14q has not been demonstrated in the TCGA data nor in the recently published single-cell studies in the context of hypoxic activation, suggesting that our results are likely confounded by the small number of investigated samples. Thus, our results primarily indicate that hypoxic/oxidative stress enhances genomic instabilities, serving to enforce microevolution towards resilience in GBM, supported by subclonal selection. To experimentally validate our hypothesis, we cultured primary-patient-derived GBM cell lines under both normoxia and hypoxic

conditions for 2–6 weeks (patients n = 4) (Figure 5E). Copy-number variations revealed differences in CNA profiles, with a significant accumulation of CNA events under chronic hypoxia conditions confirming the hypothesis of stress-induced CNA alterations (Figure 4E). A recent report by Johnson et al. demonstrated a link between metabolic-epigenetic and genetic changes and showed that DNA-methylation disorders are associated with CNAs (Johnson et al., 2021). With this in mind, we explored the impact of hypoxia metabolism on DNA methylation by analyzing O-6-methylguanine-DNA methyltransferase (*MGMT*) promoter methylation at CpG sites cg12434587 and cg12981137 under normoxia and hypoxia conditions. Cell lines with an unmethylated *MGMT* promoter under normoxia developed hypermethylation when exposed to hypoxia (Figure 5F). These findings further strengthen our hypothesis of metabolism-driven CNAs, where most *de novo* rearrangements must be considered as stochastic random events, contributing to the subclonal evolution of the tumor.

### Hypoxia metabolism regulates “go or grow” potential in GBM

In our initial characterization of spatially resolved transcriptional programs, we reported that the reactive-hypoxia program is significantly enriched in non-cycling cells (Figure 2A). This is consistent with recent reports, suggesting that hypoxic stress triggers cell-cycle arrest, in particular an S-phase arrest (Seim et al., 2003) (Figure 6A). This observation was pronounced in

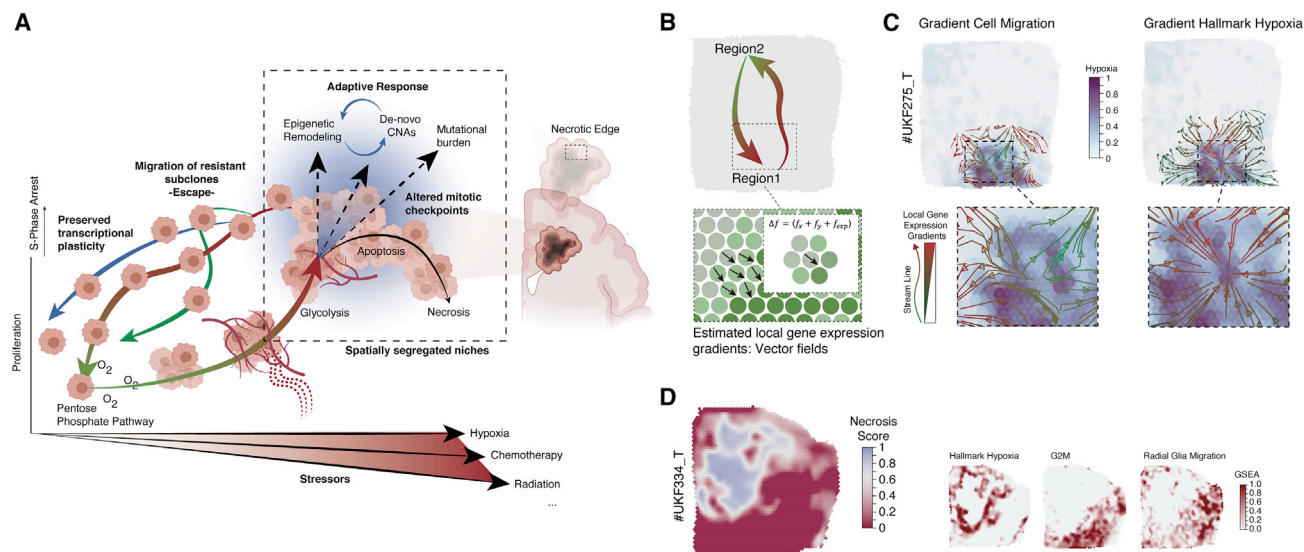


**Figure 6. Illustration of the hypoxia-stress concept and escape mechanism**

(A) Concept and model of proliferation-hypoxia interdependence hypothesis. First, increasing proliferation causes metabolic imbalance of growth and regional hypoxia. Hypoxia-induced termination of the cell cycle is associated with retention in the S phase and consecutive accumulation of CNAs. Second, cells acquiring such a potential resistance advantage can gradually migrate out of the hypoxic areas.

(B) Model of vector-field calculations, which consist of the aligned gradients of spatial shifts in gene-expression levels and indicate the direction of migratory activation.

(C) Surface plots of a spatial transcriptomic example (#UKF275\_T). Arrows indicate the vector fields (illustrated as streamlines) from defined transcriptional programs. For the illustration, we calculated vector fields consisting of the aligned gradients of spatial shifts in gene-expression levels. By placing the spots within fixed spatial grids, we calculated an approximation of spatial trajectories.

(D) Surface plots (#UKF334\_T) indicating the relationship between necrosis (left plot) and the enrichment of hypoxia (2<sup>nd</sup> from left), cell cycle (G2M 3<sup>rd</sup> from left), and radial glia migration (last from left).

the hypoxia-core spots, leading to the hypothesis that hypoxia-driven S-phase arrest contributes to the accumulation of genomic instabilities (Figure 6A), which is supported by previously reported findings that stress response and alterations in mitotic checkpoints leads to aneuploidy (Zhu et al., 2018). Combining recent evidence and our integrative analysis, we propose the following hypothetical model.

The baseline transcriptional state of GBM cells can be assigned to “developmental” (AC-, OPC-, or NPC-like) programs (Bhaduri et al., 2020; Couturier et al., 2020; Richards et al., 2021). Spatially, these programs are linked to lower cellular density, with metabolic profiling revealing an enrichment of the pentose phosphate pathway (PPP). Due to proliferation and tumor growth, increasing nutrient and oxygen deficiency occurs, forcing the adoption of metabolic programs toward glycolysis. This phenomenon, a reciprocal switch between PPP and glycolysis, has been linked to the go or grow potential of tumor cells (Kathagen et al., 2013), suggesting that the PPP dominates regions consisting of growing tumor cells. When oxygen deficiency occurs, this hypoxia-induced switch to glycolysis subsequently leads to the induction of the go program, which facilitates the escape/migration of cells to normoxic regions, (Kathagen et al., 2013). Due to the downregulation of cell-cycle programs that occurs under hypoxic conditions, an arrest in the S phase occurs, leading to subsequent accumulation of *de novo* CNAs (Seim et al., 2003). We hypothesize that a large percentage of these hypoxia-affected cells then enter apoptosis, resulting in the characteristic necrosis seen in GBM. Only a small fraction

of cells managing to escape by employing the upregulation of migration-associated transcriptional programs (Kathagen et al., 2013). Besides hypoxia, other stressors such as radiation or chemotherapy have been reported to cause such stress-related perturbations in GBM (Johnson et al., 2021) (Figure 6A).

Based on our model, one should expect to see an inverse relationship between hypoxia metabolism and cellular migration. To explore the enrichment of migratory gene-expression signatures in metabolically altered regions, we determined the spatial orientation of directed gradients between low and high enrichment of specific gene-expression signatures. Simplified, the orientation vector of each spot is based on the graded enrichment of the investigated gene-expression signature in its local neighborhood. These vector-field calculations allow us to approximate spatial gene-expression trajectories, enabling the identification of spatially opposing transcriptional pathways (Figure 6B). Based on these vector-field calculations, we report that hypoxia response and migration signatures show inversely directed spatial trajectories (Figures 6C and 6D). In summary, our findings provide evidence for metabolic changes and oxidative stress being potential reciprocal drivers of genomic diversity, resulting in clonal evolution in GBM.

### Exploration of tumor-host interdependence in the reactive-immune regions

Besides hypoxia-associated environmental stressors leading to spatially segregated niches, another major stressor of GBM is the immune environment, the understanding of which is essential

for the development of successful immunotherapy treatments. Immunoediting within the tumor is a decidedly important trait that ensures immune escape and leads to a lack of effective immunotherapeutic options for GBM (Filley et al., 2017). Recently, evidence has been presented on epigenetic reprogramming of MES-like tumor cells reshaping the microenvironment (Gangoso et al., 2021). Accordingly, enrichment of dysfunctional (exhausted) T cells has been observed and reported in MES regions of GBM (Hara et al., 2021; Mathewson et al., 2021; Ravi et al., 2022). Initial exploration of the spatially distinct transcriptional programs showed that the reactive-immune classification was composed of cells enriched for both the MES-like (MES1) and the astrocytic-like (AC) transcriptional signatures, also described as the “MES-AC-hybrid” states (Figure 2B).

In order to provide a holistic perspective of the tumor-immune interdependence, we complemented our findings with imaging mass cytometry (IMC)-based single-cell profiling. We carefully selected ROIs within regions of reactive-immune and reactive-hypoxia programs and control ROIs from regions classified as neuronal differentiation. IMC data were acquired from tissue sections consecutive to those used for stRNA-seq ( $n = 6$  patients, 14 different  $1,000 \mu\text{m}^2$  ROIs), resulting in a comprehensive proteomic map of 82,179 cells post segmentation (Figure 7A; Table S4). Our analysis revealed a significant increase of myeloid ( $p_{\text{adj}} < 0.01$ , multivariate ANOVA [MANOVA]) and lymphoid cells ( $p_{\text{adj}} < 0.01$ , MANOVA) in the regions classified as reactive-immune (Figure 7B, 7C, and S8A–S8C). To investigate the tumor-cell differentiation in immune-enriched areas, we quantified the cellular diversity by subdividing cells into radial glia (EGFR<sup>+</sup>HOPX<sup>+</sup>), reactive-immune (EGFR<sup>+</sup>CHI3L1<sup>+</sup>VIM<sup>+</sup>), spatial OPC (EGFR<sup>+</sup>OLIG1<sup>+</sup>), neural development (EGFR<sup>+</sup>SNAP25<sup>+</sup>CALM2<sup>+</sup>), and reactive-hypoxia (EGFR<sup>+</sup>VEGFA<sup>+</sup>). An exclusive enrichment of reactive-immune (EGFR<sup>+</sup>CHI3L1<sup>+</sup>VIM<sup>+</sup>) cells was confirmed only in transcriptionally defined reactive-immune localizations (Figure 7B).

To complement our findings pertaining to the cellular relationships between the immune system and GBM, we aimed to model cellular interdependence (STAR Methods). We quantified cellular connectivity between tumor cells and lymphoid or myeloid cells based on their distance, confirming enhanced cellular interactions between tumor cells and the immune compartment in transcriptionally defined reactive-immune areas (Figure 7D, bottom). Next, we explored the distribution of cell types within the different ROIs. We confirmed the suspected enrichment of AC- and MES-like cells in both reactive-immune ( $p_{\text{adj}} = 1.32\text{e-}6$ ) and hypoxia ( $p_{\text{adj}} = 2.61 \times 10^{-9}$ ) ROIs. OPC-like cells were mainly enriched in neural development ( $p_{\text{adj}} = 3.15 \times 10^{-12}$ ) ROIs (Figures 7E and 7F). Additionally, both reactive-immune and hypoxia areas revealed a significant enrichment of tumor-associated myeloid cells (TAMs) and T cells (Figure 7G). Given that T cells are enriched in both reactive areas, we investigated the mean PD-1 protein levels on T cells (CD3<sup>+</sup>), which were significantly increased within reactive-immune areas compared with reactive-hypoxia ( $p = 0.023$ ) and neural development ( $p = 0.034$ ) areas, suggesting a local enhanced immunosuppression in reactive-immune ROIs (Figure S8A). These findings were further supported by the observation of local enrichment of CD163<sup>+</sup> myeloid cells in reactive-immune areas,

which was reported to support anti-cancer immunity (Ravi et al., 2022) (Figures S8B and S8C). Additionally, spotwise projection of an scRNA-seq dataset representing the GBM immune landscape (STAR Methods) confirmed the enrichment of both memory and exhausted T cells in the reactive-immune areas of the tumor (Figure 7H).

### Environmental conditions contribute to a bidirectional subtype shift

Our findings so far have shown that the microenvironment plays an important role in the transcriptional plasticity exhibited within GBM. Evidence of these findings has been previously reported as well, with a multitude of studies showing that an inflammatory environment drives transcriptional adaptation, leading to GBM heterogeneity (Gangoso et al., 2021; Hara et al., 2021; Mathewson et al., 2021). Metabolic alterations such as hypoxia have been implied to bias differentiation towards a MES-like state (Heiland et al., 2018; Joseph et al., 2015); however, it is unclear if this is reversible. A bidirectional shift between subclasses was described based on alterations within the tumor (Rooj et al., 2017), yet limited evidence has been presented on the impact of the local microenvironment on the various transcriptional programs. Our hypothesized model and results suggest that a part of these metabolically or immunologically affected cells, here described as the reactive phenotype, will escape and migrate toward healthy parts of the brain. To follow our hypothesis that the microenvironment causes defined transcriptional reprogramming in tumor cells, we aimed to investigate to what extent reactive-transformed cells will change when exposed to healthy brain. Due to the limited spatial resolution of the stRNA-seq technology, exploration of infiltrating cells is not possible; therefore, we performed scRNA-seq in the last part of our work.

At this stage, information about expressed transcriptional programs was of priority; therefore, we simulated tissue infiltration by means of our previously established human organotypic neocortical-tissue-based GBM model, devoid of both metabolic and immune stress. To assess the impact of various microenvironments, we used cortical access tissue from multiple human donors of different ages (2–85 years of age, patients  $n = 3$ ; sections  $n = 48,16$  per patient) and two murine donors from 2-week- and 2-year-old rats ( $n = 32$  sections) (Figure 8A). The tissue was cultured for 4 days as previously described (Maier et al., 2021; Ravi et al., 2019), after which the same MES-like primary-patient-derived cell line (characterized by RNA-seq [Schneider et al., 2021]) was inoculated into all cultured tissue sections (Figure 8A). After 7 days of culture in different host environments, the tissue was digested, and tumor cells were isolated using FACS for transcriptional profiling using scRNA-seq (15,034 cells). Computational identification of tumor cells was carried out based on their characteristic gains in chromosome 7 (10,887 cells) using inferred CNAs (Figures 8C and 8D). To explore the dynamic adaptation across different host environments, all malignant cells were aligned based on enrichments of their corresponding cellular states (Figures 8E and 8F). The baseline state (cells grown in two-dimensional [2D] cell culture) revealed an MES-1/2-like phenotype (chi-squared test,  $p < 2.2 \times 10^{-16}$ ), with a low degree of transcriptional diversity and plenty of cycling cells (Figure 8E). Developmental states



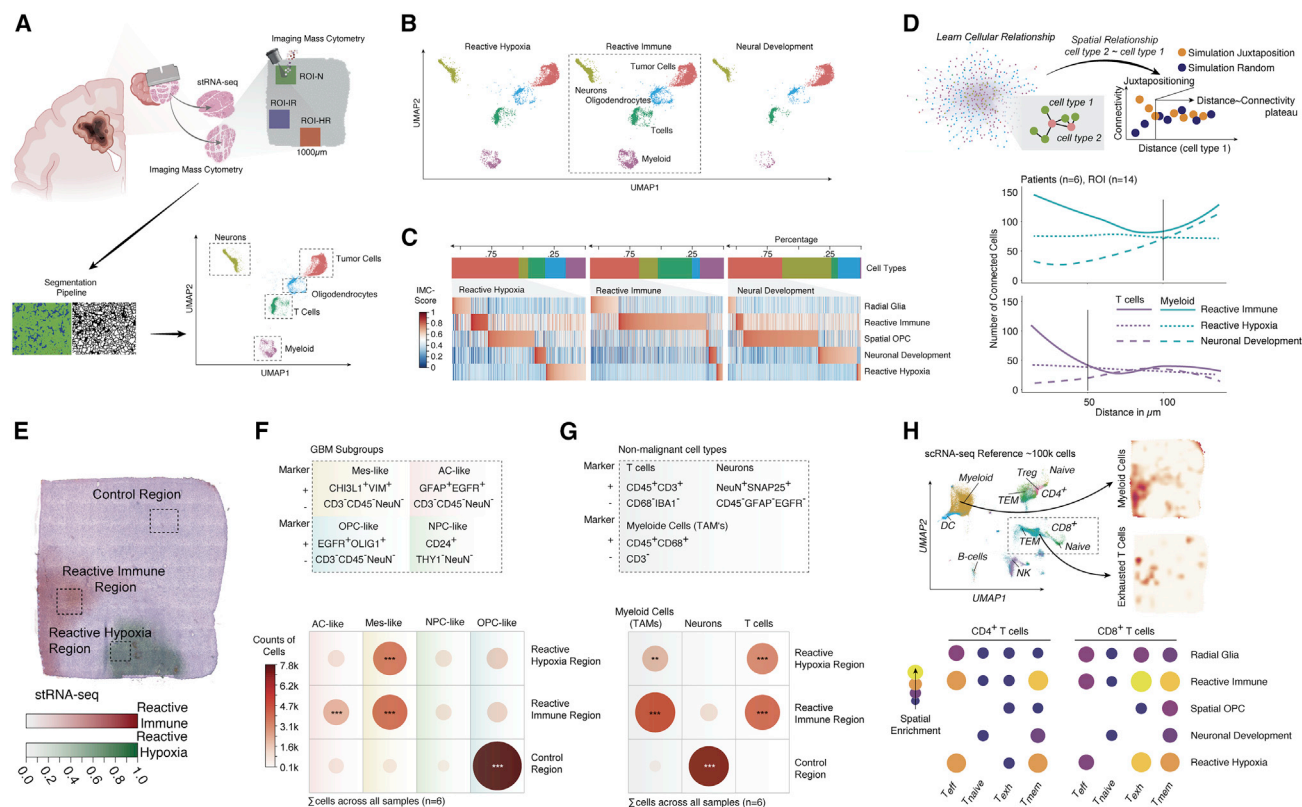


**Figure 7. Integration of single-cell mass cytometry**

(A) Illustration of the integration of imaging mass cytometry data within the spatial transcriptomic data. Based on the defined transcriptomic niches (see also Figure 2), defined areas were selected for IMC. At the bottom is an illustration analysis pipeline for IMC data.

(B) Dimensional reduction of the cell-type diversity in different areas of dominating spatially resolved transcriptional patterns.

(C) Bar plots of the changes of lymphoid and myeloid cells across spatially resolved transcriptional patterns (top). Heatmap of tumor-cell diversity of our annotated spatially resolved subtypes (bottom).

(D) Illustration of the workflow for the quantification of cellular relationships (top). Quantification of the cellular connectivity between tumor cells and myeloid (cyan) or lymphoid (purple) cells (bottom).

(E) An H&E of the #UKF275 is presented as an example. A colored mask indicates the distinct reactive immune (red) and hypoxia regions (green).

(F and G) Illustration of the cell counts per subregion and cell type. Counts and statistic for tumor cells are illustrated in (F) and non-malignant cells in (G). Statistics were performed by ANOVA, and the p value is corrected (FDR) and illustrated as \*\*\*p < 0.001, \*\*p < 0.01, \*p < 0.05.

(H) Deconvolution of the cellular position of myeloid cells (top right) and effector T cells as an example. At the top, a 2D representation of the glioblastoma immune compartment is presented. The dataset is merged from three recently published datasets (STAR Methods). At the bottom is a heatmap of spatial enrichment (spotlight score per region across all tumor samples) for CD4<sup>+</sup> and CD8<sup>+</sup> T cell subtypes. T<sub>eff</sub>, effector T cells; T<sub>mem</sub>, central and effector memory T cells; T<sub>exh</sub>, exhausted T cells; T<sub>naive</sub>, naive T cells. Blank fields illustrate no detectable enrichment of cell types.

See also Figure S8 and Table S4.

(OPC-, AC-, and NPC-like) were significantly over-represented in cells cultured in human donor tissue, primarily in the young- and middle-aged donors ( $\frac{2}{3}$ ) (MANOVA p <  $2.2 \times 10^{-16}$ ). GBM cells cultured in the rodent neural environment exhibited enrichment for MES-1/2- and AC-like transcriptional signatures (MANOVA p <  $2.2 \times 10^{-16}$ ). Cycling cells of the developmental states were only detectable in the OPC-like subgroup, which is in line with recent reports (Neffel et al., 2019; Tirosh et al., 2016a; Venteicher et al., 2017). In order to examine dynamic adaptations, we annotated scRNA velocity according to the first two principal components (Figure 8G). Macro states including initial and terminal states were estimated by Markov chains based on annotated RNA velocity and transcriptomic similarity (CellRank [Lange et al., 2020]; Figure 8H). In general, the estimated vector field from the *in vitro* cell-culture root

(Figures 8G and 8H, top) to the MES- and AC-like tail (Figures 8G and 8H, bottom) represents a directional adaptation driven by the neural environment. Protein tyrosine phosphatase receptor type Z1 (*PTPRZ1*), a common marker gene of radial-glia-differentiated GBM cells (Bhaduri et al., 2020), happened to be assigned to a high velocity in the MES-AC-hybrid state based on its phase portrait (Figures 8G and 8H, bottom, and 8I). Our data confirmed a bidirectional fate within the OPC- and NPC-like branches. Genes such as those encoding potassium channels (*KCNH8*) and metabotropic glutamate receptors (*GRM3*) demonstrated high velocity within these transcriptional modules, suggesting that the neuronal environment promotes defined transcriptional programs, which is in line with recent descriptions of neuronal-glioma interactions (Venkataramani et al., 2019; Venkatesh et al., 2019).



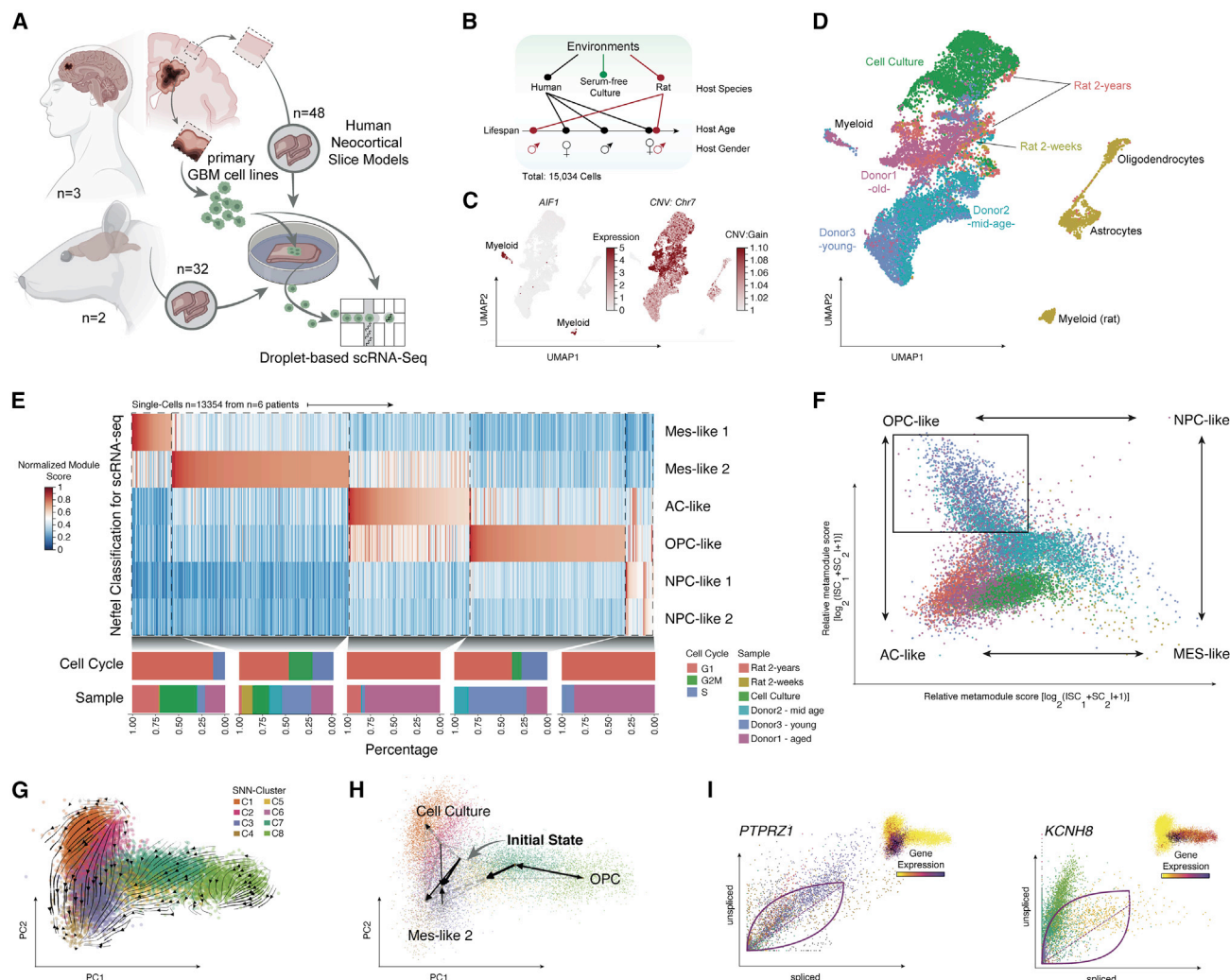


**Figure 8. Ex vivo human cortical culture indicates the bidirectional shift through environmental impact**

(A) Illustration of the workflow to test the impact of varying host environments on tumor cells.  
 (B) Overview of the host environments.  
 (C) Dimensional reduction UMAP 2D representation of scRNA-seq marked by AIF1 (myeloid cells) and gains in chromosome 7 (tumor cells).  
 (D) Dimensional reduction UMAP 2D representation of all integrated scRNA-seq data. Colors indicate the host environment in which the cell was cultivated.  
 (E) Enrichment analysis of transcriptional subtypes, and the heatmap indicates the enrichment score of each cell. At the bottom, the percentage of cells per subgroup and the environmental condition are illustrated.  
 (F) Volcano plot of the four major cellular states described by Neftel et al. (2019). Colors indicate the tissue-donor origin.  
 (G) Velocities derived from the dynamical model for the scRNA-seq data are demonstrated as PCA dimensional reduction. The main gene-averaged flow visualized by velocity streamlines corresponds to the tumor cell differentiation after injection within different tissue donors.  
 (H) Estimation of initial and terminal states using CellRank in a representation similar to (G).  
 (I) Scatter plots of unspliced gene expression (y axis) and spliced gene expression (x axis) demonstrate transcriptional dynamics of splicing kinetics within different clusters. *PTPRZ1* shows upregulation in the MES-like 2 cell state and *KCNH8* within the OPC-state as indicated by the PCA plot at the top right corner. See also Figure S8.

Estimation of the velocity length confirmed the accentuated speed of differentiation in cells from tissue sections compared with cell-culture conditions, highlighting the transcriptional plasticity of GBM cells (Figures S8D and S8E). Of note, we found a significant enrichment of MES-like/reactive cell types in neural environment of elderly donors (human and rat, chi-squared test  $p < 2.2 \times 10^{-16}$ ), whereas cells from phylogenetic lineage-differentiated origins were predominantly enriched in younger donors (chi-squared test

$p < 2.2 \times 10^{-16}$ ). This observation showed a considerable correlation of age-associated effects, potentially based on the enhanced baseline inflammatory state found in the aged brain (Sankowski et al., 2019). Still, the causality of the impact of age on tumor differentiation has not been described. Our data provide clear evidence that the host environment, in addition to known factors such as the mutational and epigenetic landscape, has a significant impact on the plasticity of transcriptional heterogeneity.

## DISCUSSION

Over the last few years, numerous discoveries made through technological advancements in single-cell profiling have revolutionized the understanding of tumor heterogeneity and plasticity and potential therapeutic options (Darmanis et al., 2017; Neftel et al., 2019; Richards et al., 2021; Tirosh et al., 2016a; Venteicher et al., 2017). However, the significance of the spatial organization of brain tumors has not been investigated. Here, we uncovered insights into the bi- and unidirectional interactions between the microenvironment and the spatio-temporal alterations in transcriptional heterogeneity of GBM. We exposed the existence of five spatially distinct transcriptional programs marked by shared transcriptional signatures and exclusive genomic alterations. Although there are prior descriptions of CNAs in GBM, neither the regional pattern nor the association with transcriptional programs has been previously reported. To allow for an overall comparison between the cellular states, histological patterns, and spatially exclusive transcriptional programs, we subsequently contextualized our results within established classifications, revealing a large overlap, although significant differences were found in the context of transcriptionally reactive/MES cells.

This comprehensive characterization of GBM at various molecular levels in a spatially resolved manner facilitates the discovery of dynamic adaptations of cellular states and their spatial relationships within the tumor microenvironment. Our data suggests that metabolic alterations such as severe hypoxia results in impaired proliferation, following a halt in the S phase, that leads to a significant accumulation of CNAs. This phenomenon has been reported in other cancer types, and sufficient evidence exists detailing the increase in genomic instability under hypoxia (Jing et al., 2018; Sieber et al., 2003). Our results and validations in 2D cell culture and TCGA data indicate that regional hypoxia metabolism represents a potential reservoir of genomic instability and represent drivers of microevolution that enable the evolution of therapy-resistant phenotypes. Our results are not able to prove causal relationships but provide a basis for the development of hypothetical models that require mechanistic validation.

A unique spatially exclusive transcriptional program was found in regions of increased immune infiltration by myeloid and lymphoid cells. This defined response of glioma cells has been recently described, indicating that tumor cells undergo epigenetic regulation to express MES-associated genes (Gangoso et al., 2021). Model systems for investigating tumor-host interactions are naturally limited due to the restricted accessibility of human tissue. However, to approximate physiological conditions, we used human neocortical tissue sections that preserve all spatial and cellular architecture of the neural environment. Inoculation of patient-derived primary glioma stem-like cells into different human and rodent host environments confirmed the impact of the microenvironment on tumor-cell differentiation. Within our model, we found a strong association between inflammatory response and the age of the donor, suggesting that aging may have an impact on tumor differentiation, analogous to the reactive transformation of glial cells with age (Senatorov et al., 2019). Several neurological diseases such as Alzheimer's disease (AD) and multiple sclerosis (MS) cause a general inflama-

tory environment, driving inflammatory transformation of glia cells (Liddel and Barres, 2017; Liddel et al., 2017; Yun et al., 2018). An increase in inflammatory transformation was also reported in the aging brain, which could be caused by damage to the blood-brain barrier (Habib et al., 2020). In the present setting, the model suggests a correlation between aging and inflammation in GBM without proving the causality.

In conclusion, we have elucidated the spectrum of regional transcriptional programs of GBM and mapped their microenvironmental landscape including metabolic and tumor-host cellular interactions. By demonstrating that the host environment plays an important role in reshaping the genetic and transcriptional heterogeneity, we provide insight into inter-patient heterogeneity and, consequently, for early GBM relapse and therapy resistance. We conclude that tailored therapeutic approaches are required, highlighting the significance of personalized approaches in neuro-oncology.

## STAR★METHODS

Detailed methods are provided in the online version of this paper and include the following:

- KEY RESOURCES TABLE
- RESOURCE AVAILABILITY
  - Lead contact
  - Materials availability
  - Data and code availability
- EXPERIMENTAL MODEL AND SUBJECT DETAILS
  - Patient samples
  - Cell lines
  - Rat tissue samples
- METHOD DETAILS
  - Spatial transcriptomics
  - Tissue collection and RNA quality control
  - Spatial gene expression protocol
  - MALDI-FTICR-MSI
  - Human organotypic slice culture
  - Human ex-vivo glioblastoma model
  - Single cell suspension from cultured slices
  - Cell sorting for scRNA-seq
  - Single cell RNA-sequencing
  - Imaging mass cytometry antibody panel
  - Sample preparation and staining for imaging mass cytometry
  - Image acquisition
  - Hypoxia treatment and methylome analysis
  - Data import, preprocessing, filtering, and normalization for spatial data analysis
  - Detection of cell number per spot
  - CNA estimation
  - CNA subclone analysis
  - Prediction of tumor cell content
  - Determination and prediction of the histological context
  - Sample-wise cluster analysis for spatially resolved transcriptomics
  - Horizontal integration and identification of spatially distinct transcriptional programs

- Pathway analysis of gene sets
- Spatial gene expression
- Spatial autocorrelation Moran's I
- Spatially weighted regression analysis
- Analysis of spatially defined trajectories
- Estimation of regional gene expression variance by local vector field estimation
- Identification of cycling cells
- CNA analysis from EPIC data
- Methylation analysis of the MGMT promotor
- MALDI data analysis
- Alignment of metabolic and stRNA-seq data
- Data integration and clustering of metabolic data
- Determination of hypoxia subgroups
- Integrative cell cycle analysis and hypoxia metabolism
- TCGA data analysis
- Analysis of scRNA-seq
- RNA velocity estimation (single-cell data)
- Infer lineage differentiation by CellRank (single-cell data)
- IMC preprocessing
- IMC data integration
- IMC neighborhood analysis
- Integration of single-cell sequencing data into spatial transcriptomics

## ● QUANTIFICATION AND STATISTICAL ANALYSIS

## SUPPLEMENTAL INFORMATION

Supplemental information can be found online at <https://doi.org/10.1016/j.ccell.2022.05.009>.

## ACKNOWLEDGMENTS

This work was supported in part by the Else Kröner-Fresenius Foundation (D.H.H.); MEPHISTO project BMBF (German Ministry of Education and Research, project number 031L0260B, D.H.H. and D.D.); the Deutsche Forschungsgemeinschaft (DFG, German Research Foundation, project number SFB 824C04, A.K.W.); BMBF (Bundesministerium für Bildung und Forschung (project number FMT 13GW0230A, U.G.H.); and the Fördergemeinschaft Kinderkrebs-Zentrum Hamburg (U.S.). We thank Dietmar Pfeifer for helpful advice. We thank [Biorender.com](https://www.biorender.com). We thank Stella Maria Carro for her support and the provision of her laboratory facilities and equipment.

## AUTHOR CONTRIBUTIONS

D.H.H., D.D., and V.M.R. conceived the idea, designed the experiments, and composed the paper; V.M.R., P.W., J.Z., and K.J. conducted spatially resolved transcriptomics; P.W., J.K.B., U.K., S.P.B., N.N., J.v.E., M.B., and M.F. conducted scRNA-seq; H.S., S.K., and B.B. conducted IMC experiments; N.S. and A.K.W. conducted MALDI experiments; J.K. and D.H.H. conducted analysis and software design of SPATA; J.K. conducted analysis of scRNA-seq; D.H.H. and J.K. conducted data integration IMC and MALDI with spatial transcriptomics; J.M.G., M.F., F.S., L.V., and M.K. conducted further experiments and validations; R.S., M.S., and M.P. conducted neuropathological validation and diagnosis; M.B., U.G.H., O.S., J.B., C.F., and P.F. contributed to the interpretation of the results; O.S., J.B., C.F., and D.H.H. assisted in tissue sampling; V.M.R., L.V., K.J., and J.Z. conducted tissue culture experiments; F.L.R., U.S., and K.L. conducted cell-culture experiments and methylation experiments and analysis; and D.H.H. supervised the project.

## DECLARATION OF INTERESTS

The authors declare no competing interests.

Received: June 4, 2021

Revised: September 30, 2021

Accepted: May 13, 2022

Published: June 13, 2022

## REFERENCES

- Abuzneid, M., and Mahmood, A. (2017). Image Registration Based on a Minimized Cost Function and SURF Algorithm. In *Image Analysis and Recognition. ICIAR, vol 10317*, F. Karray, A. Campilho, and F. Cheriet, eds. (Springer, Cham.: Lecture Notes in Computer Science). [https://doi.org/10.1007/978-3-319-59876-5\\_36](https://doi.org/10.1007/978-3-319-59876-5_36).
- Aichler, M., Borgmann, D., Krumsiek, J., Buck, A., MacDonald, P.E., Fox, J.E.M., Lyon, J., Light, P.E., Keipert, S., Jastroch, M., et al. (2017). N-acetyltaurines and acylcarnitines cause an imbalance in insulin synthesis and secretion provoking  $\beta$  cell dysfunction in type 2 diabetes. *Cell Metab.* 25, 1334–1347. <https://doi.org/10.1016/j.cmet.2017.04.012>.
- Aryee, M.J., Jaffe, A.E., and Corrada, H. (2014). Minfi: a flexible and comprehensive Bioconductor package for the analysis of Infinium DNA methylation microarrays. *Bioinformatics* 30, 1363–1369.
- Bady, P., Sciuscio, D., Diserens, A.-C., Bloch, J., van den Bent, M.J., Marosi, C., Dietrich, P.-Y., Weller, M., Mariani, L., Heppner, F.L., et al. (2012). MGMT methylation analysis of glioblastoma on the Infinium methylation BeadChip identifies two distinct CpG regions associated with gene silencing and outcome, yielding a prediction model for comparisons across datasets, tumor grades, and CIMP-status. *Acta Neuropathol.* 124, 547–560. <https://doi.org/10.1007/s00401-012-1016-2>.
- Bay, H., Ess, A., Tuytelaars, T., and Van Gool, L. (2008). Speeded-up robust features (SURF). *Comput. Vis. Image Understand.* 110, 346–359.
- Bemis, K.D., Harry, A., Eberlin, L.S., Ferreira, C., van de Ven, S.M., Mallick, P., Stolzowicz, M., and Vitek, O. (2015). Cardinal: an R package for statistical analysis of mass spectrometry-based imaging experiments. *Bioinformatics* 31, 2418–2420. <https://doi.org/10.1093/bioinformatics/btv146>.
- Berg, S., Kutra, D., Kroeger, T., Straehle, C.N., Kausler, B.X., Haubold, C., Schiegg, M., Ales, J., Beier, T., Rudy, M., et al. (2019). ilastik: interactive machine learning for (bio)image analysis. *Nat. Methods* 16, 1226–1232. <https://doi.org/10.1038/s41592-019-0582-9>.
- Bergen, V., Lange, M., Peidli, S., Wolf, F.A., and Theis, F.J. (2020). Generalizing RNA velocity to transient cell states through dynamical modeling. *Nat. Biotechnol.* 38, 1408–1414. <https://doi.org/10.1038/s41587-020-0591-3>.
- Bhaduri, A., Di Lullo, E., Jung, D., Müller, S., Crouch, E.E., Espinosa, C.S., Ozawa, T., Alvarado, B., Spatazza, J., Cadwell, C.R., et al. (2020). Outer radial glia-like cancer stem cells contribute to heterogeneity of glioblastoma. *Cell Stem Cell* 26, 48–63. <https://doi.org/10.1016/j.stem.2019.11.015>.
- Bhandari, V., Hoey, C., Liu, L.Y., Lalonde, E., Ray, J., Livingstone, J., Lesurf, R., Shiah, Y.-J., Vujcic, T., Huang, X., et al. (2019). Molecular landmarks of tumor hypoxia across cancer types. *Nat. Genet.* 51, 308–318. <https://doi.org/10.1038/s41588-018-0318-2>.
- Bhandari, V., Li, C.H., Bristow, R.G., Boutros, P.C., and Consortium, P.C.A.W.G. (2020). Divergent mutational processes distinguish hypoxic and normoxic tumours. *Nat. Commun.* 11, 737. <https://doi.org/10.1038/s41467-019-14052-x>.
- Bivand, R.S., Pebesma, E., and Gomez-Rubio, V. (2013). *Applied spatial data analysis with R*, Second edition (NY: Springer). <https://asdar-book.org/>.
- Bowman, R.L., Wang, Q., Carro, A., Verhaak, R.G.W., and Squatrito, M. (2017). Gliovis data portal for visualization and analysis of brain tumor expression datasets. *Neuro Oncol.* 19, 139–141. <https://doi.org/10.1093/neuonc/now247>.
- Carpenter, A.E., Jones, T.R., Lamprecht, M.R., Clarke, C., Kang, I.H., Friman, O., Guertin, D.A., Chang, J.H., Lindquist, R.A., Moffat, J., et al. (2006). CellProfiler: image analysis software for identifying and quantifying cell phenotypes. *Genome Biol.* 7, R100. <https://doi.org/10.1186/gb-2006-7-10-r100>.

- Couturier, C.P., Ayyadury, S., Le, P.U., Nadaf, J., Monlong, J., Riva, G., Allache, R., Baig, S., Yan, X., Bourgey, M., et al. (2020). Single-cell RNA-seq reveals that glioblastoma recapitulates a normal neurodevelopmental hierarchy. *Nat. Commun.* 11, 3406. <https://doi.org/10.1038/s41467-020-17186-5>.
- Darmanis, S., Sloan, S.A., Croote, D., Mignardi, M., Chernikova, S., Samghabadi, P., Zhang, Y., Neff, N., Kowarsky, M., Caneda, C., et al. (2017). Single-cell RNA-seq analysis of infiltrating neoplastic cells at the migrating front of human glioblastoma. *Cell Rep.* 21, 1399–1410. <https://doi.org/10.1016/j.celrep.2017.10.030>.
- Darmanis, S., Sloan, S.A., Zhang, Y., Enge, M., Caneda, C., Shuer, L.M., Hayden Gephart, M.G., Barres, B.A., and Quake, S.R. (2015). A survey of human brain transcriptome diversity at the single cell level. *Proc. Natl. Acad. Sci. U S A.* 112, 7285–7290. <https://doi.org/10.1073/pnas.1507125112>.
- Elosua-Bayes, M., Nieto, P., Mereu, E., Gut, I., and Heyn, H. (2021). SPOTlight: seeded NMF regression to deconvolute spatial transcriptomics spots with single-cell transcriptomes. *Nucleic Acids Res.* 49, e50.
- Filley, A.C., Henriquez, M., and Dey, M. (2017). Recurrent glioma clinical trial, CheckMate-143: the game is not over yet. *Oncotarget* 8, 91779–91794. <https://doi.org/10.18632/oncotarget.21586>.
- Galili, T. (2015). dendextend: an R package for visualizing, adjusting and comparing trees of hierarchical clustering. *Bioinformatics* 31, 3718–3720. <https://doi.org/10.1093/bioinformatics/btv428>.
- Gangoso, E., Southgate, B., Bradley, L., Rus, S., Galvez-Cancino, F., McGivern, N., Güç, E., Kapourani, C.-A., Byron, A., Ferguson, K.M., et al. (2021). Glioblastomas acquire myeloid-affiliated transcriptional programs via epigenetic immunoeediting to elicit immune evasion. *Cell* 184, 2454–2470.e26. <https://doi.org/10.1016/j.cell.2021.03.023>.
- Garofano, L., Migliozi, S., Oh, Y.T., D'Angelo, F., Najac, R.D., Ko, A., Frangaj, B., Caruso, F.P., Yu, K., Yuan, J., et al. (2021). Pathway-based classification of glioblastoma uncovers a mitochondrial subtype with therapeutic vulnerabilities. *Nat. Cancer* 2, 141–156. <https://doi.org/10.1038/s43018-020-00159-4>.
- Gibb, S., and Strimmer, K. (2012). MALDIquant: a versatile R package for the analysis of mass spectrometry data. *Bioinformatics* 28, 2270–2271. <https://doi.org/10.1093/bioinformatics/bts447>.
- Gollini, I., Lu, B., Charlton, M., Brunsdon, C., and Harris, P. (2015). Gwmodel: an R package for exploring spatial heterogeneity using geographically weighted models. *J. Stat. Softw.* 63, 1–50.
- Grimes, D.R., Jansen, M., Macauley, R.J., Scott, J.G., and Basanta, D. (2020). Evidence for hypoxia increasing the tempo of evolution in glioblastoma. *Br. J. Cancer* 123, 1562–1569. <https://doi.org/10.1038/s41416-020-1021-5>.
- Grubman, A., Chew, G., Ouyang, J.F., Sun, G., Choo, X.Y., McLean, C., Simmons, R., Buckberry, S., Landin, D.V., Pflueger, J., et al. (2019). A single cell brain atlas in human Alzheimer's disease. Preprint at bioRxiv. <https://doi.org/10.1101/628347>.
- Habib, N., McCabe, C., Medina, S., Varshavsky, M., Kitsberg, D., Dvir-Szternfeld, R., Green, G., Dionne, D., Nguyen, L., Marshall, J.L., et al. (2020). Disease-associated astrocytes in Alzheimer's disease and aging. *Nat. Neurosci.* 23, 701–706. <https://doi.org/10.1038/s41593-020-0624-8>.
- Haghverdi, L., Lun, A.T.L., Morgan, M.D., and Marioni, J.C. (2018). Batch effects in single-cell RNA-sequencing data are corrected by matching mutual nearest neighbors. *Nat. Biotechnol.* 36, 421–427. <https://doi.org/10.1038/nbt.4091>.
- Hänzelmann, S., Castelo, R., and Guinney, J. (2013). GSEA: gene set variation analysis for microarray and RNA-seq data. *BMC Bioinf.* 14, 7. <https://doi.org/10.1186/1471-2105-14-7>.
- Hao, Y., Hao, S., Andersen-Nissen, E., Mauck, W.M., Zheng, S., Butler, A., Lee, M.J., Wilk, A.J., Darby, C., Zager, M., et al. (2021a). Integrated analysis of multimodal single-cell data. *Cell* 184, 3573–3587.e29. <https://doi.org/10.1016/j.cell.2021.04.048>.
- Hao, Y., Hao, S., Andersen-Nissen, E., Mauck, W.M., Zheng, S., Butler, A., Lee, M.J., Wilk, A.J., Darby, C., Zager, M., et al. (2021b). Integrated analysis of multimodal single-cell data. *Cell* 184, 3573–3587.e29. <https://doi.org/10.1016/j.cell.2021.04.048>.
- Hara, T., Chanoch-Myers, R., Mathewson, N.D., Myskiw, C., Atta, L., Bussema, L., Eichhorn, S.W., Greenwald, A.C., Kinker, G.S., Rodman, C., et al. (2021). Interactions between cancer cells and immune cells drive transitions to mesenchymal-like states in glioblastoma. *Cancer Cell* 39, 779–792.e11. <https://doi.org/10.1016/j.ccell.2021.05.002>.
- Heiland, D.H., Gaebelin, A., Bories, M., Wörner, J., Pompe, N., Franco, P., Heynckes, S., Bartholomae, M., hAilin, D.Ö., Carro, M.S., et al. (2018). Microenvironment-derived regulation of HIF signaling drives transcriptional heterogeneity in glioblastoma multiforme. *Mol. Cancer Res.* 16, 655–668. <https://doi.org/10.1158/1541-7786.MCR-17-0680>.
- Henrik Heiland, D., Ravi, V.M., Behringer, S.P., Frenking, J.H., Wurm, J., Joseph, K., Garrelfs, N.W.C., Strähle, J., Heynckes, S., Grauvogel, J., et al. (2019). Tumor-associated reactive astrocytes aid the evolution of immunosuppressive environment in glioblastoma. *Nat. Commun.* 10, 2541. <https://doi.org/10.1038/s41467-019-10493-6>.
- Hovestadt, V., and Zapatka, M. (2015). conumee: Enhanced copy-number variation analysis using Illumina DNA methylation arrays (R package version 1.9.0). <http://bioconductor.org/packages/conumee/>.
- Jing, A., Vizeacoumar, F.S., Parameswaran, S., Haave, B., Cunningham, C.E., Wu, Y., Arnold, R., Bonham, K., Freywald, A., Han, J., et al. (2018). Expression-based analyses indicate a central role for hypoxia in driving tumor plasticity through microenvironment remodeling and chromosomal instability. *NPJ Syst. Biol. Appl.* 4, 38. <https://doi.org/10.1038/s41540-018-0074-z>.
- Johnson, K.C., Anderson, K.J., Courtois, E.T., Gujar, A.D., Barthel, F.P., Varn, F.S., Luo, D., Seignon, M., Yi, E., Kim, H., et al. (2021). Single-cell multimodal glioma analyses identify epigenetic regulators of cellular plasticity and environmental stress response. *Nat. Genet.* 53, 1456–1468. <https://doi.org/10.1038/s41588-021-00926-8>.
- Joseph, J.V., Conroy, S., Pavlov, K., Sontakke, P., Tomar, T., Eggens-Meijer, E., Balasubramanian, V., Wagemakers, M., den Dunnen, W.F.A., and Kruij, F.A.E. (2015). Hypoxia enhances migration and invasion in glioblastoma by promoting a mesenchymal shift mediated by the HIF1 $\alpha$ -ZEB1 axis. *Cancer Lett.* 359, 107–116. <https://doi.org/10.1016/j.canlet.2015.01.010>.
- Kathagen, A., Schulte, A., Balcke, G., Phillips, H.S., Martens, T., Matschke, J., Günther, H.S., Soriano, R., Modrusan, Z., Sandmann, T., et al. (2013). Hypoxia and oxygenation induce a metabolic switch between pentose phosphate pathway and glycolysis in glioma stem-like cells. *Acta Neuropathol.* 126, 763–780. <https://doi.org/10.1007/s00401-013-1173-y>.
- Kleshchevnikov, V., Shmatko, A., Dann, E., Aivazidis, A., King, H.W., Li, T., Lomakin, A., Kedlian, V., Jain, M.S., Park, J.S., et al. (2020). Comprehensive mapping of tissue cell architecture via integrated single cell and spatial transcriptomics. Preprint at bioRxiv. <https://doi.org/10.1101/2020.11.15.378125>.
- Koch, S.E., and DesJardins, M. (1983). An interactive Barnes objective map analysis scheme for use with satellite and conventional data. *J. Applied Meteorol.* 22, 1487–1503.
- La Manno, G., Soldatov, R., Zeisel, A., Braun, E., Hochgerner, H., Petukhov, V., Lidschreiber, K., Kastrioti, M.E., Lönnerberg, P., Furlan, A., et al. (2018). RNA velocity of single cells. *Nature* 560, 494–498. <https://doi.org/10.1038/s41586-018-0414-6>.
- Lange, M., Bergen, V., Klein, M., Setty, M., Reuter, B., Bakhti, M., Lickert, H., Ansari, M., Schniering, J., Schiller, H.B., et al. (2020). CellRank for directed single-cell fate mapping. Preprint at bioRxiv. <https://doi.org/10.1101/2020.10.19.345983>.
- Li, W., Jia, H., Li, Q., Cui, J., Li, R., Zou, Z., and Hong, X. (2018). Glycerophosphatidylcholine PC(36:1) absence and 3'-phosphoadenylate (pAp) accumulation are hallmarks of the human glioma metabolome. *Sci. Rep.* 8, 14783. <https://doi.org/10.1038/s41598-018-32847-8>.
- Li, Y., Li, B., Li, W., Wang, Y., Akgül, S., Treisman, D.M., Heist, K.A., Pierce, B.R., Hoff, B., Ho, C.-Y., et al. (2020). Murine models of IDH-wild-type glioblastoma exhibit spatial segregation of tumor initiation and manifestation during evolution. *Nat. Commun.* 11, 3669. <https://doi.org/10.1038/s41467-020-17382-3>.
- Liddelow, S.A., and Barres, B.A. (2017). Reactive astrocytes: production, function, and therapeutic potential. *Immunity* 46, 957–967. <https://doi.org/10.1016/j.immuni.2017.06.006>.
- Liddelow, S.A., Guttenplan, K.A., Clarke, L.E., Bennett, F.C., Bohlen, C.J., Schirmer, L., Bennett, M.L., Münch, A.E., Chung, W.-S., Peterson, T.C.,



- p>et al. (2017). Neurotoxic reactive astrocytes are induced by activated microglia.
- Nature*
- 541, 481–487.
- <https://doi.org/10.1038/nature21029>
- .
- Lu, B., Harris, P., Charlton, M., and Brunsdon, C. (2014). The GWmodel R package: further topics for exploring spatial heterogeneity using geographically weighted models. *Geo Spatial Inf. Sci.* 17, 85–101.
- Lun, A.T.L., McCarthy, D.J., and Marioni, J.C. (2016). A step-by-step workflow for low-level analysis of single-cell RNA-seq data with Bioconductor. 5, 2122. <https://doi.org/10.12688/11000research.9501.2>.
- Luoto, K.R., Kumareswaran, R., and Bristow, R.G. (2013). Tumor hypoxia as a driving force in genetic instability. *Genome Integr.* 4, 5. <https://doi.org/10.1186/2041-9414-4-5>.
- Maier, J.P., Ravi, V.M., Kueckelhaus, J., Behringer, S.P., Garrelfs, N., Will, P., Sun, N., von Ehr, J., Goeldner, J.M., Pfeifer, D., et al. (2021). Inhibition of metabotropic glutamate receptor III facilitates sensitization to alkylating chemotherapeutics in glioblastoma. *Cell Death Dis.* 12, 723. <https://doi.org/10.1038/s41419-021-03937-9>.
- Maire, C.L., Fuh, M.M., Kaulich, K., Fita, K.D., Stevic, I., Heiland, D.H., Welsh, J.A., Jones, J.C., Görgens, A., Ricklefs, T., et al. (2021). Genome-wide methylation profiling of glioblastoma cell-derived extracellular vesicle DNA allows tumor classification. *Neuro Oncol.* 23, 1087–1099.
- Mathewson, N.D., Ashenberg, O., Tirosh, I., Gritsch, S., Perez, E.M., Marx, S., Jerby-Aron, L., Chanoch-Myers, R., Hara, T., Richman, A.R., et al. (2021). Inhibitory CD161 receptor identified in glioma-infiltrating T cells by single-cell analysis. *Cell* 184, 1281–1298.e26. <https://doi.org/10.1016/j.cell.2021.01.022>.
- Monzon, F.A., Alvarez, K., Peterson, L., Truong, L., Amato, R.J., Hernandez-McClain, J., Tannir, N., Parwani, A.V., and Jonasch, E. (2011). Chromosome 14q loss defines a molecular subtype of clear-cell renal cell carcinoma associated with poor prognosis. *Mod. Pathol.* 24, 1470–1479. <https://doi.org/10.1038/modpathol.2011.107>.
- Neftel, C., Laffy, J., Filbin, M.G., Hara, T., Shore, M.E., Rahme, G.J., Richman, A.R., Silverbush, D., Shaw, M.L., Hebert, C.M., et al. (2019). An integrative model of cellular states, plasticity, and genetics for glioblastoma. *Cell* 178, 835–849.e21. <https://doi.org/10.1016/j.cell.2019.06.024>.
- Osswald, M., Jung, E., Sahm, F., Solecki, G., Venkataramani, V., Blaes, J., Weil, S., Horstmann, H., Wiestler, B., Syed, M., et al. (2015). Brain tumour cells interconnect to a functional and resistant network. *Nature* 528, 93–98. <https://doi.org/10.1038/nature16071>.
- Palmer, A., Phapale, P., Chernyavsky, I., Lavigne, R., Fay, D., Tarasov, A., Kovalev, V., Fuchser, J., Nikolenko, S., Pineau, C., et al. (2017). FDR-controlled metabolite annotation for high-resolution imaging mass spectrometry. *Nat. Methods* 14, 57–60. <https://doi.org/10.1038/nmeth.4072>.
- Patel, A.P., Tirosh, I., Trombetta, J.J., Shalek, A.K., Gillespie, S.M., Wakimoto, H., Cahill, D.P., Nahed, B.V., Curry, W.T., Martuza, R.L., et al. (2014). Single-cell RNA-seq highlights intratumoral heterogeneity in primary glioblastoma. *Science* 344, 1396–1401. <https://doi.org/10.1126/science.1254257>.
- Phillips, H.S., Kharbanda, S., Chen, R., Forrest, W.F., Soriano, R.H., Wu, T.D., Misra, A., Nigro, J.M., Colman, H., Soroceanu, L., et al. (2006). Molecular subclasses of high-grade glioma predict prognosis, delineate a pattern of disease progression, and resemble stages in neurogenesis. *Cancer Cell* 9, 157–173. <https://doi.org/10.1016/j.ccr.2006.02.019>.
- Pombo Antunes, A.R., Scheyltjens, I., Lodi, F., Messiaen, J., Antoranz, A., Duerinck, J., Kancheva, D., Martens, L., De Vlaminc, K., and Van Hove, H. (2021). Single-cell profiling of myeloid cells in glioblastoma across species and disease stage reveals macrophage competition and specialization. *Nat. Neurosci.* 24, 595–610. <https://doi.org/10.1038/s41593-020-00789-y>.
- Ravi, V.M., Joseph, K., Wurm, J., Behringer, S., Garrelfs, N., d'Errico, P., Naseri, Y., Franco, P., Meyer-Luehmann, M., Sankowski, R., et al. (2019). Human organotypic brain slice culture: a novel framework for environmental research in neuro-oncology. *Life Sci. Alliance* 2, e201900305. <https://doi.org/10.26508/lsa.201900305>.
- Ravi, V.M., Neidert, N., Will, P., Joseph, K., Maier, J.P., Kueckelhaus, J., Vollmer, L., Goeldner, J.M., Behringer, S.P., Scherer, F., et al. (2022). T-cell dysfunction in the glioblastoma microenvironment is mediated by myeloid cells releasing interleukin-10. *Nat. Commun.* 13, 925. <https://doi.org/10.1038/s41467-022-28523-1>.
- Reuter, B., Weber, M., Fackeldey, K., Röblitz, S., and Garcia, M.E. (2018). Generalized Markov state modeling method for nonequilibrium biomolecular dynamics: exemplified on amyloid  $\beta$  conformational dynamics driven by an oscillating electric field. *J. Chem. Theory Comput.* 14, 3579–3594. <https://doi.org/10.1021/acs.jctc.8b00079>.
- Richards, L.M., Whitley, O.K.N., MacLeod, G., Cavalli, F.M.G., Coutinho, F.J., Jaramillo, J.E., Svergun, N., Riverin, M., Croucher, D.C., Kushida, M., et al. (2021). Gradient of Developmental and Injury Response transcriptional states defines functional vulnerabilities underpinning glioblastoma heterogeneity. *Nat. Cancer* 2, 157–173. <https://doi.org/10.1038/s43018-020-00154-9>.
- Rooj, A.K., Ricklefs, F., Mineo, M., Nakano, I., Chiocca, E.A., Bronisz, A., and Godlewski, J. (2017). MicroRNA-mediated dynamic bidirectional shift between the subclasses of glioblastoma stem-like cells. *Cell Rep.* 19, 2026–2032. <https://doi.org/10.1016/j.celrep.2017.05.040>.
- Sankowski, R., Böttcher, C., Masuda, T., Geirsdottir, L., Sagar, Sindram, E., Seredenina, T., Muhs, A., Scheiwe, C., Shah, M.J., Heiland, D.H., et al. (2019). Mapping microglia states in the human brain through the integration of high-dimensional techniques. *Nat. Neurosci.* 22, 2098–2110. <https://doi.org/10.1038/s41593-019-0532-y>.
- Schneider, M., Vollmer, L., Potthoff, A.-L., Ravi, V.M., Evert, B.O., Rahman, M.A., Sarowar, S., Kueckelhaus, J., Will, P., Zuhorst, D., et al. (2021). Meclofenamate causes loss of cellular tethering and decoupling of functional networks in glioblastoma. *Neuro Oncol.* 23, 1885–1897. <https://doi.org/10.1093/neuonc/noab092>.
- Seim, J., Graff, P., Åmellem, Ø., and Landsverk, K.S. (2003). Hypoxia-induced irreversible S-phase arrest involves down-regulation of cyclin A. *Cell Prolif* 36, 321–332.
- Senatorov, V.V., Friedman, A.R., Milikovsky, D.Z., Ofer, J., Saar-Ashkenazy, R., Charbakh, A., Jahan, N., Chin, G., Mihaly, E., Lin, J.M., et al. (2019). Blood-brain barrier dysfunction in aging induces hyperactivation of TGF $\beta$  signaling and chronic yet reversible neural dysfunction. *Sci. Transl. Med.* 11, eaaw8283. <https://doi.org/10.1126/scitranslmed.aaw8283>.
- Sharma, S.V., Lee, D.Y., Li, B., Quinlan, M.P., Takahashi, F., Maheswaran, S., McDermott, U., Azizian, N., Zou, L., Fischbach, M.A., et al. (2010). A chromatin-mediated reversible drug-tolerant state in cancer cell subpopulations. *Cell* 141, 69–80. <https://doi.org/10.1016/j.cell.2010.02.027>.
- Shim, E.-H., Livi, C.B., Rakheja, D., Tan, J., Benson, D., Parekh, V., Kho, E.-Y., Ghosh, A.P., Kirkman, R., Velu, S., et al. (2014). L-2-Hydroxyglutarate: an epigenetic modifier and putative oncometabolite in renal cancer. *Cancer Discov.* 4, 1290–1298. <https://doi.org/10.1158/2159-8290.CD-13-0696>.
- Sieber, O.M., Heinemann, K., and Tomlinson, I.P.M. (2003). Genomic instability—the engine of tumorigenesis? *Nat. Rev. Cancer* 3, 701–708. <https://doi.org/10.1038/nrc1170>.
- Smith, J.C., and Sheltzer, J.M. (2018). Systematic identification of mutations and copy number alterations associated with cancer patient prognosis. *Elife* 7, e39217. <https://doi.org/10.7554/eLife.39217>.
- Sun, N., Fernandez, I.E., Wei, M., Witting, M., Aichler, M., Feuchtinger, A., Burgstaller, G., Verleden, S.E., Schmitt-Kopplin, P., Eickelberg, O., and Walch, A. (2018). Pharmacometabolic response to pirfenidone in pulmonary fibrosis detected by MALDI-FTICR-MSI. *Eur. Respir. J.* 52, 1702314. <https://doi.org/10.1183/13993003.02314-2017>.
- Tabula Muris Consortium (2020). A single-cell transcriptomic atlas characterizes ageing tissues in the mouse. *Nature* 583, 590–595. <https://doi.org/10.1038/s41586-020-2496-1>.
- Tirosh, I., Izar, B., Prakadan, S.M., Wadsworth, M.H., Treacy, D., Trombetta, J.J., Rotem, A., Rodman, C., Lian, C., Murphy, G., et al. (2016b). Dissecting the multicellular ecosystem of metastatic melanoma by single-cell RNA-seq. *Science* 352, 189–196. <https://doi.org/10.1126/science.1254050>.
- Tirosh, I., Venteicher, A.S., Hebert, C., Escalante, L.E., Patel, A.P., Yizhak, K., Fisher, J.M., Rodman, C., Mount, C., Filbin, M.G., et al. (2016a). Single-cell RNA-seq supports a developmental hierarchy in human oligodendrogloma. *Nature* 539, 309–313. <https://doi.org/10.1038/nature20123>.

- Tiwari, A., Tashiro, K., Dixit, A., Soni, A., Vogel, K., Hall, B., Shafqat, I., Slaughter, J., Param, N., Le, A., et al. (2020). Loss of HIF1A from pancreatic cancer cells increases expression of PPP1R1B and degradation of p53 to promote invasion and metastasis. *Gastroenterology* 159, 1882–1897. <https://doi.org/10.1053/j.gastro.2020.07.046>.
- Townes, F.W., Hicks, S.C., Aryee, M.J., and Irizarry, R.A. (2019). Feature selection and dimension reduction for single-cell RNA-Seq based on a multinomial model. *Genome Biol.* 20, 295. <https://doi.org/10.1186/s13059-019-1861-6>.
- Venkataramani, V., Tanev, D.I., Strahle, C., Studier-Fischer, A., Fankhauser, L., Kessler, T., Körber, C., Kardorff, M., Ratliff, M., Xie, R., et al. (2019). Glutamatergic synaptic input to glioma cells drives brain tumour progression. *Nature* 573, 532–538. <https://doi.org/10.1038/s41586-019-1564-x>.
- Venkatesh, H.S., Morishita, W., Geraghty, A.C., Silverbush, D., Gillespie, S.M., Arzt, M., Tam, L.T., Espenel, C., Ponnuswami, A., Ni, L., et al. (2019). Electrical and synaptic integration of glioma into neural circuits. *Nature* 573, 539–545. <https://doi.org/10.1038/s41586-019-1563-y>.
- Venteicher, A.S., Tirosh, I., Hebert, C., Yizhak, K., Neftel, C., Filbin, M.G., Hovestadt, V., Escalante, L.E., Shaw, M.L., Rodman, C., et al. (2017). Decoupling genetics, lineages, and microenvironment in IDH-mutant gliomas by single-cell RNA-seq. *Science* 355, eaai8478. <https://doi.org/10.1126/science.aai8478>.
- Verhaak, R.G.W., Hoadley, K.A., Purdom, E., Wang, V., Qi, Y., Wilkerson, M.D., Miller, C.R., Ding, L., Golub, T., Mesirov, J.P., et al. (2010). Integrated genomic analysis identifies clinically relevant subtypes of glioblastoma characterized by abnormalities in PDGFRA, IDH1, EGFR, and NF1. *Cancer Cell* 17, 98–110. <https://doi.org/10.1016/j.ccr.2009.12.020>.
- Wishart, D.S., Feunang, Y.D., Marcu, A., Guo, A.C., Liang, K., Vázquez-Fresno, R., Sajed, T., Johnson, D., Li, C., Karu, N., et al. (2018). HMDB 4.0: the human metabolome database for 2018. *Nucleic Acids Res.* 46, D608–D617. <https://doi.org/10.1093/nar/gkx1089>.
- Wurm, J., Behringer, S.P., Ravi, V.M., Joseph, K., Neidert, N., Maier, J.P., Doria-Medina, R., Folio, M., Delev, D., Pfeifer, D., et al. (2019). Astroglial release of pro-oncogenic chitinase 3-like 1 causing MAPK signaling in glioblastoma. *Cancers* 11, 1437.
- Yu, G., Wang, L.-G., Han, Y., and He, Q.-Y. (2012). clusterProfiler: an R package for comparing biological themes among gene clusters. *OMICS* 16, 284–287. <https://doi.org/10.1089/omi.2011.0118>.
- Yun, S.P., Kam, T.-I., Panicker, N., Kim, S., Oh, Y., Park, J.-S., Kwon, S.-H., Park, Y.J., Karuppagounder, S.S., Park, H., et al. (2018). Block of A1 astrocyte conversion by microglia is neuroprotective in models of Parkinson's disease. *Nat. Med.* 24, 931–938. <https://doi.org/10.1038/s41591-018-0051-5>.
- Zanotelli, V.R.T., and Bodenmiller, B. (2022). ImcSegmentationPipeline: A pixel-classification based multiplexed image segmentation pipeline. <https://doi.org/10.5281/zenodo.384196>.
- Zappia, L., and Oshlack, A. (2018). Clustering trees: a visualization for evaluating clusterings at multiple resolutions. *GigaScience* 7, giy083. <https://doi.org/10.1093/gigascience/giy083>.
- Zhao, T., Chiang, Z.D., Morriss, J.W., LaFave, L.M., Murray, E.M., Del Priore, I., Meli, K., Lareau, C.A., Nadaf, N.M., Li, J., et al. (2022). Spatial genomics enables multi-modal study of clonal heterogeneity in tissues. *Nature* 601, 85–91. <https://doi.org/10.1038/s41586-021-04217-4>.
- Zheng, G.X.Y., Terry, J.M., Belgrader, P., Ryvkin, P., Bent, Z.W., Wilson, R., Ziraldo, S.B., Wheeler, T.D., McDermott, G.P., Zhu, J., et al. (2017). Massively parallel digital transcriptional profiling of single cells. *Nat. Commun.* 8, 14049. <https://doi.org/10.1038/ncomms14049>.
- Zhu, J., Tsai, H.-J., Gordon, M.R., and Li, R. (2018). Cellular stress associated with aneuploidy. *Dev. Cell* 44, 420–431. <https://doi.org/10.1016/j.devcel.2018.02.002>.

## STAR★METHODS

### KEY RESOURCES TABLE

REAGENT or RESOURCE	SOURCE	IDENTIFIER
<b>Antibodies</b>		
Imaging mass cytometry antibody panel		See <a href="#">Table S4</a>
<b>Chemicals, peptides, and recombinant proteins</b>		
Tissue-Tek® O.C.T.™ Compound	Sakura	Cat#4583
TriZOI	Invitrogen	Cat#15596026
SPRIselect reagent	Beckman Coulter	Cat#B23318
Bovine Serum Albumin (BSA)	Sigma-Aldrich	Cat#A3059
9-aminoacridine hydrochloride monohydrate (9-AA)	Sigma-Aldrich	Cat#A38401
4',6-diamidino-2-phenylindole (DAPI)	Merck KGaA	Cat#32670-5MG
89-Yttrium (III) nitrate tetrahydrate	Sigma-Aldrich	Cat#217239-10G
157-Gadolinium (III) chloride	Trace Sciences Int.	
Super Block (TBS) Blocking Buffer	ThermoFisher Scientific	Cat#37581
Iridium Cell-ID intercalator	Fluidigm	Cat#201192B
GlutaMax™	Gibco	Cat#13462629
Hibernate™ -A Medium	Gibco	Cat#12087586
N-methyl-D-Glucamin (NMDG)	Sigma-Aldrich	Cat#M2004
Antibiotic-Antimycotic (100X)	Gibco	Cat#15240062
Neurobasal™ Medium	Gibco	Cat#11570556
L-Glutamine	Gibco	Cat# 25030149
B-27 Supplement, serum-free (50X)	Gibco	Cat#11530536
MgSO4	Sigma-Aldrich	Cat#M3409
HEPES	Sigma-Aldrich	Cat#H0887
D-Glucose	Sigma-Aldrich	Cat#RNBG7039
<b>Critical commercial assays</b>		
Visium Spatial Tissue Optimization Slide & Reagent Kit	10x Genomics	Cat#PN-1000193
Visium Spatial Gene Expression Slide and Reagent Kit	10x Genomics	Cat#PN-1000184
Visium Accessory Kit	10x Genomics	Cat#PN-1000194
KAPA SYBR FAST qPCR Master Mix	Roche	Cat#KK4600
Dual Index Kit TT Set A	10x Genomics	Cat#PN-1000215
Chromium Next GEM Single Cell 3' GEM, Library & Gel Bead Kit v3.1	10x Genomics	Cat#PN-1000121
Chromium Next GEM Chip G Single Cell Kit	10x Genomics	Cat#PN-1000120
Single Index Kit T Set A	10x Genomics	Cat#PN-1000213
Pico Pure RNA Isolation Kit	ThermoFisher Scientific	Cat#KIT0204
Fragment Analyzer 5200 RNA Kit	Agilent	Cat#DNF-471
Fragment Analyzer 5200 HS NGS Kit	Agilent	Cat#DNF-474
Qubit 1X dsDNA HS Kit	ThermoFisher Scientific	Cat#Q33231
NextSeq 500/550 High Output Kit v2.5 (150 cycles)	Illumina	Cat#20024907
NextSeq 500/550 High Output kit v2.5 (75 cycles)	Illumina	Cat#20024906
Neural Tissue Dissociation Kit (T)	Miltenyi Biotech	Cat#130-093-231

(Continued on next page)

**Continued**

REAGENT or RESOURCE	SOURCE	IDENTIFIER
Maxpar X8 antibody labelling Kits	Fluidigm	Cat#201149A
Biological samples		
BTSC#233	UK Freiburg	Primary Cell Line
BTSC#168	UK Freiburg	Primary Cell Line
GS10	UKE Hamburg	Primary Cell Line
GS11	UKE Hamburg	Primary Cell Line
GS12	UKE Hamburg	Primary Cell Line
GS13	UKE Hamburg	Primary Cell Line
Human Cortex Donor 1	UK Freiburg	N/A
Human Cortex Donor 2	UK Freiburg	N/A
Human Cortex Donor 3	UK Freiburg	N/A
Rat Cortex 3 weeks old	Charles River	Wistar (003)
Rat Cortex 2 Years old	Charles River	Wistar (003)
Deposited data		
Spatial Transcriptomic Data (raw)	Datadryad	<a href="https://doi.org/10.5061/dryad.h70rxwdmj">https://doi.org/10.5061/dryad.h70rxwdmj</a>
Spatial Transcriptomic Data (processed)	SPATADData (GitHub)	<a href="https://github.com/theMIOlab/SPATADData">https://github.com/theMIOlab/SPATADData</a>
MALDI Data (raw and processed)	Datadryad	<a href="https://doi.org/10.5061/dryad.h70rxwdmj">https://doi.org/10.5061/dryad.h70rxwdmj</a>
IMC Data (raw and processed)	Datadryad	<a href="https://doi.org/10.5061/dryad.h70rxwdmj">https://doi.org/10.5061/dryad.h70rxwdmj</a>
850k Methylation EPIC Data:	Datadryad	<a href="https://doi.org/10.5061/dryad.h70rxwdmj">https://doi.org/10.5061/dryad.h70rxwdmj</a>
TCGA data	GLIOVIS	<a href="http://gliovis.bioinfo.cnio.es">http://gliovis.bioinfo.cnio.es</a>
Single Cell Data (Neftel et al., 2019)	GEO	GSE131928
Single Cell Data (Darmanis et al., 2017)	GEO	GSE84465
Single Cell Data (Ravi et al., 2022)	OSF database	<a href="https://osf.io/4q32e/">https://osf.io/4q32e/</a> <a href="https://doi.org/10.17605/OSF.IO/4Q32E">https://doi.org/10.17605/OSF.IO/4Q32E</a>
Single Cell Data (Pombo Antunes et al., 2021)	GEO	GSE163120
Single Cell Data (Mathewson et al., 2021)	GEO	GSE163108
Software and algorithms		
SPATA	<a href="https://github.com/theMIOlab/SPATA">https://github.com/theMIOlab/SPATA</a>	
SPATA2	<a href="https://github.com/theMIOlab/SPATA2">https://github.com/theMIOlab/SPATA2</a>	
Cell Profiler	<a href="https://cellprofiler.org">https://cellprofiler.org</a>	
Ilastik	<a href="https://www.ilastik.org">https://www.ilastik.org</a>	
For MALDI: R-Script:	<a href="https://github.com/theMIOlab/Code_Request/blob/main/MALDI.R">https://github.com/theMIOlab/Code_Request/blob/main/MALDI.R</a>	
SPATAWrapper	<a href="https://github.com/heilandd/SPATAWrappers">https://github.com/heilandd/SPATAWrappers</a>	
METASPACE,	<a href="https://metaspace2020.eu">https://metaspace2020.eu</a>	
Human Metabolome Database	<a href="https://www.hmdb.ca">https://www.hmdb.ca</a>	
MSigDBv7.2	<a href="https://www.gsea-msigdb.org/gsea/msigdb/index.jsp">https://www.gsea-msigdb.org/gsea/msigdb/index.jsp</a>	
Bodenmiller Pipeline for Segmentation	<a href="https://github.com/Bodenmiller-Group/ImcSegmentationPipeline">https://github.com/Bodenmiller-Group/ImcSegmentationPipeline</a>	
Other		
Indium-tin-oxide coated conductive slides	Bruker Daltonics	Cat#MFPRM7462243
C-Tubes	Miltenyi Biotech	Cat#130-093-237
SuperFrost plus slides	R. Langenbrinck GmbH	Cat#03-0060
PAP pen	ImmEdge	Cat#H-4000

**RESOURCE AVAILABILITY**

**Lead contact**

Further information and requests for resources and reagents should be directed and will be fulfilled by the Contact: D. H. Heiland, [dieter.henrik.heiland@uniklinik-freiburg.de](mailto:dieter.henrik.heiland@uniklinik-freiburg.de).



### Materials availability

This study did not generate new unique reagents.

### Data and code availability

All data including spatial transcriptomic data, MALDI data, IMC data, single-cell RNA-seq and 850k methylation that were generated in this study have been deposited at Datadryad (<https://doi.org/10.5061/dryad.h70rxwdmj>) and are publicly available. Accession links and DOI's are listed in the [key resources table](#). For validation analysis were performed from publicly deposited data. Single cell RNA-seq data from GEO (GSE131928, GSE84465, GSE163120, GSE163108) and OSF (<https://osf.io/4q32e/> <https://doi.org/10.17605/OSF.IO/4Q32E>) was used. All original code has been deposited at GitHub and is publicly available as of the date of publication. The software tool SPATA and SPATA2 (<https://github.com/theMILOLab/SPATA2>) was generated for this study. Links of all used tools are listed in the [key resources table](#)

## EXPERIMENTAL MODEL AND SUBJECT DETAILS

### Patient samples

The local ethics committee of the University of Freiburg approved the data evaluation, imaging procedures and experimental design (protocol 100020/09 and 472/15\_160880). The methods were carried out in accordance with the approved guidelines, with written informed consent obtained from all subjects. Patients at the Department of Neurosurgery of the Medical Center, University of Freiburg (Freiburg, Germany) provided preoperative informed consent to take part in the study in all cases. Clinical characteristics are summarized in [Table S1](#). If the anatomical location and constitution of the access cortex facilitated its utilization at the time of surgery, spatial transcriptomics and tissue culture experiments were performed on the tumor and the (healthy) access cortex.

### Cell lines

Patient derived primary cultures (BTSC#233 [gender: male] and BTSC#168 [gender: female]) were grown in MEM (GIBCO, 11095080) supplemented with 10% FCS (Pan-Biotech, P30-3306) and 1% Penicillin/Streptomycin (Pan-Biotech, P0607100).

### Rat tissue samples

All protocols were approved by the responsible Animal Care Committee of the Regierungspräsidium Freiburg (Permit X21/02A), Male Wistar rats (3 weeks old and 24 months old, Charles River), were housed under standard lighting (12 h light-dark cycle), at 22°C and 40% humidity and were allowed access to food and water *ad libitum*. On the experimental day, rats were decapitated after an overdose of inhalation anesthetic (Forene, Baxter, USA), and the brains were quickly extracted and submerged in oxygenated ice-cold "Preparation medium". Tissue sections (300µm) were prepared using a vibratome (VT 1200, Leica, Germany) as previously described and were processed similarly to the human tissue sections ([Ravi et al., 2019](#)).

## METHOD DETAILS

### Spatial transcriptomics

Spatial transcriptomics experiments were performed using the 10X Visium Spatial Gene Expression kit (<https://www.10xgenomics.com/spatial-gene-expression>). All the instructions for Tissue Optimization and Library preparation were followed according to manufacturer's protocol. Here, we briefly describe the methods followed using the library preparation protocol.

### Tissue collection and RNA quality control

Fresh tissue, collected immediately post resection, was quickly embedded in Tissue-Tek® O.C.T.™ Compound (Sakura, 4583) and snap frozen in isopentane, pre-chilled in liquid nitrogen. Embedded tissue was stored at –80°C until further processing. A total of 10 sections (10µm each) per sample were lysed using TriZOI (Invitrogen, 15596026) and used to determine RNA integrity. Total RNA was extracted using PicoPure RNA Isolation Kit (Thermo Fisher, KIT0204) according to the manufacturer's protocol. RIN values were determined using a Fragment Analyzer 5200 (RNA kit, Agilent, DNF-471) according to the manufacturer's protocol. Only samples with an RNA integrity value > 7 was used.

### Spatial gene expression protocol

10 µm thick sections were mounted onto spatially barcoded glass slides with poly-T reverse transcription primers, one section per array. Slides were fixed in 100% methanol and H&E staining was performed. Brightfield imaging was carried out at 10× magnification with a Zeiss Axio Imager 2 Microscope, and post-processing was performed using ImageJ software. Following imaging, permeabilization was carried out for a pre-determined time to release and capture mRNA from the tissue onto primers on the slide. Template switch oligos were introduced in order to generate a second strand in a reverse transcription reaction and produced second strand was cleaved off by denaturation. Next, generated cDNA was amplified according to qPCR results using KAPA SYBR FAST qPCR Master Mix (Roche, KK4600) and fragments in the size of interest were selected using SPRIselect reagent (Beckman Coulter, B23318). Quality check was performed using a Fragment Analyzer (HS NGS Fragment kit, Agilent, DNF-474). Further, fragmentation and double-sided size selection using SPRIselect reagent was carried out in order to optimize cDNA fragments for Illumina NextSeq

Sequencing System. Unique indexes as well as P5 and P7 Illumina primers were added to the libraries. The average length of the final libraries was quantified using a Fragment Analyzer (HS NGS Fragment kit, Agilent, DNF-474) and the concentration of libraries was determined using a Qubit 1X dsDNA HS kit (Thermo Fisher, Q33231). Final libraries were diluted to 4nM, pooled, and denatured before sequencing on the Illumina NextSeq 550 platform using paired-end sequencing. We used 28 cycles for read 1, 10 cycles per index and 120 cycles for read 2 on a NextSeq 500/550 High Output Kit v2.5 (Illumina, 20024907).

### **MALDI-FTICR-MSI**

Tissue preparation steps for MALDI imaging mass spectrometry (MALDI-MSI) analysis was performed as previously described (Aichler et al., 2017; Sun et al., 2018). Frozen tissues were cryo-sectioned at 10  $\mu$ m from the same tissue block as used for spatial transcriptomics and thaw mounted onto indium-tin-oxide coated conductive slides (Bruker Daltonik, Bremen, Germany). The matrix solution consisted of 10 mg/mL 9-aminoacridine hydrochloride monohydrate (9-AA) (Sigma-Aldrich, Germany) in water/methanol 30:70 (v/v). SunCollect™ automatic sprayer (Sunchrom, Friedrichsdorf, Germany) was used for matrix application. The MALDI-MSI measurement was performed on a Bruker Solarix 7T FT-ICR-MS (Bruker Daltonik, Bremen, Germany) in negative ion mode using 100 laser shots at a frequency of 1,000 Hz. The MALDI-MSI data were acquired over a mass range of m/z 75–1,000 with 50  $\mu$ m lateral resolution. Following the MALDI imaging experiments, the tissue sections were stained with hematoxylin and eosin (H&E) and scanned with an AxioScan.Z1 digital slide scanner (Zeiss, Jena, Germany) equipped with a 20 $\times$  magnification objective. After the MALDI-MSI measurement, the acquired data underwent spectra processing in FlexImaging v. 5.0 (Bruker Daltonics, Germany) and SCiLS Lab v. 2020 (Bruker Daltonik GmbH). MS peak annotation was performed using Human Metabolome Database (HMDB, <https://www.hmdb.ca/>) (Wishart et al., 2018) and METASPACE (<https://metaspace2020.eu/>) (Palmer et al., 2017).

### **Human organotypic slice culture**

Human neocortical slices were prepared as recently described (Henrik Heiland et al., 2019; Ravi et al., 2019). Resected cortical tissue (assessed by EEG and MRI) was immediately brought to the lab in the “Preparation medium” (Gibco Hibernat<sup>TM</sup> media supplemented with 1 mM Gibco GlutaMax<sup>TM</sup>, 13 mM Glucose, 30 mM NMDG and 1% Anti-Anti) saturated with carbogen (95% O<sub>2</sub> and 5% CO<sub>2</sub>). Capillaries and damaged tissue were dissected away from the tissue block. The combination of GlutaMax and NMDG in the collection medium has provided us with best tissue recovery post resection. 300  $\mu$ m thick cortical slices were obtained using a vibratome (VT1200, Leica Germany) and incubated in preparation medium for 10 min before plating to avoid any variability due to tissue trauma. Tissue blocks (1  $\times$  2 cm) typically permits preparation of 18–20 sections. One to three sections were gathered per insert, with care to maintain adequate spacing between the sections. The transfer of the slices was facilitated by a polished wide mouth glass pipette. Slice were maintained in growth medium containing Neurobasal L-Glutamine (Lot No. 1984948; Gibco) supplemented with 2% serum-free B-27 (Lot No. 175040001; Gibco), 2% Anti-Anti (Lot No. 15240-062; Gibco), 13 mM d-glucose (Lot No. RNBG7039; Sigma-Aldrich), 1 mM MgSO<sub>4</sub> (M3409; Sigma-Aldrich), 15 mM HEPES (H0887; Sigma-Aldrich), and 2 mM GlutaMAX (Lot No. 1978435; Gibco). The entire medium was replaced with fresh medium 24 h post plating and every 48 h thereafter.

### **Human ex-vivo glioblastoma model**

ZsGreen tagged BTSC#233 was cultured and prepared as described previously (Henrik Heiland et al., 2019; Schneider et al., 2021). Briefly, post trypsinization, a centrifugation step was performed, following which the cells were harvested and re-suspended in PBS for 20,000 cells/ $\mu$ L. Cells were then used immediately for inoculation into tissue sections. A 10  $\mu$ L Hamilton syringe was used to inject 1  $\mu$ L of GBM cells onto the white matter part of the section. Inoculated tissue sections cells were incubated at 37°C for a week and culture medium was refreshed every 48h. Tumor proliferation was monitored by fluorescence imaging by means of an inverted microscope (Observer D.1; Zeiss). After the appropriate culture duration, sections were either fixed and used for immunostaining or for single cell sequencing.

### **Single cell suspension from cultured slices**

Nine sections per condition were processed using C-Tubes (Miltenyi Biotech, 130-093-237) with a shortened protocol for the Neural Tissue Dissociation Kit (T) (Miltenyi Biotech, 130-093-231). Briefly, the tissue as well as the first enzyme mix, containing enzyme T and buffer X, were transferred to a C-tube, and incubated at 37°C for 5 min, followed by a dissociation for 2 min. Next, second enzyme mix, containing enzyme A and buffer Y, was added, and incubated for 5 min, followed by another dissociation for 2 min. The final sample was then filtered and centrifuged in a 50mL falcon and cell pellet was further used for cell sorting.

### **Cell sorting for scRNA-seq**

Freshly prepared cell suspensions were washed with FACS buffer containing 2% FCS and 1mM EDTA in PBS and stained with DAPI. Cells were sorted on the BD FACSAria<sup>TM</sup> Fusion flow cytometer at the core facility, University of Freiburg. To gather viable tumor cells, ZsGreen positive, DAPI negative populations were collected in BSA-coated tubes containing 2% FCS in PBS and prepared for later droplet-based single cell RNA-Sequencing.

### **Single cell RNA-sequencing**

Single cell RNA-sequencing was performed according to the Chromium Next GEM Single Cell 3'v3.1 protocol (10x Genomics), based on a droplet scRNA-sequencing approach. In brief, collected cells were added to a prepared master mix containing reagents for a

reverse transcription reaction and loaded onto separate lanes of a Chromium Next GEM Chip G. After running the chip on a Chromium Controller, generated GEMs were transferred to a tube strip. Following reverse transcription, GEMs were broken, and cDNA was purified from leftover reagents. Amplified cDNA was fragmented and size-selected using SPRIselect reagent (Beckman Coulter, B23318). i7 indexes as well as P5 and P7 Illumina primers were added to the libraries. The average length of final libraries was quantified using a Fragment Analyzer (HS NGS Fragment kit, Agilent, DNF-474) and the concentration of libraries was determined using a Qubit 1X dsDNA HS kit (Thermo Fisher, Q33231). Final libraries were diluted to 4nM, pooled, and denatured before sequencing on an Illumina NextSeq 550 Sequencing System (Illumina, San Diego, CA, USA) using NextSeq 500/550 High Output kit v2.5 (Illumina, 20024906) with 28 cycles for read 1, 8 cycles for i7 index and 56 cycles for read 2.

### Imaging mass cytometry antibody panel

A 39-marker IHC panel (Table S4) was designed including structural and tumor markers as well as markers to assess several innate and adaptive immune cells (Table S4). Metal-labeled antibodies were either obtained pre-conjugated (Fluidigm) or labeled in-house by conjugating purified antibodies to lanthanide metals using the Maxpar X8 antibody labelling kit (Fluidigm) according to the manufacturer's instructions. In addition, 89-Yttrium (III) nitrate tetrahydrate (Sigma Aldrich, cat. # 217239-10G) and 157-Gadolinium (III) chloride (Trace Sciences Int.) were diluted in L-buffer to a 1M stock solution and further diluted to a 50  $\mu$ M working solution for subsequent antibody labelling with the Maxpar X8 labelling kit. Metal-conjugated antibodies were titrated and validated on glioblastoma, brain, liver, and tonsil tissue.

### Sample preparation and staining for imaging mass cytometry

10  $\mu$ m thick tissue sections on SuperFrost plus slides (R. Langenbrinck GmbH, 03-0060) were dried at 37°C for one minute and fixed in 100% methanol for 30 min at -20°C. Slides were rinsed three times in TBS for 5 min each. Tissue sections were encircled with a PAP pen (ImmEdge, Vector laboratories, H-4000) and blocked for 45 min at room temperature using SuperBlock (TBS) Blocking Buffer (ThermoFisher Scientific, 37581). The sections were then stained with a mix of metal-labeled primary antibodies diluted in TBS with 0.5% BSA as well as 10% FBS and incubated at room temperature for 1 h. Slides were rinsed in TBS-T (TBS supplemented with 0.2% Tween-20) twice and twice in TBS for 5 min each. Tissue sections were then stained with Iridium Cell-ID intercalator (500  $\mu$ M, Fluidigm, 201192B) diluted 1:2000 in TBS for 30 min at room temperature. Slides were rinsed three times for 5 min in TBS, dipped in ddH<sub>2</sub>O for 5 s and air-dried. Slides were stored at room temperature until image acquisition.

### Image acquisition

Two to three 1,000  $\mu$ m<sup>2</sup> ROI's per patient sample were acquired using a Hyperion Imaging System (Fluidigm). Tissue sections were laser ablated spot-by-spot at 200 Hz resulting in a pixel size/resolution of 1  $\mu$ m<sup>2</sup>. Preprocessing of the raw data was conducted using the CyTOF software v7.0 (Fluidigm, CA, USA) and image acquisition control was performed using MCD Viewer v1.0.560.6 (Fluidigm, CA, USA).

### Hypoxia treatment and methylome analysis

The investigated cell lines were treated in long-term hypoxia and normoxia conditions, respectively. We performed 850k EPIC methylation analysis (as described previously, Neuropathology Hamburg, Ulrich Schüller (Maire et al., 2021), from the published paired samples: GS-10H, GS-10N, GS-11H, GS-11N, GS-12H, GS-12N, GS-13H, GS-13N, treatment and conditions were described previously (Kathagen et al., 2013).

### Data import, preprocessing, filtering, and normalization for spatial data analysis

Data were analyzed and quality controlled by the cell ranger pipeline provided by 10X Genomics. For further analysis we developed a framework for spatial data analysis. The cell ranger output can be imported into SPATA by either a direct import function (SPATA: initiateSpataObject\_10X) or manually imported using count matrix and barcode-coordinate matrix along with the H&E staining. The routine import applies following steps via the Seuratv4.0 package: To normalize gene expression, values of each spot were divided by the estimated total number of transcripts and multiplied by 10,000, followed by natural-log transformation. As described for scRNA sequencing, we removed batch effects and scaled data using a regression model including sample batch and percentage of ribosomal and mitochondrial gene expression. A detailed description is provided in the supplementary methods and results.

### Detection of cell number per spot

In a first step, we trained a pixel-wise classifier for automated segmentation of each nucleus (ilastik, (Berg et al., 2019)). The output contained a grayscale probability map for the ilastik prediction values per pixel, in .tif format. We then loaded the probability map into CellProfiler (Carpenter et al., 2006) to identify nuclei as primary objects. The following Parameters were chosen to optimize the object identification: (1) Object diameter min: ~3 max: ~15 (adjusted based on the input image resolution) (2) Thresholding method: Two-class Otsu with a smoothing scale of 1.33, lower bounds: 0.3 upper bounds: 1.0, (3) Threshold strategy "Adaptive" with a window of 50. The identified objects were then exported as .csv files. For accurate determination of cells/spot, we imported the space ranger file (.../outs/) into SPATA2, using the command SPATA2::initiateSpataObject\_10X(). Next, we removed spots not "under tissue", as

observed from the histology image (see our tutorial: <https://themilolab.github.io/-SPATA2/articles/spata-v2-object-initiation-and-manipulation.html>). We then counted the number of cells within the boundaries of each spot using a wrapper function (*\*Cellnumber\_pred.R*). The script is available at [github.com/theMILOLab/](https://github.com/theMILOLab/)

In detail, the following steps were performed to quantify the cell/spot measurement:

- (1) Compute scaling factors between high-resolution image (used for segmentation) and the low-resolution image (used to annotate the spots in the image). The scale factors are saved in the “scalefactors\_json.json” output of the space ranger.
- (2) Co-register spots and segmented nuclei using the *point.in.poly* function of the *sp* package (Bivand et al., 2013).

#### Algorithm R:

```
for all  $S_n$  do
  for all  $S_p$  do
    Spot.segment  $\leftarrow$  swfscMisc::circle.polygon( $x = S_p.x$ ,  $y = S_p.y$ ,  $radius = adaptive.r$ )
    cell.spot  $\leftarrow$  sp::point.in.polygon (Spot.segment[ $x$ ,  $y$ ], Nuclei[ $x$ ,  $y$ ,  $N_n$ ])
    return(cell.spot)
output  $\leftarrow$  data.frame( barcode( $S_n$ ),  $S_n.x$ ,  $S_n.y$ , cell.spot $_n$ )
```

Variables:  
 $S_n$  = Vector of samples  
 $S_p$  = Vector of spots  
 $adaptive.r$  = Radius of spot multiplied by scaling factor  
 $N_n$  = Total number of nuclei

To validate the segmentation, we compared manual segmentation of 15 Images with cell profiler (object identification), ilastik (object identification) and a combination of Ilastik (probability map, Method3) and the object identification with cell profiler. The manual segmentations were used as ground truth to compare and evaluate the respective algorithms. Two strategies were used to validate the accuracy of each segmentation algorithm. First, we measured the overlap of the images by CellProfiler (Modul: *MeasureImageOverlap*, Test: F-Score-Measurment) resulting in a mean f-Score for CellProfiler (object identification): 0.548, ilastik (object identification): 0.633, and Ilastik + CellProfiler: 0.841. Next, we validated the numbers of cells per spot across the different method resulting in accuracy of 93.2% for Ilastik + CellProfiler, 83.1% ilastik and 67.3% CellProfiler. Our validation suggested that the combination of Ilastik + CellProfiler was superior and was therefore implemented in our analysis pipeline.

#### CNA estimation

For CNA analysis we implemented a CNA pipeline into our SPATA R tool available in the development branch, <https://github.com/theMILOLab/SPATA>. Copy number variations (CNVs) were estimated by aligning genes to their chromosomal location and applying a moving average to the relative expression values, with a sliding window of 100 genes within each chromosome, as described recently (Patel et al., 2014). First, genes were arranged in accordance with their respective genomic localization using the InferCNV package (R-software)<sup>8</sup>. As a reference set of non-malignant cells, we used a spatial transcriptomic dataset from a non-malignant cortex sample. To increase speed and computational power, down-sampling is optional. To avoid considerable impacts of any particular gene on the moving average, we limited the relative expression values to a range of  $[-2.6, 2.6]$ , replacing all values above/below to  $exp_{ij} = |2.6|$ , using the InferCNV package (R-software). This was performed only in the context of CNA estimation as previous reported (Tirosh et al., 2016b). The exported .RDS output files were then reimported and grouped by chromosomal averages of estimated CNA and aligned to their spatial position using the *fdata* slot of the SPATA object. Using the *SPATA::joinWithFeatures()* function, we then extracted cluster-wise comparisons. CNA analysis of spatial data is implemented in SPATA2 through the *SPATA2::runCnvAnalysis()* command. In a next step, we rearranged the estimated CNA values to defined chromosomal bins. These bins are created by the SPATAwrappers function *Create.ref.bins()*, with the SPATA object and the size of the given bins as input. In this manuscript, we used a bin size of 1Mbp, resulting in 3847 chromosomal bins with a mean coverage of 5.5 genes per bin. Rescaling and interpolation were carried out using a 10kbp sliding window. For normalization, we used a loess regression model, built to determine the copy-number values from the InferCNV output. Interpolation and normalization were performed using the *SPATAwrappers::runCnv.Normalization()* function.

#### CNA subclone analysis

To determine subclones based on the CNA data, we performed PCA analysis followed by KMeans clustering of the first 30 components as recently described (Zhao et al., 2022). To determine the optimal tree cut, we estimated the Calinski-Harabasz index and used the first peak of the  $k \sim CH$  index curve (CH index vs Number of clusters). The next aim was to quantify the spatial correlation and overlap of spatially distinct transcriptional programs with the subclonal architecture. First, we estimated the distance ( $S_{dist}$ ) of each spot ( $S_1, S_2, \dots, S_k$ ) of a given CNA subclone to the KMeans centroid ( $c$ ) through the fitted values ( $f(c_k)$ ) as follows:



$$S_{dist} = \sqrt{\sum_{i=1}^k (c - f(c_k))^2}$$

Spots with a low distance were removed ( $S_{dist} < \text{quantil}(S_{dist}, 0.9)$ ) from further analysis. We then estimated the dominating spatially distinct transcriptional program of all given spots and quantified the percentage of expression of each transcriptional program in a given subclone.

### Prediction of tumor cell content

Analyses and algorithms that have been established for single cell sequencing studies are not necessarily suitable to the analysis of spatially resolved transcriptomic data. This is mainly due to the unclear cellular composition within each spot and an advantage in analyzing this data would be to approximate the true composition of each spot. The integration of single-cell data and spatial transcriptomics already allows for the prediction of the probability of residence of some cell types, but in tumors, such a prediction is difficult due to the enormous heterogeneity within and between samples. In contrast to highly variable gene expression, chromosomal alterations are a rather robust and suitable parameters for the evaluation of the tumor cell content of each spot. To train and validate a prediction model, we performed single-cell sequencing and corresponding spatially resolved transcriptomics from the same donor. We inferred copy-number alterations of the scRNA-seq dataset and extracted signatures of both tumor and non-malignant cells which showed a large similarity as shown in [Figures S6I](#) and [S6J](#). Next, we validated the extent to which the inferred CNAs called from RNA-seq data reflect CNAs that were detected in DNA sequencing. Therefore, we used the recent published slide-RNA-seq and slide-DNA-seq dataset and compared the CNAs detected by both spatial sequencing approaches, [Figures S6B–S6I](#). Both validation methods revealed that inferred CNAs obtained from spatial transcriptomics reflect actual chromosomal gains and losses in spatially resolved transcriptomics obtained using the 10X Visium platform. Given the fact that CNA's can be utilized to detect tumor content, we trained a model from simulated data to predict the percentage of tumor cells per spot. The following approach encompasses three steps:

(1) *Simulation of a spatial training data set:* To simulate spatially resolved transcriptomic data with different ratios of healthy and malignant cells, we created a training and test dataset for various models. The composition of each spot  $S_n$  with a given number at cells per spot  $n$  was defined as follows:

$$S_n = t_{\frac{n}{n}} + h_{\frac{n}{n}}$$

where  $t$  : tumor cells from the scRNA-seq data set,  $h$  : non-malignant cells, with the frequency of  $n_h$ . The expression of a gene  $g$  was determined as follows:

$$g_s = \frac{\sum_{i=1}^{at} g_i + \sum_{i=1}^{an} g_i}{n}$$

For the CNA dataset,  $CNV_s$  of each spot consisted of averaged chromosomal alterations  $g_s\{Chr1, \dots, Chr21\}$  obtained by varying the numbers of cells per spot  $n = \{2, \dots, 20\}$ . The final training dataset included 2000 training spots with 19 different cell numbers, resulting in a total of 38,000 spots. For internal validation a test dataset was simulated using the same parameters.

(2) *Linear models used for quantification of tumor-cell content:* To approximate the relation between chromosomal alterations in healthy and tumor spots, we trained a loess model to predict the tumor cell content based on gain of Chr7, which is a hallmark of GBM that appeared in most samples. First, we centered the estimated CNA gain and fitted the gain of  $CNV \sim \frac{n_t}{n_h}$  by loess fit.  $n_t$  represents the number of tumor cells per spot.

$$n_{CNVi} = \frac{A_{CNVi} - \min(A_{CNV})}{\max(A_{CNV}) - \min(A_{CNV})}$$

$$\hat{f}_h(CNV_i) = \frac{1}{n} \sum_{i=1}^n K_h(CNV - CNV_i)$$

$K$  is the kernel and  $0.8 > h > 0.2$  was used to adjust the estimator. As illustrated in the [Figure S2G](#), the amplification of Chr7 showed a robust correlation to the tumor cell content in our simulated dataset ranging from 2 to 20 cells per spot, compared to non-altered chromosomal regions (noise), [Figure S1G](#). Although, alterations in Chr7 alone provides a significant correlation to the tumor cell content, the low signal-to-noise ratio hampered accurate prediction, [Figure S1G](#).

(3) *Implementation of neural network for quantification of tumor-cell content:* To provide improved quantification, we considered the above-mentioned biases in spatially resolved datasets and created simulated spots that were predominantly composed of sub-clones to avoid this source of bias. Our parameters were defined as follows: The defined training data set  $CNV = \{cnv_i^k\}$ ,  $i = 1, \dots, N$  and the number of cells  $N = \{n^k\}$ ,  $i = 1, \dots, N$ , which result in the prediction of  $Y \sim w_o + w_i x_i$ . For the model, we trained a sequential neural network consisting of 3 hidden layers (64, 32, 16). In order to avoid overfitting, the dropout rate was set to 0.1. The model was then compiled using a mean square error (MSE) loss function with a RMSprop optimizer. To account for the different number of cells

per spot, we followed our above-mentioned approach, training 19 different models ranging from 2 to 20 cells per spot. We validated our model using multiple simulated data sets from different patients, with an overall accuracy of 95% and significant correlation between training and validation datasets ( $R^2 = 0.93$ , IQR: 0.87–0.96,  $p < 0.0001$ ), [Figures 2B](#) and [S1H](#). This was true for spots with more than 5 cells, with the classifier only able to predict tumor or non-tumor state of spots with <5 cells.

### Determination and prediction of the histological context

The H&E staining's were classified based on their histological morphology. We started by created a dataset of defined histological classification from cropped 500 × 500 pixel images at random positions across samples from all patients. The images were then classified by experienced neuropathologists in accordance with the classification system of the Ivy-gap database into the categories: "Infiltrating", "Necrosis", "Necrotic Edge", "Cellular", "Vascular" and for normal brain white matter and cortex. These images were used as a ground truth to train a pretrained Convnet Architecture (VGG16 architecture `keras::application_vgg16`). The training and prediction were performed using the `keras::` and `tensorflow::` package, [Figures S1D](#) and [S1E](#). We estimated the likelihood of the histology of a given spot based on the prediction values of the neural network. Additionally, we used the transcriptional data for an integrative estimation of histology. Spots with a total UMI count under the 10<sup>th</sup> percentile and a high likelihood of necrosis (>0.5) were classified as necrosis. This optimization was performed to improve the spatial resolution of histology in areas with a sharp border between necrosis and necrotic edge. To validate the classification, we performed segmentation of the histological images ( $n = 4$ ) using the `SPATA2::createSegmentation()`, revealing large overlap with predicted histology (F-score = 0.893).

### Sample-wise cluster analysis for spatially resolved transcriptomics

To identify recurrent spatially distinct transcriptional programs, we started clustering our spatially resolved transcriptomic dataset on a patient by patient basis due to the large interpatient heterogeneity recently as described ([Neffel et al., 2019](#)). First, we transformed our `spata`-object into `seurat`-objects (`SPATA2::transformSpataToSeurat()`) and removed all spots with predicted tumor content below 90%, spots with low UMI counts (<1,000), low number of detected genes (<400) and high percentage of mitochondrial genes (>50%). Next, we estimated the cell phase using the `CellCycleScoring()` function in Seurat. Normalization, scaling, and regression was performed using the `SCTransform()` function with `vars.to.regress <- c("percent.mt", "S.Score", "G2M.Score")`. We used the 2000 most variable expressed genes to decomposed eigenvalue frequencies of the first 30 principal components. We used either the PCA analysis implemented in `Seuratv4.0` ([Hao et al., 2021a](#)) or a generalized principal component analysis (GLM-PCA) for non-normal distributions ([Townes et al., 2019](#)) due to the fact that our UMI counts follow multinomial sampling. For further analysis we used the first 30 non-trivial estimated eigenvectors. Based on the PCA analysis, we performed clustering using 5 different cluster algorithms and estimated the optimal number of clusters or cluster resolution as follows: For graph-based clustering, a Euclidean distance matrix was computed to identify pairs of cells with shared neighbors similar to the SNN-Cliq approach (Louvain-, and smart local moving (SLM) clustering). We iterated the cluster resolution `res = {0, ..., 1.5}` (step size = 0.025). Cluster integrity was estimated by the highest modularity of each cluster from a graph, based on random connections between nodes ([Lun et al., 2016](#)). We then computed the cluster stability using the `clustree` package ([Zappia and Oshlack, 2018](#)) to determine the optimal resolution for final clustering. This approach is embedded in the `SPATAwrappers` package in the function `runFullclustervalidation()`. For kMeans, Partitioning Around Medoids (PAM) and hierarchical clustering, the optimal k was determined using gap statistics. We then validated the cluster recall and precision by f-statistics, excluding clustering approaches with a f-score < 0.7. We next integrated the cluster algorithms using the `clustree` package (`clustree::clustree_overlay`) and estimated the cluster architecture with the highest overlap of all methods, resulting in coherent clusters reflecting robust cluster assignments, further referred to as "consensus clusters". Next, we estimated differential expressed genes of the consensus clusters using the Wilcox method of the `FindAllMarkers()` function in Seurat. We subsequently removed clusters with redundant marker genes (>20% overlap of significant marker genes with FDR < 0.001), clusters with fewer than 50 significant genes ( $\log_{2}FC > 0.25$  and  $\text{padj} < 0.001$ ). P value adjustment was carried out using the Benjamini-Hochberg method. The remaining gene signatures were integrated across all clusters to identify recurring transcriptional programs.

### Horizontal integration and identification of spatially distinct transcriptional programs

To compute the recurring transcriptional programs, we performed data integration in both the transcriptional and cartesian space. (1) *Transcriptional space*: Using the above identified common regulator genes as anchors, we performed reciprocal PCA to integrate all stRNA-seq datasets. This method was able to integrate all preprocessed tumor samples into a single reference PCA space. This merged projection was further processed by cluster analysis of the five different algorithms described in STAR Methods: "Sample-wise cluster analysis for spatially resolved transcriptomics". The resulting cluster overlay analysis (`clustree` package) revealed five distinct programs. Next, we performed differential expressed genes of the distinct programs using the Wilcox method in the `FindAllMarkers()` function in Seurat. The most significant and unique classified genes ( $\log_{2}FC > 0.25$  and  $\text{padj} < 0.001$ ) were summarized to build the transcriptional signature of the "spatially distinct transcriptional programs". (2) *Cartesian space*: To evaluate the spatial overlap of all determined patient individual consensus clusters ( $n = 99$ ), we used the most significant marker genes ( $\log_{2}FC > 0.25$  and  $\text{padj} < 0.001$ ) to build consensus cluster signatures. We then performed spatially weighed correlation analysis of the consensus cluster signatures (STAR Methods: [Spatially weighted regression analysis](#)), individually for each sample. The resulting correlation array with the shape  $[c, c, n]$  ( $c$  = consensus cluster signatures and  $n$  = number of samples 16) was reduced by mean to a  $c \times c$  correlation matrix. Hierarchical clustering of the correlation matrix was then carried out, estimating the optimal number of k using the

Calinski-Harabasz index, resulting in 5 clusters. Both methods, the cluster analysis in transcriptional and cartesian space showed a high similarity (Jaccard-Index 0.746, based on the genes of the consensus cluster signatures).

### Pathway analysis of gene sets

We performed pathway analysis using three different methods all implemented into our SPATA toolbox. As presented in our figures we used gene set variation analysis (GSVA) or z-scored enrichment of gene sets. The analysis was performed through the GSVA package (Hänzelmann et al., 2013). For GO-term enrichment we used the DOSE package and cluster profiler (Yu et al., 2012).

### Spatial gene expression

The visualization of spatial gene expression is implemented in the SPATA software *SPATA::plotSurfaceInteractive*. For spatial expression plots, we used either normalized and scaled gene expression values (to plot single genes) or enrichment scores of a defined genesets, using the 0.5 quantile of a probability distribution fitting. The x-axis and y-axis coordinates are given by the input file based on the localization to the H&E staining. We computed a matrix based on the maximum and minimum extension of the spots used (32x33) containing gene expression or computed scores. Spots without overlaid tissue were set to zero. Next, we transformed the matrix, using the squared distance between two points divided by a given threshold, implemented in the fields package (<https://github.com/dnrychka/fieldsRPackage>, R-software) and adapted the input values by increasing the contrast between uncovered spots. The data are illustrated as surface plots (plotly package R-software) or as images (graphics package, R-software).

### Spatial autocorrelation Moran's I

Spatial autocorrelation determines the spatial dependencies of spots to its neighbors based on feature locations and attribute values using Moran's I-statistics values. This allows to evaluate whether a defined gene expression or feature is grouped, distributed or random. If the Z-score or p-value indicates statistical significance, a positive Moran's I-index value indicates a tendency to cluster and a negative Moran's I-index value indicates a tendency to scatter. The autocorrelation is defined as:

$$I = \frac{N}{W} \frac{\sum_x \sum_y w_{xy} (exp_x - \overline{exp})(exp_y - \overline{exp})}{\sum_x (exp_x - \overline{exp})^2}$$

where  $N$  defines the number of spatial spots with the index  $x$  and  $y$  and the matrix of spatial weights as  $w_{xy}$ . The feature is indicated by  $exp$  and  $\overline{exp}$  the mean value of neighboring features. The spatial weights were defined as a distance matrix of the cartesian space.  $W$  is defined as the sum of all  $w_{xy}$ . We embedded the autocorrelation into the SPATAwrappers package by the function *inferSpatial.ac()*.

### Spatially weighted regression analysis

Correlation coefficient in spatially resolved data needs to be addressed differently compared to data where every datapoint can be assumed to be independent. In the context of spatial weighted correlation measurements, the model needs to be corrected for effects of local neighbor dependencies. For example, if the same cell drives similar activation of two adjacent spots, it cannot be considered non-stationary in the spatial context. To address this issue, geographically weighted models are used. The spatial transcriptomic data have the particularity that the neighborhoods correspond to a fixed distance and do not vary in their distance. We have used the following models within our analyses: (1) Spatially weighted correlation based on geographical weighted correlation, allowing to test for non-stationarity. We performed Monte Carlo testing as following: (i) Computation of the true correlation based on all spots within the area or sample under study. (ii) This is followed by a random selection of a permutation of the spots, preserving the spatial coordinates of the same parameters. (iii) Determination of a simulated correlation at all spots using randomized data from the step (ii). (iv) Repeating steps (ii) and (iii)  $n$  times, 299 iterations in our case. (v) At each spot, the rank of the one true correlation within the distribution of the simulated correlations was determined. To be considered significant, the true correlation needs to be in the upper or lower 2nd 5% tail of the ranked distribution.

The second model was used to determine local regression. The second model was used to explore local variations in data relationships via local regression coefficients and associated estimates using a "geographic weighted regression model", adopted and optimized to the spatial transcriptomic context. The basic model is defined as

$$y_i = \beta_{i0} + \sum_{k=1}^m \beta_{ik} x_{ik} + \varepsilon_i$$

Where  $y_i$  is the dependent variable at location  $i$ ;  $x_{ik}$  is the value of the  $k$  th independent variable at location  $i$ ;  $m$  is the number of independent variables;  $\beta_{i0}$  is the intercept parameter at location  $i$ ;  $\beta_{ik}$  the local regression coefficient for the  $k$  th independent variable at location  $i$ ; and  $\varepsilon_i$  is the random error at location  $i$ . This basic model does not account for varying relationships between stationary and non-stationary coefficients. A semi-parametric mixed geographic weighted regression model was introduced and implemented in GWmodel (Gollini et al., 2015; Lu et al., 2014). A non-adaptive approach was adopted since the distance within spots is assumed constant. The weighted matrix  $w_{ij}$  was calculated by either a Gaussian  $w_{ij} = \exp(-d_{ij}^2/h^2)$  or bi-square kernel:  $w_{ij} = 1 - (d_{ij}^2/h^2)^2$ , where  $d_{ij}$  is determined as the distance between the spot  $i$  and  $j$ .  $h$  is defined as the bandwidth. The optimal bandwidth was determined by cross-validation. In R language, the GWR was computed as follows:

**Algorithm R:**

**for all P do**

*Optimal.h* < - *spgwr:gwr.sel*( $P_a \sim P_b$ , *adapt* = F)

$$CV = \sum_i [y_i - \hat{y}_{\#i}(\hat{\beta})]^2$$

*gwr.model* < - *spgwr:gwr*( $P_a \sim P_b$

*bandwidth* = *Optimal.h*,

*gweight* = *gwr.bisquare*)

Variable:

P= Vector of variables

**Analysis of spatially defined trajectories**

A given trajectory includes multiple spots summarized into predefined bins along the directed trajectory. In order to model the gene expression of single genes or genesets, we created a set of mathematical models representing defined biological behaviors, including linear, logarithmic, or gradient ascending/descending expression patterns, one-, or multiple peak expression, detailed information in the package description. The analysis is implemented into the function *assessTrajectoryTrends()*. Further, if a defined pattern is requested, we allow the possibility to add a vector containing the requested model that the algorithm will screen for. Next, we fitted the summarized expression values of each bin using a non-parametric kernel estimation (Gaussian or Cauchy-Kernel), input vectors were normalized and z-scored:

$$n_{\text{exp } i} = \frac{A_{\text{exp } i} - \min(A_{\text{exp}})}{\max(A_{\text{exp}}) - \min(A_{\text{exp}})}$$

$$\hat{f}_h(n_{\text{exp } i}) = \frac{1}{n} \sum_{i=1}^n K_h(n_{\text{exp}} - n_{\text{exp } i})$$

Where K is the kernel and  $0.7 > h > 0.3$  is used to adjust the estimator. Next, we computed residuals for each input vector (gene expression) and estimated area under the curve (AUC) using the trapezoidal numerical integration.

$$\int_b^a f(\text{res}) dx \approx \sum_{k=1}^n \frac{f(\text{res}_{k-1}) + f(\text{res}_k)}{2} \Delta \text{res}_k$$

The distance and direction are defined by [a,b]  $a = x_0 < x_1 < \dots < x_{n-1} < x_n = b$ . We use the AUC to rank the estimated models and predict genes that follow our predefined behavior. The implemented function *plotTrajectoryFit()* shows the model fit with respect to the given residuals.

**Estimation of regional gene expression variance by local vector field estimation**

Within a spatially determined dynamic system, the state of each point can be represented as a vector ( $\mathbf{x}$ ) in a multidimensional space whose elements represent the transcriptional and metabolic space. Metabolic differences in space are often associated with spatial gradients. To identify and compare these gradients, we determine the spatial changes as a vector within the vector field  $\mathbf{f}$ , composed of the coordinates  $\mathbf{x}$  in the d-dimensional space of all spots resulting in a vector  $\mathbf{v}$  in the same space, i.e.,  $\mathbf{v} = \mathbf{f}(\mathbf{x})$ . We started by transforming the gene or metabolic space by a biweight kernel  $K(u) = \frac{15}{16}(1 - u^2)^2 |u| \leq 1$ . The following 2D kernel density estimator (KDE) was used:

$$f(p) = \frac{1}{p} \sum_{i=1}^p K_h(\delta p - \delta p_i)$$

K is the kernel and  $0.3 > h > 0.1$  is used to adjust the estimator. In the next step, we estimated the vector field based on local variances in the cartesian space (dimension:  $\mathbf{x}, \mathbf{y}$ ) and gene expression space (dimension  $\mathbf{z}_1, \mathbf{z}_2, \dots, \mathbf{z}_n$ ). We calculated a distance matrix of all spots and determined the nearest neighbors (within a 200  $\mu\text{m}$  distance). The vector was determined by  $f(x, y) = (x, y)i + (x_{\max(\delta)}, y_{\max(\delta)})j$ . Each spot  $S = \{S_1, \dots, S_{n-1}, S_n\}$  with its coordinates  $x, y$  a vector field in  $\mathbb{R}^2$  based on the feature  $\delta = \{\delta_1, \dots, \delta_{p-1}, \delta_p\}$  whereby

$$\delta \begin{cases} \text{if } p = 1 \rightarrow \delta = \delta_1 \\ \text{if } p > 1 \rightarrow \delta = f(p) \end{cases}$$



for multiple genes. We embedded the analysis in the *SPATAwrappers* package available on GitHub (<https://github.com/heilanddd/SPATA-wrappers>) under the function *SPATAwrappers::inferVectorFields()*. In the next step, we visualized the vector fields either by arrow plots (*SPATAwrappers::plotVectorFields()*) or streamline plots. To generate the streamline plots, we utilized the ggplot based package *metR* (<https://github.com/eliocamp/metR>) in the *SPATAwrappers::plotStreamlines* function. The function estimates streamline as follows:

Output of the vector field estimation is a *data.frame* with the vector *x*, *y*, *t.x*, *t.y* of each given barcode.

#### Algorithm R:

1. Estimate a grid:  
`sf::st_make_grid(n = grid) # grid <- c(50,50)`
2. Estimate median vectors in grid  
`for all grid(x,y) do median(x.t); median(y.t)`
3. Barnes interpolation (Koch and DesJardins, 1983):  
`x.t_inter <- oce::interpBarnes( grid$x , grid$y , z = mean_grid(x.t), gamma = 0.2)`  
`y.t_inter <- oce::interpBarnes( grid$x , grid$y , z = mean_grid(y.t), gamma = 0.2)`
4. ggplot integration  
`p + metR::geom_streamline(data , aes(x = grid$x, y = grid$y, dx = x.t_inter, dy = y.t_inter))`

#### Identification of cycling cells

We used the set of genes published by Neftel et al. to calculate proliferation scores based on the GSVA package implemented in R-software. The analysis was based on a non-parametric unsupervised approach, transforming a classical gene matrix (gene-by-sample) into a gene set by sample matrix, resulting in an enrichment score for each sample and pathway. From the output enrichment scores, we set a threshold based on distribution fitting to define cycling cells.

#### CNA analysis from EPIC data

For copy number variation (CNV) analysis from EPIC data, raw signal intensities were obtained from IDAT files using the minfi package (Aryee et al., 2014). CNV analysis from methylation array data was performed using the *conumee::cnv.fit* and *conumee::cnv.bin* functions of the *conumee* package (version 1.22.0) (Hovestadt and Zapatka, 2015). For genome segmentation, a custom script was used, calculating running means from 12 bins in + and - directions and combining adjacent bins with similar running means with a cutoff at 0.05. A control set of non-tumorous brain was used (n = 6) as a reference data set to determine the baseline copy number state, as recently described (Maire et al., 2021).

#### Methylation analysis of the MGMT promotor

To evaluate the MGMT promotor methylation, we filtered the 850k data by the TSS1500, TSS100, 5'URT and first exome of the MGMT from chromosomal position Chr10:1312640000 to Chr10:1312645500, resulting in 22 CpG islands. To determine the MGMT methylation status, the two CpG islands are of superior importance: cg12434587 and cg12981137 accordingly to a previously published study (Bady et al., 2012). Comparison between hypoxia treatment and normoxia condition was performed by Wilcoxon-rank statistics.

#### MALDI data analysis

We imported the files into R using the *readImzML* function from the *cardinal* package (Bemis et al., 2015). We reshaped the pixelwise data matrix into an intensity matrix and a matrix of coordinates for each tumor separately. We filtered the m/z matrix to annotated peaks (METASPACE database) using the *match.closest* function from the *MALDIquant* package, resulting in a metabolic intensity matrix (Gibb and Strimmer, 2012). The intensity matrix and the corresponding spatial coordinates were imported into a SPATA object for further spatial data analysis using the *SPATA::initiateSpataObject\_MALDI*.

#### Alignment of metabolic and stRNA-seq data

Matrix embedding techniques differ between stRNA-seq and metabolic imaging, with the reference H&E staining's from each modality revealing significant differences. In order to approximate image alignment, we performed feature-based alignment and dynamic transformation. We utilized the *image.dlib* a C library for image analysis and computed image features by the function *image\_surf*. The SURF method is based on the sum of the Haar wavelet response around the point of interest as previously described (Bay et al., 2008). Next, we estimated the affine transformation parameters using the minimized cost function as described recently (Abuzneid and Mahmood, 2017). Through this approach, we were able to map the metabolic data to the reference stRNA-seq dataset, Figure S7A. After both images were approximately merged, non-correlating sections (especially edge or artefact areas) were excluded from further analysis, Figure S7A. Due to the different resolution across data modalities, spot-wise fusion of metabolic

and transcriptomic data was necessary. To estimate the metabolic intensities at a given spot  $S = \{s_i^k\}$ ,  $i = 1, \dots, S$ , with the coordinates  $(x, y)$  we determined the metabolic intensities  $m \in S$  with  $n$  metabolic intensities and averaged them

$$S_m = \frac{\sum_{i=1}^k m_i}{n} \text{ US}$$

### Data integration and clustering of metabolic data

Analogous to the methods used for transcriptomic data analysis, we used reciprocal PCA for horizontal integration, with metabolite intensities acting as anchors for the metabolic data (described in STAR Methods: [Horizontal integration and identification of spatially distinct transcriptional programs](#)). Next, we use the cluster analysis methods mentioned above, including iterative determination of resolution and

Cluster stability. Because of the difference in the number of clusters between stRNA-seq and metabolic data, the f-score was determined by increasing number of clusters ( $k$ ). This resulted in the spatial organization showing a high degree of agreement, especially in areas of low  $k$  values. In order to vertically integrate both metabolic and transcriptional data, we performed the weighted nearest neighbor integration ([Hao et al., 2021b](#)) with the `FindMultiModalNeighbors()` function from the Seurat package. The following parameters were used: `dims.list = list(1:8, 1:30)`, `smooth = F`, `k.nn = 15`. Next, we performed dimensional reduction from the resulting  $k$ -nearest neighbor (kNN) using the `RunUMAP` function from the Seurat package. Shared nearest neighbor clustering was performed from the weighted shared nearest neighbor (wsNN) with iterative cluster resolutions to determine optimal resolution.

### Determination of hypoxia subgroups

In our analysis, we differentiate between hypoxia-core and hypoxia associated spots. Based on the weighted nearest neighbor integration, we found two clusters highly associated with the “reactive hypoxia program”. We classified these spots based on the mutual metabolic and transcriptional activation of hypoxia or transcriptional/metabolic activation alone. For metabolic data, we estimated the enrichment score of Lactate metabolism and glycolysis and for transcriptional data the “HALLMARK HYPOXIA” enrichment. We rescored the data from mutual activation enrichment score (ES) = 1. No enrichment was determined as ES = 0. We defined the hypoxia core as ES > 0.6, the hypoxia associated as  $0.4 < \text{ES} < 0.6$ . Random control spots were defined as ES < 0.4.

### Integrative cell cycle analysis and hypoxia metabolism

To estimate the relationship between cell cycle phases and hypoxia metabolism, we estimated the cell cycle parameters G1, S and G2M phase by the Seurat function `CellCycleScoring()`. Next, we used the `joinWith()` function of the SPATA2 package to estimate the hypoxia gene set enrichment score. The comparison was visualized by a scatterplot (x: hypoxia signature, y: G2M score).

### TCGA data analysis

For the TCGA data analysis, we downloaded the CNV and transcriptional data along with clinical information. First, we filtered the data for IDH wild-type glioblastoma. The Verhaak subtype was given in the clinical data information downloaded at: <http://gliovis.bioinfo.cnio.es> ([Bowman et al., 2017](#)). To determine the enrichment of the hypoxia signature, we estimated the mean gene expression of the hypoxia signature across the proneural, mesenchymal and classical subgroup. Next, we reclassified the samples as hypoxia (upper 0.2 quantil) and non-hypoxia (lower 0.2 quantil). We compared the patients of hypoxia and non-hypoxia using the CNA data revealing a larger variance in CNA's from the hypoxia group. The numbers of pathological losses and gains per sample was summarized as the genomic instability score and correlated to the hypoxia signature across all subgroups. Regression analysis was performed by a generalized linear model (glm) model  $\text{glm}(\text{hypoxia} \sim \text{genomic.instability})$ .

### Analysis of scRNA-seq

Single cell RNA-seq were processed by 10x Genomics Cell Ranger 3.1.0 ([Zheng et al., 2017](#)). Postprocessing was performed using the MILO-pipeline for scRNA-seq (<https://github.com/theMILOlab/scPipelines>). Single cell analysis was performed by the Seuratv4.0 package and SPATA 1.0 package. We used the Seurat wrapper for scVelo ([Bergen et al., 2020](#)) to perform pseudotime analysis and Cell Rank ([Lange et al., 2020](#)) for cell fate estimation. After preprocessing of the data through Seurat, we imported the data into SPATA. Further analysis was performed as explained in the sections above.

### RNA velocity estimation (single-cell data)

We used the CellRanger BAM file to separate expression matrices of spliced and unspliced reads through the ready-to-use pipeline from the velocityto package ([La Manno et al., 2018](#)). The resulting .loom file was read into the scVelo Seurat wrapper (<https://github.com/satijalab/seurat-wrappers>). We merged the Seurat objects and performed batch effect removal as explained above. After data integration, Seurat objects with exonic and intronic gene-level UMI counts were converted into h5ad format (<https://github.com/mojaveazure/seurat-disk>). We then imported the h5ad files to an AnnData object. Next we performed normalization and selected the 2,000 most variable expressed genes by the scVelo package (v0.2.3) ([Bergen et al., 2020](#)). We excluded all genes with less than 20 assigned reads across the exonic and intronic components and estimated RNA velocity and latent time using a dynamic model. Data was exported as .csv files and integrated into the SPATA object for further visualization. This pipeline is implemented into a SPATA wrapper for scVelo (SPATA::getRNAvelocity, in the development branch).

### Infer lineage differentiation by CellRank (single-cell data)

After generating the dynamic model, we estimated macrostates that represent initial, terminal as well as transient intermediate states using the CellRank package (v1.1.0, <https://github.com/theislab/cellrank>) (Bergen et al., 2020; Lange et al., 2020). We constructed a transition matrix using the connectivity kernel which was analyzed by Generalized Perron Cluster Cluster Analysis (GPCCA) (Reuter et al., 2018) after computing a Schur triangulation. We estimated the probability of all identified macro state (initial and terminal states) in each spot. The probability vectors were integrated into the fdata slot of the corresponding SPATA object. Lineage driver genes of each estimated macrostate were identified by the *compute\_lineage\_drivers* function of CellRank. Additionally, we used the partition-based graph abstraction (PAGA) to simplify state transition in space.

### IMC preprocessing

Raw data was processed by the Bodenmiller Pipeline (Zanotelli and Bodenmiller, 2022). For single-cell analysis we segmented the cells based on the nucleus (DNA-staining) using 6 random crops of each image for training. Training was performed by pixel-wise classification using ilastik (Berg et al., 2019). We imported the classification trained images into cell profiler to extract single cell intensities of segmented cells. We analyzed the spatially resolved single-cell matrix by SPATA. For import, we used the *SPATA::initiateSpataObject\_MALDI()* function and performed batch effect removal between images by matching mutual nearest neighbors (Haghverdi et al., 2018).

### IMC data integration

Horizontal data integration of IMC data was performed by mutual nearest neighbor analysis using fastMNN() from the batchelor package (Haghverdi et al., 2018). Data from each patient and localization (total n = 16) was load into a seurat object and the MNN was performed using the SeuratWrappers function (fastMNN()). The resulting MNN components were used for UMAP dimensional reduction and shared nearest neighbor clustering. To reduce data noise and batch effects across patients, we estimated an internal reference dataset of various cell types including inclusion and exclusion markers. The following cell types were defined Neurons: (NeuN<sup>+</sup>, SNAP25<sup>+</sup> & CD45<sup>-</sup>, GFAP<sup>-</sup>, EGFR<sup>-</sup>) Myeloid cells (CD45<sup>+</sup>, CD68<sup>+</sup>), T cells (CD3<sup>+</sup>, CD45<sup>-</sup> and CD68<sup>-</sup>, CD3<sup>-</sup>), tumor cells (EGFR<sup>+</sup>). We then performed rPCA analysis, aligning the whole data to its reference dataset.

### IMC neighborhood analysis

In order to compute spatial dependencies of a given cell to its neighborhood in the cartesian space, we integrated the single-cell position into a graph using the igraph package. Each cell represents a node with connections to the surrounding cells defined as edges, weighted by its cartesian distance. Next, we adapted the weights using a power function ( $b^n$ ) to reach scale-free topology in our network:  $P(k) \propto k^{-\tau}$  where  $\tau$  is any number and  $k$  the connections. Based on our model, we hypothesized that different cell types with high connectivity (numbers of connections) at short distance represent highly interacting cells, and cells with low connectivity in the neighborhood representing cells without interactions or random interactions. We used this model to estimate the interaction of immune cells (myeloid and T cells) to different subgroups (spatially distinct transcriptional programs).

### Integration of single-cell sequencing data into spatial transcriptomics

To integrate scRNA-seq and spatially resolved transcriptomic to define the position of immune cell populations, we used the published data from (Ravi et al., 2022). We estimated the likelihood of the spatial position or each cell type cluster using the spotlight algorithm, embedded into the SPATAwrapper package, function: *inferSpotlight* (Elosua-Bayes et al., 2021).

## QUANTIFICATION AND STATISTICAL ANALYSIS

No statistical methods were used to predetermine sample size. For cell-based and tissue culture experiments, biological triplicates were performed (tissue culture n = 6) in each single experiment in general, unless otherwise stated.

Statistical analysis was performed using R software 4.01 software. Two tailed *t*-test and Mann-Whitney test were used to compare condition vs. control. ANOVA models were used to compare continuous outcomes across multiple groups/conditions, unless otherwise indicated in each figure legend. Spatial data statistics and analysis workflows are states in the **METHOD DETAILS**.

## **Supplemental information**

### **Spatially resolved multi-omics**

### **deciphers bidirectional tumor-host**

### **interdependence in glioblastoma**

**Vidhya M. Ravi, Paulina Will, Jan Kueckelhaus, Na Sun, Kevin Joseph, Henrike Salié, Lea Vollmer, Ugne Kuliesiute, Jasmin von Ehr, Jasim K. Benotmane, Nicolas Neidert, Marie Follo, Florian Scherer, Jonathan M. Goeldner, Simon P. Behringer, Pamela Franco, Mohammed Khiat, Junyi Zhang, Ulrich G. Hofmann, Christian Fung, Franz L. Ricklefs, Katrin Lamszus, Melanie Boerries, Manching Ku, Jürgen Beck, Roman Sankowski, Marius Schwabenland, Marco Prinz, Ulrich Schüller, Saskia Killmer, Bertram Bengsch, Axel K. Walch, Daniel Delev, Oliver Schnell, and Dieter Henrik Heiland**



## **Supplemental information**

### **Spatially resolved multi-omics deciphers bidirectional tumor-host interdependence in glioblastoma**

Vidhya M. Ravi, Paulina Will, Jan Kueckelhaus, Na Sun, Kevin Joseph, Henrike Salié, Lea Vollmer, Ugne Kuliesiute, Jasmin von Ehr, Jasim K. Benotmane, Nicolas Neidert, Marie Follo, Florian Scherer, Jonathan M Goeldner, Simon P. Behringer, Pamela Franco, Mohammed Khiat, Junyi Zhang, Ulrich G. Hofmann, Christian Fung, Franz L. Ricklefs, Katrin Lamszus, Melanie Boerries, Manching Ku, Jürgen Beck, Roman Sankowski, Marius Schwabenland, Marco Prinz, Ulrich Schüller, Saskia Killmer, Bertram Bengsch, Axel K. Walch, Daniel Delev, Oliver Schnell, Dieter Henrik Heiland

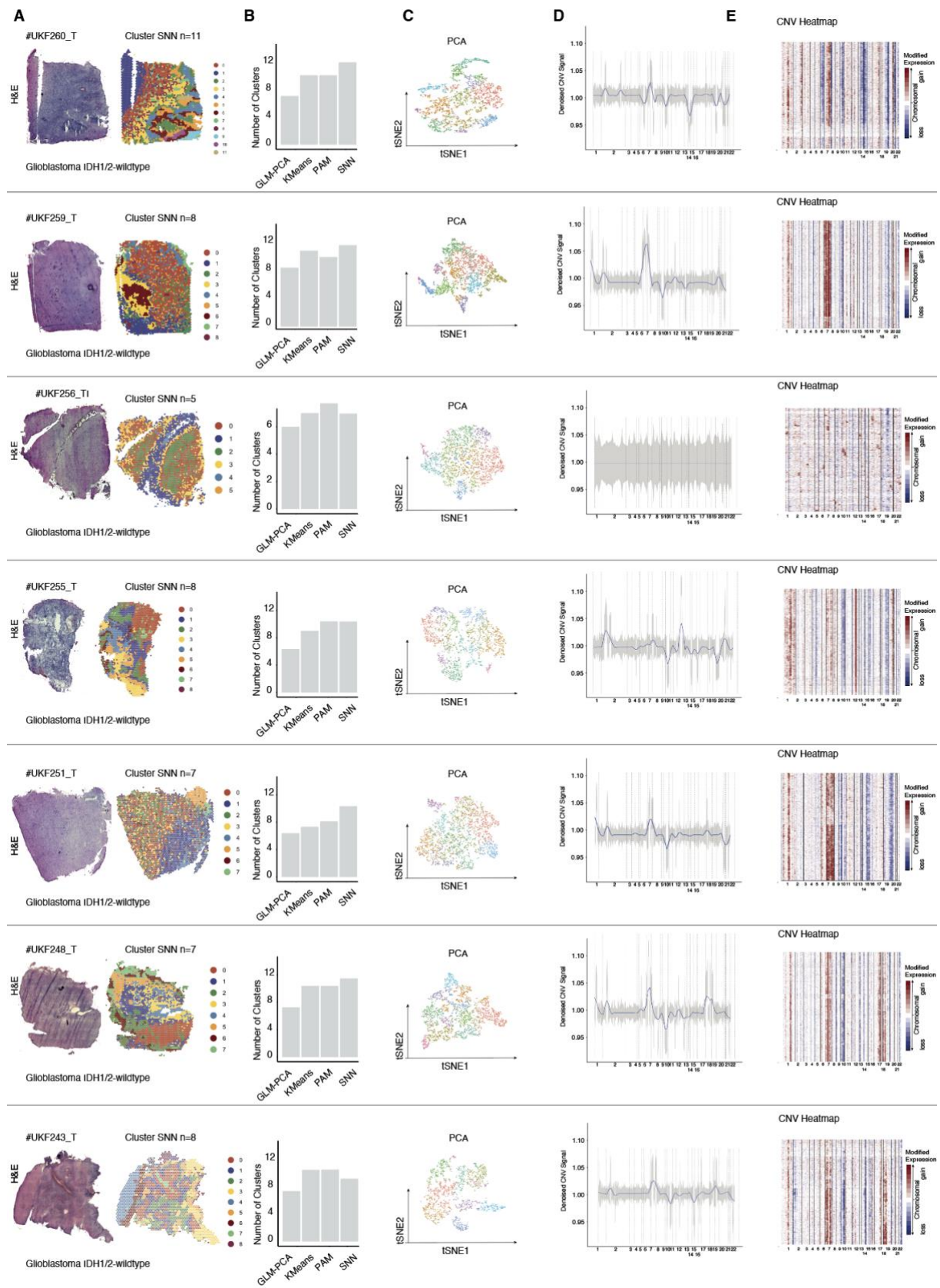
12 **Table S1: Overview of the cohort related to Figure 1**

ID	Tissue Type	Batch	Region	Age	Tumor	Histology	Sex	MALDI	IMC
#275UKF	T	6	frontal	80	IDH-WT	GBM	f	1	1
#270UKF	T	6	frontal	41	IDH-MUT	AA	m		
#269UKF	T	6	occipital	51	IDH-WT	GBM	m		
#268UKF	T	6	frontal	49	IDH-MUT	ODG	f		
#266UKF	T	6	temporal	76	IDH-WT	GBM	f		
#265UKF	C	2	temporal	55	C	Cortex	m		
#265UKF	T	2	temporal	55	IDH-WT	GBM	m		
#262UKF	T	5	temporal	59	IDH-WT	GBM	m	1	1
#260UKF	T	5	temporal	81	IDH-WT	GBM	m	1	1
#259UKF	T	3	temporal	75	IDH-WT	GBM	f	1	1
#256UKF	C	4	temporal	64	C	Cortex	f		
#256UKF	TC	4	temporal	64	IDH-WT	GBM	f		
#256UKF	TI	4	temporal	64	IDH-WT	GBM	f		
#255UKF	T	5	temporal	81	IDH-WT	GBM	f		
#251UKF	T	4	temporal	61	IDH-WT	GBM	m		
#248UKF	C	1	frontal	44	C	Cortex	m	1	1
#248UKF	T	1	frontal	44	IDH-WT	GBM	m		
#243UKF	T	1	frontal	55	IDH-WT	GBM	f		
#242UKF	C	1	frontal	81	C	Cortex	f		
#242UKF	T	1	frontal	81	IDH-WT	GBM	f		
#241UKF	C	1	temporal	19	C	Cortex	m		
#259UKF	T	3	temporal	75	IDH-WT	GBM	f		
#296UKF	T	9	temporal	34	IDH-WT	GBM	m	1	1
#304UKF	T	9	temporal	81	IDH-WT	GBM	m		
#313UKF	C	10	temporal	57	C	Cortex	m		
#313UKF	T	10	temporal	57	IDH-WT	GBM	m		
#334UKF	C	10	frontal	73	C	Cortex	f		
#334UKF	T	10	frontal	73	IDH-WT	GBM	f		

13 Tissue Type (Macroscopic): T: Tumor, C: Cortex, TC: Tumor Core: TI: Tumor Infiltrative region

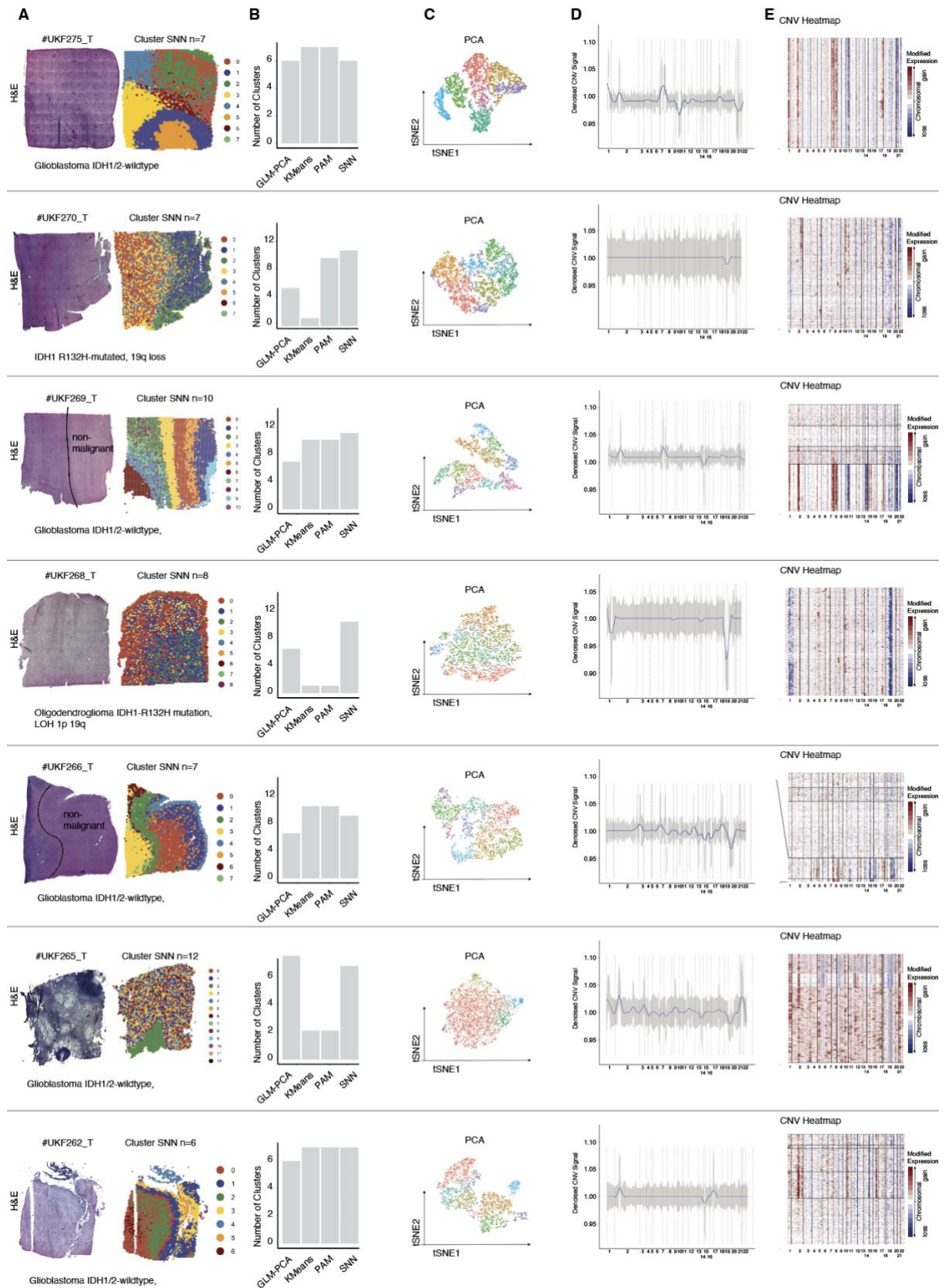
14

15 **Supplementary Figure 1**

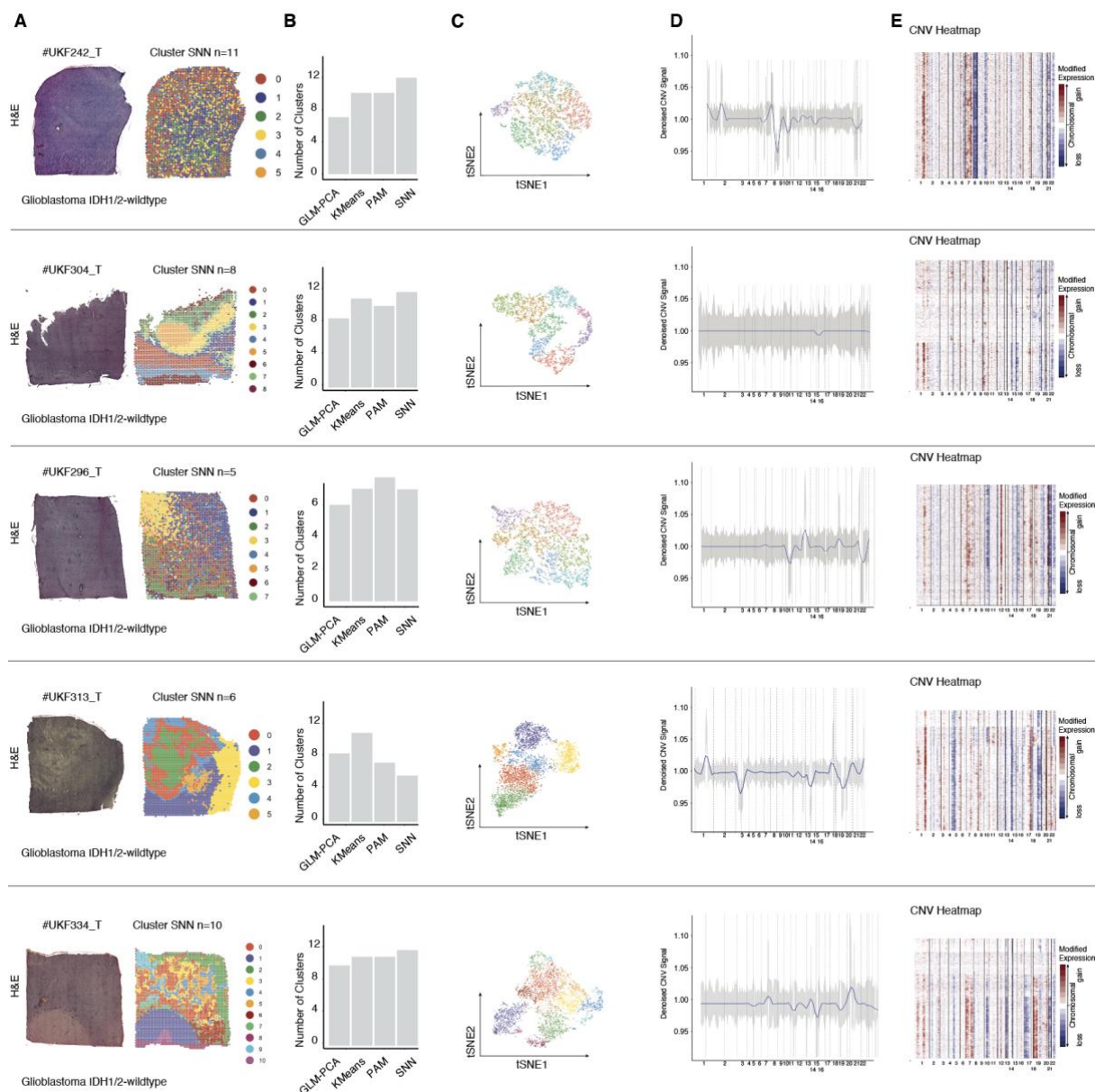


16

17



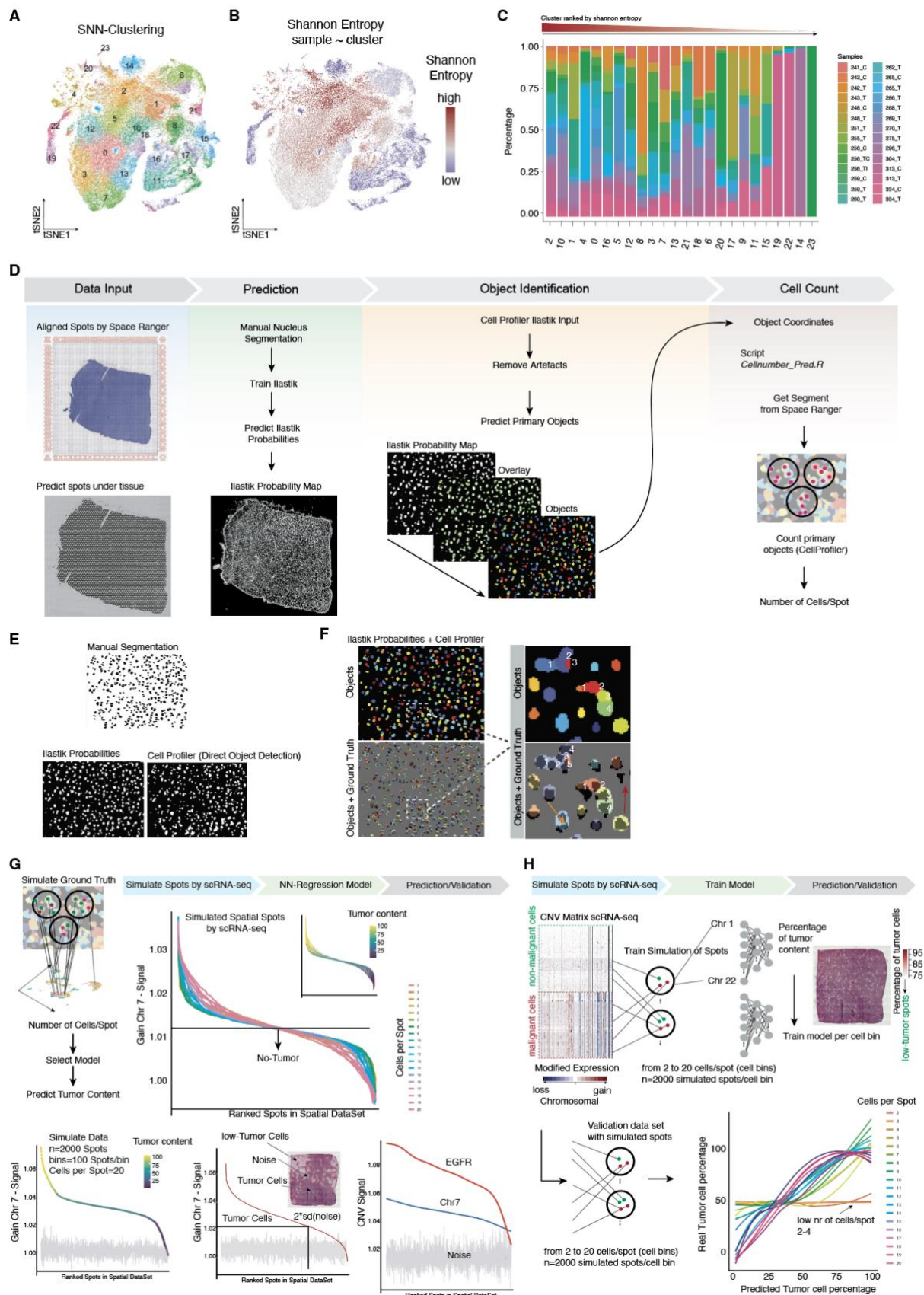




## Supplementary Figures 1: Overview of the cohort, related to Figure 1

(A) Illustration of a H&E staining (left) and the optimized SNN cluster analysis at the right side using iterative resolutions. (B) Bar plot of the optimal number of clusters using various algorithms (C) UMAP projection of spots. (D) Illustration of the copy number profile presented as line plot (left) with standard deviations marked in grey. (E) CNA alterations presented as heatmap. Blue indicate a chromosomal loss, red a chromosomal gain.

27 **Supplementary Figure 2**



28

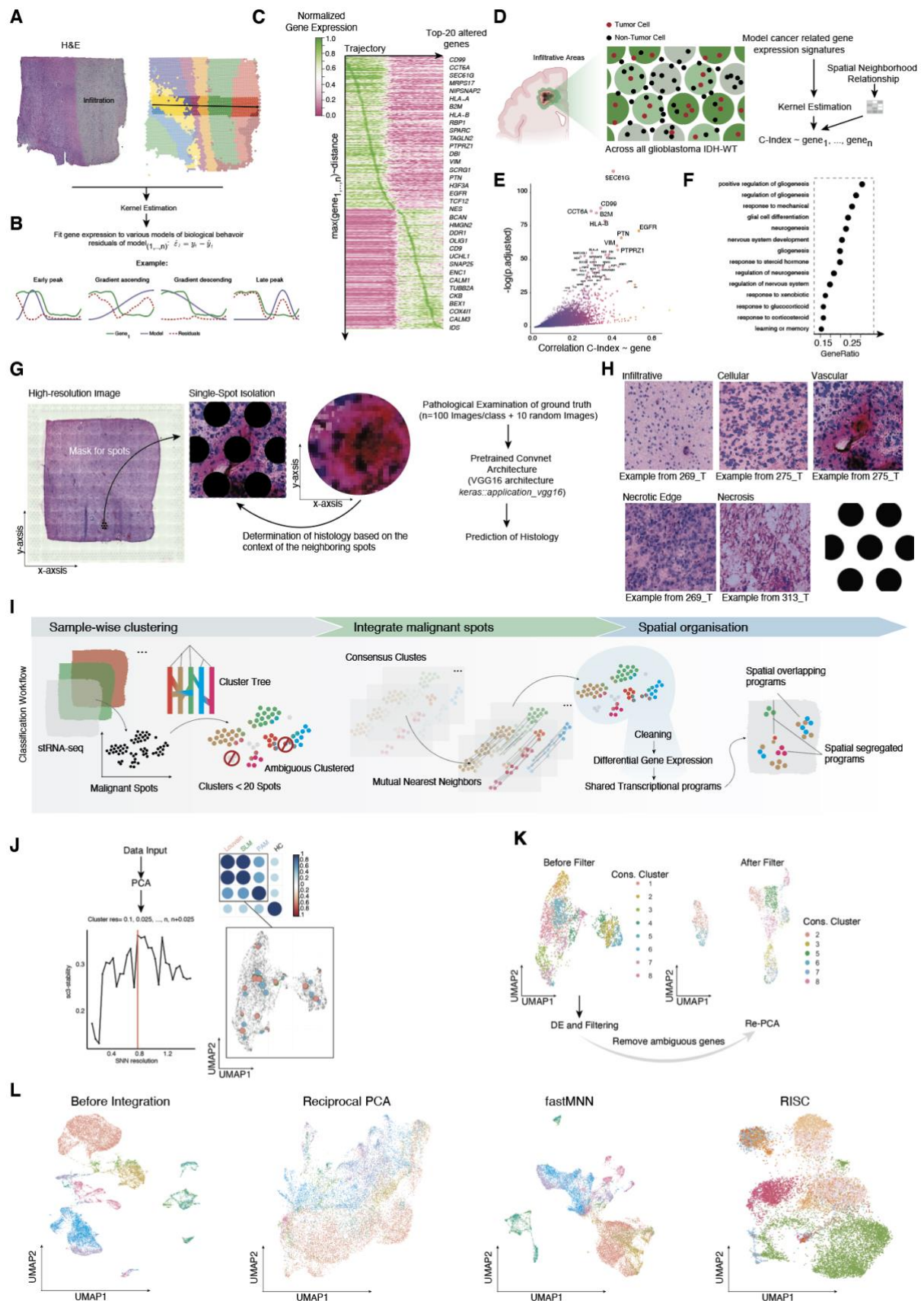
29 **Supplementary Figure 2: Data integration stRNA, related to Figure 1**

(A) A dimensional reduction using the tSNE algorithm. Colors indicate clusters from the Shared Nearest Neighbour (SNN) approach. (B) To investigate the extent to which clusters were patient specific or included multiple individuals, we estimated Shannon Entropy between clusters and patients. Clusters are colored by respective entropy in the tSNE representation. (C) Bar plot representation of patient distribution across clusters, sorted by entropy. (D) Illustration of the workflow for nucleus segmentation from stRNA-seq datasets. (E) Validation of segmentation was performed by comparing manual segmentation (ground truth, upper image), ilastik probability maps (bottom left) and the CellProfiler object identification (bottom, right). (F) Example of the combined ilastik+CellProfiler strategy for segmentation. The identified object is illustrated in the upper image and the overlay of the ground truth (bottom). The enlargements on the right show the inaccuracies of automated segmentation. In some cases, clumped objects are not separated correctly. The arrows show that some nuclei are not recognized (red) or are detected incorrectly (orange).

(G) On the upper left, overview of the workflow for spatial data simulation is illustrated. A detailed description of the method can be found within the STAR-Methods. In a nutshell, single-cell sequencing data were used to generate randomly assembled spots with both tumor and non-malignant cells. This dataset was used as ground truth to determine the content of malignant spots. Training and validation datasets were also simulated. Since the spots contain differing number of cells, we simulated spots similarly. We then computed copy number variants at large chromosomal regions and compared the gain of chromosome 7 in simulated spots (plot bottom left) and our stRNA-seq data (middle plot). The gray signal represents the average noise (based on chromosomes without alterations). Chromosome 7 intensity from non-simulated stRNA-seq data exhibits increased noise compared to simulated data. Using a loess regression model, we found that a prediction of the tumor content is highly biased by the signal to noise ratio (bottom right plots). (H) The insufficient accuracy of the simple regression model necessitated a switch to deep learning (artificial neural network, ANN) approach. A detailed description is provided in the STAR-Methods. We trained the ANN to predict the number of malignant cells in our simulated dataset. This was possible with high accuracy in spots composed of 5 cells and more. Low cell numbers per spot lack sufficient prediction (bottom right).



58 **Supplementary Figure 3:**



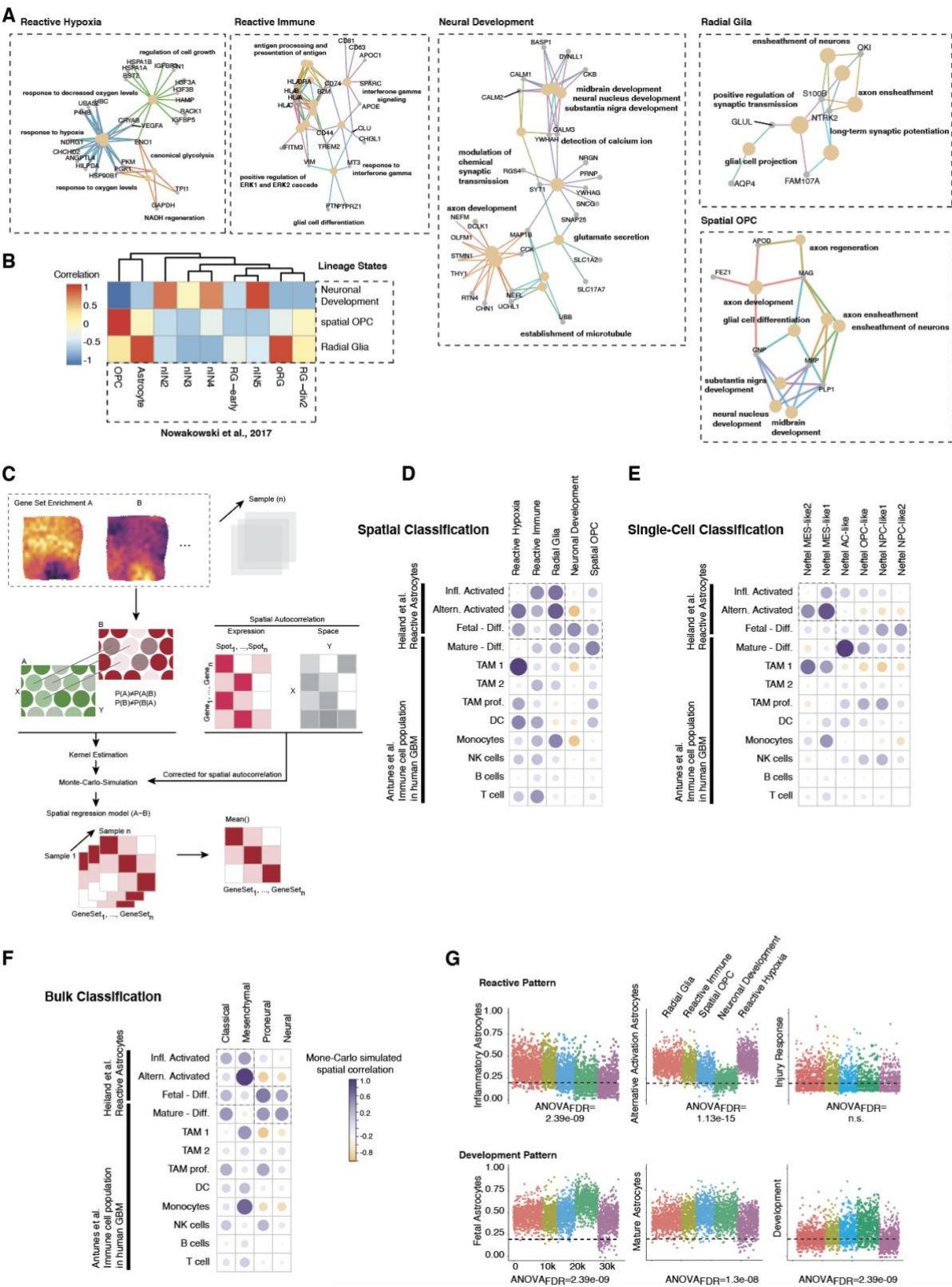
59

60 **Supplementary Figure 3: Analysis of the infiltrative margin and data integration, related to Figure**

61 **1-2**



(A) In order to analyze infiltrated areas, we performed spatial trajectory analysis, described (Kueckelhaus et al., 2020) in detail recently and in the STAR methods. An illustration helps visualize the concept of spatial trajectory analysis. (B) Feature behavior (gene expression/ gene set enrichments or other phenotype features) is fitted to a library of predefined biological behavior's and validated by its residuals (integral of the residuals: area under the curve, AUC). Features with low AUC were filtered to screen for defined transcriptional adaptations along the trajectory from tumor towards the infiltrated cortex. (C) Heatmap of filtered genes with a low AUC ( $< 2$ ) with the biological behavior: "early peak", "one peak", "late peak", smoothed by a gaussian kernel and ranked by maximum expression along the trajectory. In the transition between tumor and infiltrative cortex, an increased expression of Radial Glia marker (*VIM*, *PTPRZ*) is demonstrated. (D) Illustration of the second approach to investigate the infiltrated areas. Only a minority of cells per spot are tumor cells, therefore CN-Analysis is used to identify low tumor content based on our simulated single cell data. Using the tumor content probability (Cancer (C)-index), a spatially weighted correlation (bi-weighted 2D Kernel estimator) is displayed, to identify genes that correlate with the probability of tumor localization. (E) Genes that were also identified in the transition area between cellular tumor and infiltrated cortex (F) The dot plot shows that gene set enrichment indicates increased gliogenesis related to migration and differentiation. (G) Illustration of the workflow to determine the histology at spot-level. A detailed description of the method is given in the STAR-Methods. (H) Example of the different histology's in relation to the spot size. (I) Illustration of the workflow for cluster analysis. A detailed step-by-step explanation is given in the STAR-Methods. (J) Illustration of an example in which multiple cluster algorithms were integrated to identify consensus clusters, based on a shared cluster tree structure. On the left, the iterative approach to determine the optimal cluster resolution is illustrated. On the x-axis, the resolution is shown, on the y-axis the determined cluster stability (based in the clustertree package). (K) After consensus cluster determination, the spots were filtered by its cluster affiliation. The illustrated UMAPs indicate the spot distribution before (left) and after filtering (right). (L) An example of horizontal data integration (n=6 spatial datasets) with features as anchors. From left to right, baseline status without integration, reciprocal PCA (Andreatta and Carmona, 2020), mutual nearest neighbors (Haghverdi et al., 2018) and RISC (Liu et al., 2021)



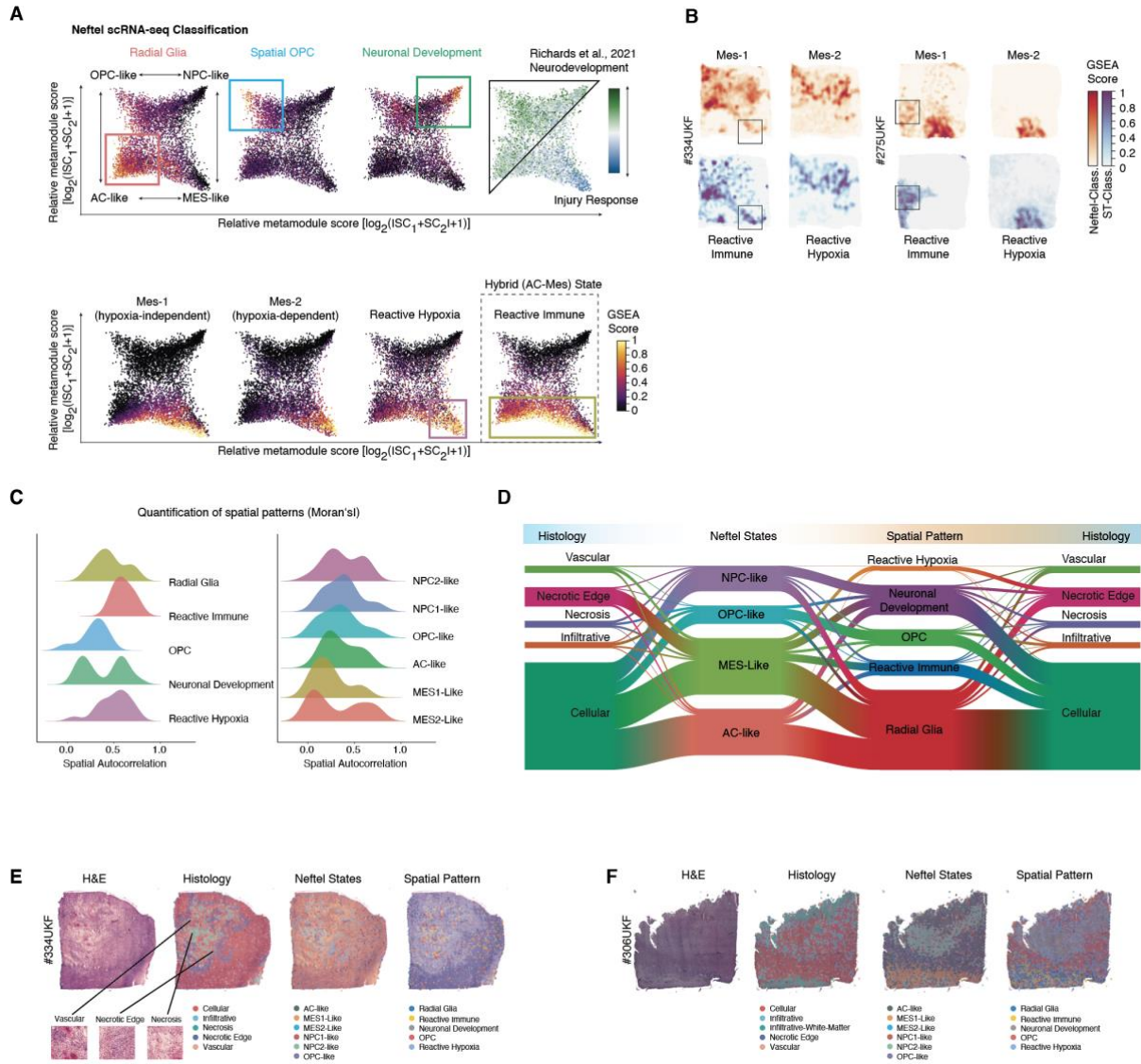
92

93      **Supplementary Figure 4: Analysis of the spatially distinct transcriptional programs, related to**

94      **Figure 2**

(A) Go-term enrichment and pathway enrichment analysis of the spatially distinct transcriptional programs using the clusterProfiler with the parameters *ont* = "ALL", *OrgDb* = "org.Hs.eg.db". The plots were built using the *cnetplot()* function. Pathways are indicated in bold; genes and pathways are presented as nodes. Connections across pathways are indicated by edges and colored in accordance to the respective pathway. (B) Heatmap of the correlation matrix between the spatially distinct transcriptional programs (only non-reactive programs) to the reference dataset of developmental stages of the human brain recently published by (Nowakowski et al., 2017). The analysis demonstrate that the identified lineage stages of tumor cells reassemble developmental stages of the human brain such as: *Neural Development*: nN2, nN4 and nN5; *Radial Glia*: Astrocytes and RG and RG-div2; *Spatial OPC*: OPC and RG-div2. (C) Overview of spatially weighted correlation analysis across multiple samples. A detailed description on the methods is given in the STAR-Methods. (D-F) Analysis of spatially weighted correlation between defined cell types of the glioma-associated environment. Cell signatures of glioblastoma associated glial cells (Henrik Heiland et al., 2019)(activated astrocytes), various myeloid cell types and T cells (Pombo Antunes et al., 2020). The correlation was illustrated by a heat-dot-plot in which correlation is indicated by size and color. (G) The illustrated scatterplot illustrates that glioblastoma reflect activation patterns and cellular states seen in non-malignant astrocytes. Signature genes of inflammatory-transformed astrocytes were enriched in the Radial-Glia and Reactive Immune programs (ANOVA and TukeyHSD, FDR=2.39e-09). Reactive Hypoxia is marked by similarity to the alternative activation signature (ANOVA and TukeyHSD, FDR=1.13e-15) (Clarke et al., 2018; Henrik Heiland et al., 2019; Liddel et al., 2017; Yun et al., 2018).

# Supplementary Figure 5



**Supplementary Figure 5: Comparison of spatial and single-cell transcriptomics, related to Figure 2**

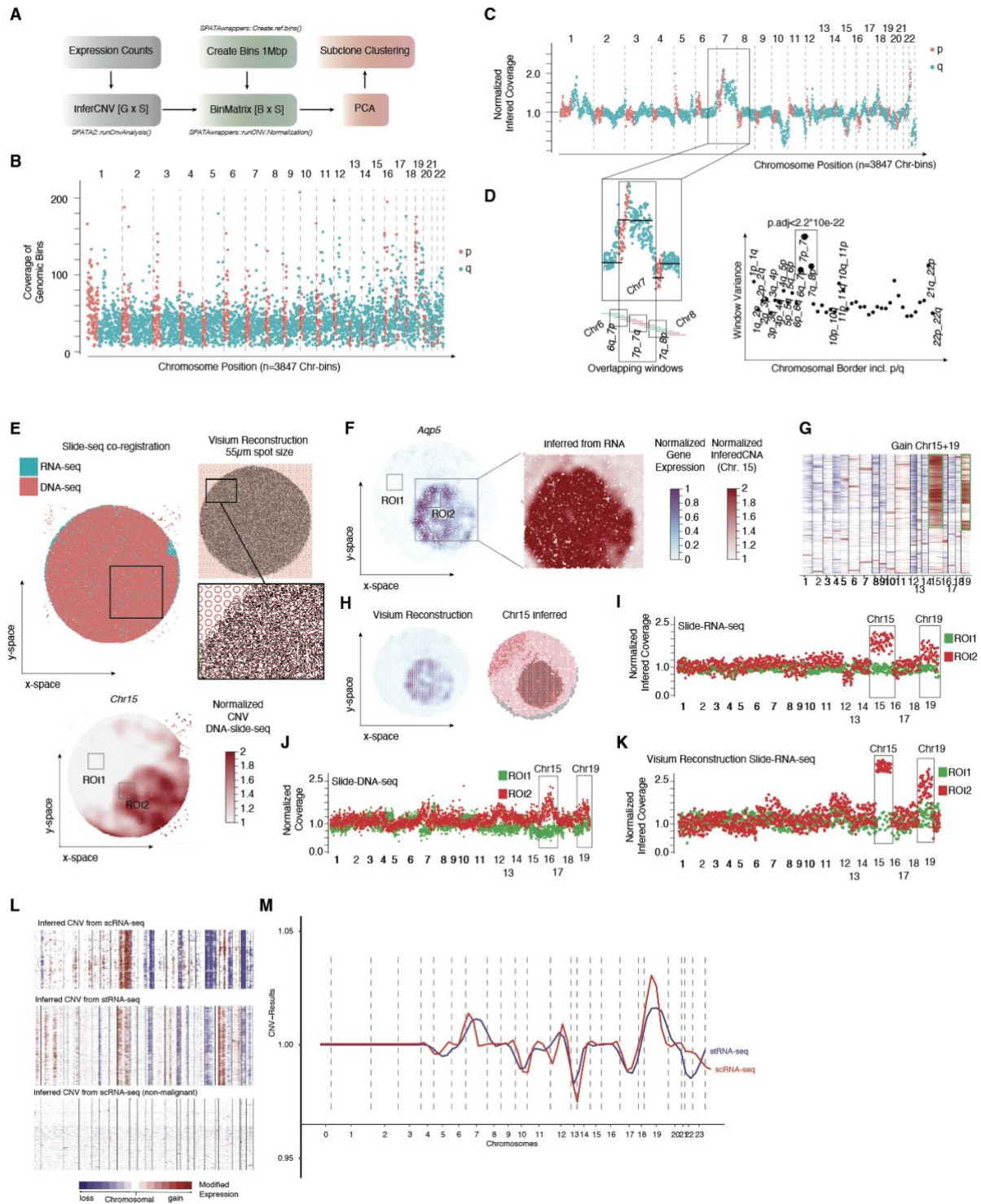
(A) Scatter plot of the 2D representation of the four major cellular states in Glioblastoma (Neftel-classification). The color code represents geneset enrichment scores for the spatially distinct transcriptional programs or the two-state classification from Richards (Richards et al., 2021) (upper right). At the bottom, the enrichment of the MES1 and MES2 state (Neftel) is presented (left) and the reactive states from our spatially distinct transcriptional programs (right) are illustrated. (B) Gene expression surface plots of the sample #334UKF (right) and #275UKF (left). The plots illustrate the spatial overlap of MES-1 gene signatures (Neftel et al., 2019) to Reactive Immune and MES-2 gene signatures (Neftel et al., 2019) to Reactive Hypoxia. The highlighted regions indicate areas containing differences between both subgroups. (C) Statistical evaluation of the spatial exclusivity based on



130 Morans's I statistics. A detailed description is given in the STAR-Methods. The density of  
131 autocorrelations of all samples is presented.

132 (D) River plot of the subgroup annotations across all patients between histological annotations, cellular  
133 states and spatially distinct transcriptional programs. (E-F) Examples of two patients with annotated  
134 histological pattern, cell states and spatially distinct transcriptional programs.

135



137

138 **Supplementary Figure 6: Validation of CNA Analysis, related to Figure 2**

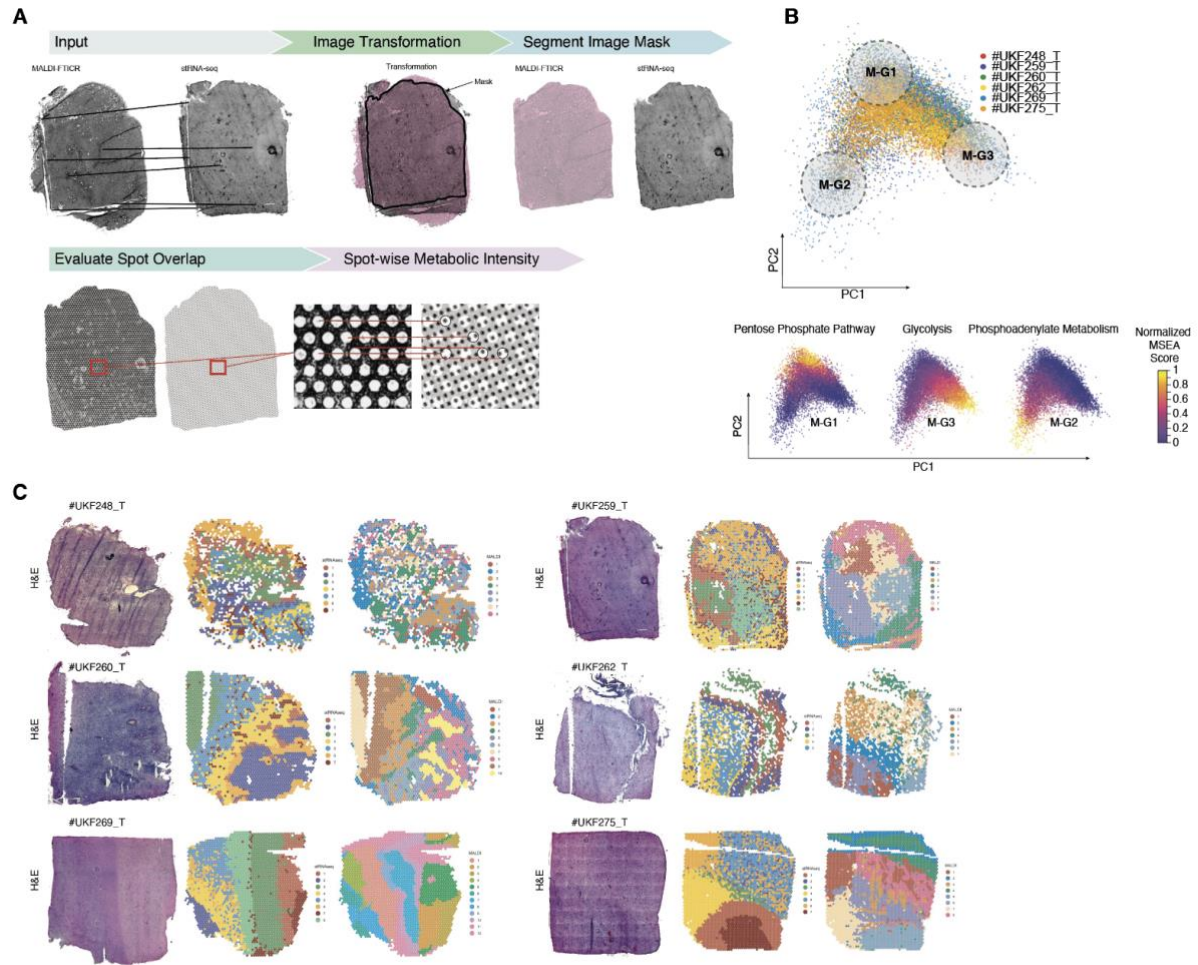
139 (A) Illustration of the workflow for copy number analysis. The input from the inferCNV algorithm was  
140 used to create defined 1mbp bins of the chromosome. The SPATAwrapper package was used to  
141 normalize the copy-number signal to the bins and estimate real copy-number values. Further subclonal  
142 analysis was performed by PCA and kMeans clustering. (B) At 1Mbp bins the coverage was 25.45 at  
143 10kbp 5.5 genes per bin. The coverage plot illustrates the variance of coverage across chromosomal

regions. In the smaller chromosomes (13-22) the p-arm was underrepresented causing a potential bias.

(C) A representative example of the copy number alterations seen in #UKF275T. (D). Illustration to what extent chromosomal gains/losses respect chromosomal borders. The significance of a chromosomal loss/gain was calculated using ANOVA and the resulting p-value was corrected using FDR. On the right, the variance of overlapping windows is illustrated (variance on the y-axis). (E) Validation of inferred CNVs with measured CNAs from DNA sequencing. In order to validate our algorithm, we used the recent published combined DNA-, RNA-slide seq dataset (Zhao et al., 2022). An overview of the alignment of both DNA- and RNA-slide-seq datasets is given in (E). Colors indicate the dataset origin. Since the slide-seq technology has a spatial resolution of 10µm which is 30.23 times lower compared to Visium spot (55µm diameter). In order to correct for these differences, we created a Visium spot mask (55µm diameter, 100µm center-to-center) and averaged the gene expression within each Visium spot (a mean number of 30.32 slide-seq spots). (F) Gene expression surface plot of *Aqp5* indicate the right bottom liver metastasis. The gains of chromosome 15 from the inferred CNA analysis is indicated at the right side. (G) CNA heatmap of the samples shows areas of tumor (Chr 15 & 19 gain).

(H) A surface plot of *Aqp5* and the inferred gain of chromosome 15 was illustrated. (I-K) Direct comparison of CNAs across chromosome 1-19 from inferred CNA slide-seq(I) DNA data (J) and from the Visium reconstruction (K). Colors indicate the ROIs. Significance is tested by two-sided t-test demonstrated at the bottom. I) Heatmap of CNAs from scRNA-seq (upper panel), stRNA-seq (middle panel) and non-malignant reference. M) Direct comparison of mean CNA obtained from sc- or stRNA-seq data. Both data types were from the same tissue source.

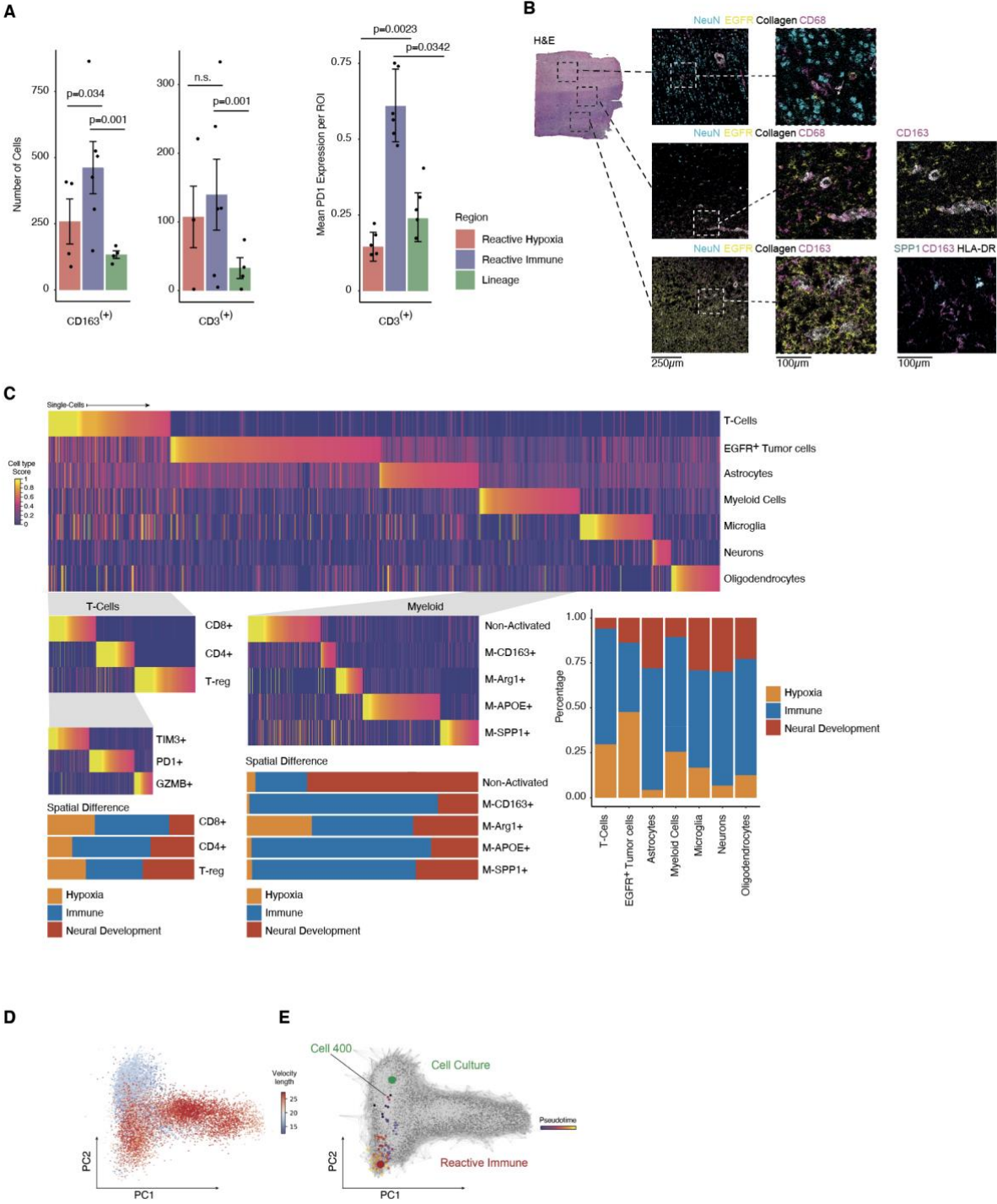
Supplementary Figure 7



Supplementary Figure 7: Integration of MADi and stRNA-seq related to Figure 4

A) Workflow of the image processing and alignment of metabolic and stRNA-seq data. A detailed explanation is given in the STAR Methods B) PCA based dimensional reduction of metabolic spots, colors indicate the patients. (bottom) Metabolic enrichment of Pentose Phosphate Pathway (PPP) (left), Glycolysis (middle) and the Phosphoadenylate Metabolism (right). Colors indicate the enrichment score. C) Overview of aligned metabolic and transcriptional data.





176  
177 **Supplementary Figure 8: Analysis of IMC Data, related to Figure 7 - 8**

178 A) Bar plots of cell counts for tumor-associated macrophages (CD163<sup>+</sup>) and T cells (CD3<sup>+</sup>) (on the left)  
179 in different ROIs. On the right, the expression of PD1 in CD3<sup>+</sup> cells within different areas was quantified.  
180 Error bars illustrate the standard error and significance levels were determined using ANOVA. B)  
181 Sample with tumor and infiltration areas (#UKF\_269). ROI's used for IMC are marked in the H&E image.  
182 IMC images (right) from all regions illustrate the different distribution of tumor cells (EGFR), neurons

(NeuN) and myeloid cells (CD68 and CD163). Bottom-Right: immunostaining (IMC) of SPP1, HLA-DR and CD163 illustrate the typical tumor-associated activated myeloid cells. C) Illustration of the cell type identification in IMC data. A heatmap of cellular distribution in different spots is illustrated. At the top, all regions are summarized (~82,000 cells). Middle panel: T cells and subgroups (bottom right). In the middle panel, the myeloid cells are further characterized. D) PCA dimensional reduction. Colors indicate the velocity length. E) A velocity graph embedded in the PCA dimensions reduction is illustrated. After deriving a distribution over root cells from the graph, the average number of steps needed to reach a cell after walking along the graph starting from the root cells is measured. Here, a random cell of the cell culture is selected.

**Table S4: IMC Antibodies, related to Figure 7**

Metal	Target	Clone	Company	Cat#	LOT	Dilution
89Y	CD45	D9M8I	CST	13917BF	8	200
111Cd	CD4	RPA-T4	BioLegend	300502	B273528	50
113In	VEGFA	G153-694	BD	555036	9344458	100
115In	HLA-DR	TAL-1B5	Abcam	ab176408	GR3314722-2	400
141Pr	Iba1	EPR16588	Abcam	ab178846	GR3290113-2	100
142Nd	EGFR	A19002A	BioLegend	933902	B297820	400
143Nd	GFAP	EPR1034Y	Abcam	834501	B305731	100
144Nd	CHI3L1	EPR19078-157	Abcam	ab255864	GR3281325-2	200
145Nd	CD3	Poly	Fluidigm	85061BF	4	200
146Nd	Ki-67	B56	Fluidigm	556003	8116751	200
147Sm	CD163	EDhu-1	Fluidigm	3147021D	242001	200
148Nd	NeuN	1B7	BioLegend	834501	B305731	400
149Sm	SPP1	A15059B	BioLegend	691302	B246000	100
151Eu	CCL2	Poly5360	BioLegend	536002	B264582	100
152Sm	CCL4	W15138A	BioLegend	686202	B217782	100
153Eu	HOPX	Poly	Abcam	ab230544	GR3283075-3	100
154Sm	Tim-3	D5D5R	Fluidigm	3154024D	3251902	200
155Gd	FoxP3	236A/E7	Thermo	14-4777-82	2129676	100
157Gd	OLIG1	EPR6790	Abcam	ab248054	GR3316742-1	400
158Gd	PD-1	EH12.2H7	BioLegend	329902	B292191	100
159Tb	CD68	KP1	Fluidigm	3159035D	2421901	5000
160Gd	CALM2	EPR5028	Abcam	ab247990	GR3321108-1	100
161Dy	THY1	5E10	Fluidigm	3161009B	0022002	3200
162Dy	CD8a	C8/144B	Fluidigm	372902	B298974	800
163Dy	SNAP25	O91D3/SNAP-25	BioLegend	850302	B240762	100
164Dy	Arginase-1	D4E3M	Fluidigm	93668BF	5	100
165Ho	NTRK2	A15019C	BioLegend	695102	B231674	5000
166Er	VIM	O91D3	BioLegend	677802	B267131	1600

167Er	GranzymeB	EPR20129-217	BioLegend	3167021D	2771902	400
168Er	CD24	ML5	BioLegend	311127	B240406	200
169Tm	Collagen	Poly	Fluidigm	3169023D	281902	800
170Er	CD44	BJ18	BioLegend	338811	B229015	3200
171Yb	APOE	A17065A	BioLegend	852802	B257864	200
172Yb	CD11b	ICRF44	BioLegend	301337	B291844	400
173Yb	CD45RO	UCHL1	Fluidigm	304202	B265383	400
174Yb	C3	K13/16	BioLegend	518101	B202439	1600
175Lu	CCR4	L291H4	BioLegend	359402	B280308	100
176Yb	cCasp3	5A1E	CST	9664S	23	50
191/193Ir	DNA		Fluidigm	201192A	P19H2305	2000

194

195

196